Ferromagnet/Semiconductor interfaces: Spin injection and Anisotropic polar magneto-optic Kerr effect

Dissertation

zur Erlangung des Doktorgrades
der Naturwissenschaften (Dr. rer. nat.)
der Fakultät für Physik
der Universität Regensburg

vorgelegt von

Martin Buchner

aus Regensburg

im Jahr 2017

Promotionsgesuch eingereicht am: 09.06.2017

Die Arbeit wurde angeleitet von: Prof. Dr. Christian H. Back

Prüfungsausschuss:	Vorsitzender:	Prof. Dr. K. Rincke
	1. Gutachter:	Prof. Dr. C. H. Back
	2. Gutachter:	Prof. Dr. D. Bougeard
	weiterer Prüfer:	Prof. Dr. J. Fabian

Contents

1. Introduction

With the development of the first semiconductor bipolar transistor in 1947 [1, 2] and the invention of the integrated circuit in 1958 [3] the semiconductor industry and thus our modern information age started. Since its beginnings the industry has experienced a remarkable growth, leading to the information technology revolution that gave rise to modern computers, smartphones, high-speed internet and so on. For more than 50 years now the semiconductor industry follows Moores's law, which states that the number of transistors on a microprocessor chip doubles every two years [4, 5]. To achieve this chipmakers have reduced the transistor feature size from 10 µm in 1965 to approximately 10 nm nowadays [6]. Shrinking the components had the pleasant side effect that the chips became faster, since the electrons could move more quickly through the circuits. Therefore, the clock rate of the microprocessors and thus the computing performance increased, while simultaneously the power consumption and the costs per transistor decreased [6, 7].

In the course of its history, the semiconductor industry has undergone several major changes. Starting with Si bipolar transistors, the industry moved first to p-type and then to n-type metal-oxide-semiconductor field-effect transistors (MOSFETs, see Fig. 1.1 on the left hand side). Today, data processing and computing are dominated by complementary metal-oxide-semiconductor (CMOS) technology, which is based on a combination of both p- and n-type MOSFETs integrated on the same Si substrate [6]. However, the ongoing size scaling according to Moore's law slowly comes to an end, since the semiconductor industry is confronted with several fundamental physical limitations, like large off-state leakage currents due to the small gate lengths or parasitic capacitances arising from the neighbouring elements [6]. Moreover, the chips dissipate more and more power due to the high density of the components on it [7]. For this reason, already in 2004 the clock rate of the processors was capped at about 4 GHz, in order to limit the heat dissipation. Simultaneously, the architecture of the processors was changed from single to multi-core to keep the performance improving [7].

Since the end of simple transistor scaling seems to be near, it is important to explore alternatives that could be used to augment or even replace the existing CMOS technology. One highly active field of research is spin-based electronics, better known under the short name "spintronics" [8]. In contrast to conventional

electronics, which exploits solely the charge of the electron for data processing, spintronics is based on the spin of the electron. By using the electron spin as an additional degree of freedom it is possible to add new functionalities to electronic devices. The study of spintronic effects started in the 1980s and was triggered by the experimental realization of electron spin injection from a ferromagnetic into a paramagnetic metal by M. Johnson and R. H. Silsbee [9] and the discovery of the giant magnetoresistance (GMR) effect by A. Fert *et al.* [10] and P. Grünberg *et al.* [11]. Soon after these findings metal-based spintronic devices were used for important and commercially very successful applications. The GMR and the related tunnel magnetoresistance (TMR) effect [12, 13], for instance, are used in hard disk read heads and magnetoresistive random access memory (MRAM) devices [14].

Contrary to metallic spintronic devices, semiconductor spintronics has not yet found its way into our everyday life. In principle, adding the spin degree of freedom to a semiconductor-based electronic device is expected to yield advantages like nonvolatile information storage, increased data processing speed and a lower power consumption [8, 14]. For this reason, spintronics was even included in the latest version of the "International Technology Roadmap for Semiconductors" as a potential candidate for the post-CMOS age [15]. The prototypical semiconductor-based spintronic device par excellence is the spin-FET as proposed by S. Datta and B. Das in 1990 [16]. The spin-FET, as sketched in Fig. 1.1 on the right hand side, combines all relevant challenges for the realization of a working semiconductor-based spintronic device, namely the successful injection and detection of an electron spin polarization into a nonmagnetic semiconductor heterostructure by utilizing ferromagnetic contacts and the precise manipulation of the injected spin ensemble by means of spin-orbit interaction. The on/off-state of the spin-FET is controlled by a gate voltage V_{G}, just like in a conventional MOSFET. However, here the source-drain current is not switched via a modulation of the conductivity of the channel, but by a coherent precession of the spin polarization about the gate voltage controlled spin-orbit fields. Up to now, the spin-FET is still waiting for its experimental realization.

In this thesis basic research in the field of semiconductor spintronics is performed. Two of the aspects mentioned above are investigated in more detail, namely spin injection into a semiconductor via ferromagnetic contacts and the spin-orbit coupling fields present at a ferromagnet/semiconductor interface. For this reason, the thesis is divided into two parts, that, in principle, can be read independently from each other. The first part deals with spin injection into heterostructure systems based on the III-V compound semiconductor GaAs. Due to its rather long spin lifetime GaAs is an excellent model system for the study of spintronic effects. Additionally, it is possible to combine it with various other materials by making use of molecular beam epitaxy. Ferromagnets like Fe or (Ga,Mn)As, for instance, can be grown epitaxially on GaAs and thus can be used as spin-

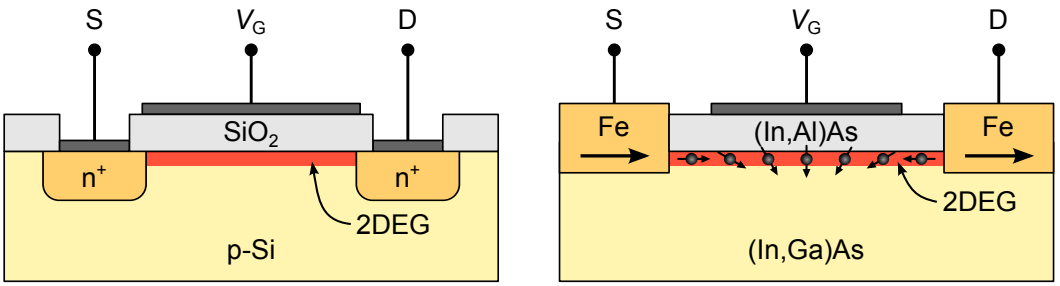

Figure 1.1.: Left: Cross section of a conventional Si n-type MOSFET. The conductivity of the 2DEG channel between source (S) and drain (D) can be controlled with a gate voltage V_G. Right: Cross section of the spin-FET as proposed by S. Datta and B. Das. A spin-polarized current is flowing between ferromagnetic source and drain contacts. The current modulation arises from spin precession underneath the gate electrode due to Bychkov-Rashba spin-orbit interaction [16].

aligning contacts. Moreover, a two-dimensional electron gas can be confined at a GaAs/(Al,Ga)As heterointerface, which allows to study spin-related phenomena in systems with reduced dimensionality. Most important for this thesis is the fact that GaAs is a direct semiconductor. This allows an optical investigation of the injected spin density by utilizing the polar magneto-optic Kerr effect. In this work a special measurement technique is used to detect the spin polarization in the GaAs. By employing scanning Kerr microscopy at the cleaved edge of the sample the spin accumulation can be observed in the transport channel directly underneath the spin injecting contacts. This approach, which was developed by Kotissek *et al.* in 2007 [17, 18] and was used afterwards by Endres *et al.* [19–22], has proven to provide important information about spin injection into GaAs-based systems.

The second part of the thesis is dedicated to the spin-orbit coupling fields present at the Fe/GaAs(001) interface and the resulting anisotropic optical properties. Spin-orbit coupling plays an important role in solid-state systems and can lead to emerging spin-orbit fields at interfaces that inherently lack inversion symmetry. The reduced symmetry at heterostructure interfaces or surfaces leads to electron momentum dependent spin-orbit fields, which affect the electronic properties of the material. So far, most investigations of interfacial spin-orbit fields rely on measurements of anisotropic transport properties. However, in 2014 Putz *et al.* showed with density functional theory calculations that the Fe/GaAs(001) heterostructure has also anisotropic optical properties [23, 24]. In particular, the Kerr rotation angle θ_K and Kerr ellipticity ε_K in polar magneto-optic Kerr effect configuration are expected to depend on the angle between the linear polarization direction of the probing laser beam and the crystallographic axes of the sample, reflecting the anisotropy of the Fe/GaAs interface. This so-called anisotropic polar magneto-optic Kerr effect (AP-MOKE) is subject of the second part of this

thesis, where it is demonstrated that an AP-MOKE can indeed be observed in ultrathin Fe/GaAs(001) samples.

The thesis is organized as follows: Chap. 2 gives an introduction to the theoretical background, which is necessary to understand the spin injection experiments. It discusses the optical properties of the investigated semiconductors and explains aspects like electrical spin injection via tunnel barriers, the D'yakonov-Perel' spin relaxation mechanism in two- and three-dimensional systems and the spin drift-diffusion theory. Subsequently, Chap. 3 describes the magneto-optic measurement scheme that was used for most of the spin injection experiments. It will be shown, how the spin polarization can be imaged at the cleaved edge of the sample by employing scanning Kerr microscopy. Moreover, the Hanle effect will be addressed, which allows to obtain a value for the spin lifetime. Here, again special attention is paid to both the two- and three-dimensional case. The experimental results are presented in Chap. 4. This chapter starts with a discussion of electrical spin injection into n-doped bulk GaAs, before it continues with spin injection experiments into a two-dimensional electron gas confined at a GaAs/(Al,Ga)As interface. Afterwards, Sec. 4.3 deals with the question, whether a spin imbalance in n-GaAs can be generated by thermal means via Seebeck spin tunneling. Finally, Chap. 5 concludes the spin injection part with a summary and an outlook.

The second part of the thesis starts with a chapter about the Fe/GaAs(001) heterostructure, highlighting aspects like its crystallographic and magnetic properties and introducing the Bychkov-Rashba and Dresselhaus spin-orbit coupling fields. Chap. 7 explains then the polar magneto-optic Kerr effect and introduces the theoretical background behind the AP-MOKE. The density functional theory calculations of Putz *et al.* are presented together with a phenomenological model, that establishes the connection between the Kerr rotation anisotropy and the interfacial spin-orbit coupling fields. The experimental findings are discussed in Chap. 8. After a pre-characterization of the investigated samples the results of the AP-MOKE measurements will be presented. Finally, Chap. 9 summarizes the results and gives an outlook.

Part I.

Spin injection

2. Fundamentals and theory

This chapter explains the theoretical aspects, which are necessary to understand the spin injection experiments. After a brief introduction into the optical properties of GaAs and (Al,Ga)As, the basic principles of electrical spin injection into semiconductors are discussed. It will be shown, that a tunnel barrier between ferromagnet and semiconductor is an important prerequisite to obtain a sizable spin accumulation. The D'yakonov-Perel' mechanism, which is responsible for spin relaxation in GaAs-based heterostructures, is explained in Sec. 2.3. Here, the differences between spin relaxation in two- and three-dimensional electron systems are discussed. Finally, Sec. 2.4 addresses the spatial distribution of a spin accumulation in a semiconductor and deals with the question, whether spin diffusion and electron diffusion are equally strong.

2.1. Optical properties of GaAs-based semiconductors

2.1.1. Optical properties of GaAs

The optical properties of GaAs are determined by its energy band structure. As depicted in Fig. 2.1 on the left hand side, GaAs is a direct semiconductor with the band gap located at the center of the Brillouin zone (= Γ-point). The band gap energy is $E_g \approx 1.52\,\mathrm{eV}$ at $T = 0\,\mathrm{K}$ [25, 26]. The conduction band (cb) has an s-like electronic character (quantum numbers $j = 1/2$, $m_j = \pm 1/2$), in contrast to the p-like valence band. Due to spin-orbit interaction the valence band is further split into three subbands: the heavy hole (hh) band ($j = 3/2$, $m_j = \pm 3/2$), the light hole (lh) band ($j = 3/2$, $m_j = \pm 1/2$) and the split-off (so) band ($j = 1/2$, $m_j = \pm 1/2$). The hh and lh bands are degenerate at the Γ-point, whereas the split-off band is shifted to lower energies by $\Delta_{so} \approx 0.34\,\mathrm{eV}$ [25, 26].

Figure 2.1 illustrates on the right hand side the optical transitions from the valence bands to the conduction band for absorption of left circularly (lc) and right circularly (rc) polarized light. Since the transitions have to obey the dipole selection rules ($\Delta l = \pm 1$, $\Delta m_l = \pm 1$) to guarantee angular momentum conservation,

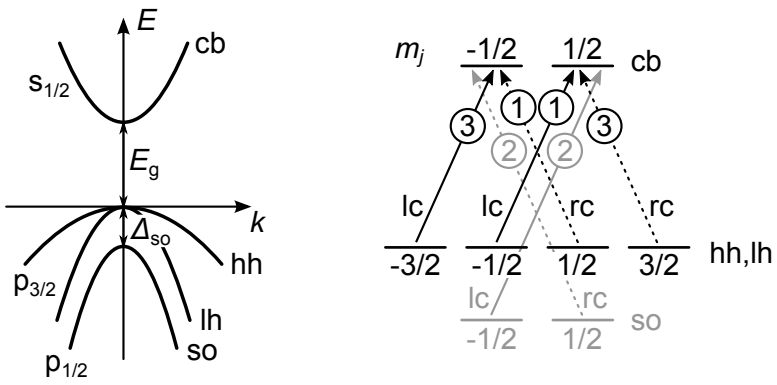

Figure 2.1.: Left: Sketch of the GaAs band structure near the Γ-point, illustrating the conduction band (cb), heavy hole band (hh), light hole band (lh) and the split-off band (so). E_g is the band gap energy and Δ_so the spin-orbit splitting. Right: Allowed optical interband transitions for the absorption of left circularly (lc) and right circularly (rc) polarized light. The circled numbers above the arrows denote the relative probabilities for a transition (replotted from [25]).

there are only six allowed transitions. The circled numbers give the relative probabilities that apply for the transitions [25]. In particular, if one chooses the energy of the incident photons such that $E_\mathrm{g} < E_\mathrm{photon} < E_\mathrm{g} + \Delta_\mathrm{so}$, there remain only the transitions from the hh and lh bands into the cb. In this case the absorption of rc polarized light will lift electrons from the hh band into the spin up subband and electrons from the lh band into the spin down subband of the cb. Since the probabilities for these transitions differ by a factor of three, the absorption of rc polarized light generates a spin polarization[1] in the cb of

$$P_n = \frac{n^\uparrow - n^\downarrow}{n^\uparrow + n^\downarrow} = \frac{3-1}{3+1} = 50\%, \tag{2.1}$$

where $n^{\uparrow/\downarrow}$ denote the densities of electrons in the cb with $m_j = \pm 1/2$ [25, 27]. Thus, circularly polarized light can be used to create an electron spin polarization in the GaAs cb. On the other hand, since recombination processes of electrons with holes have to obey the very same selection rules, a spin imbalance in the cb will generate partially circularly polarized luminescence light [25,27]. Altogether, these considerations demonstrate the close interconnection between the optical properties of GaAs with an electron spin polarization in its conduction band, which makes GaAs-based heterostructures to an ideal model system to study spin injection phenomena using (magneto-)optic methods.

[1] The spin polarization of any spin resolved quantity X is defined by $P_X = (X^\uparrow - X^\downarrow)/(X^\uparrow + X^\downarrow)$ [25, 27].

2.1.2. Persistent photoconductivity in (Al,Ga)As/GaAs heterojunctions

A part of this work is dedicated to spin injection experiments into a GaAs-based two-dimensional electron gas (2DEG). One frequently encountered way to realize a 2DEG is to confine the electron distribution within a triangular potential well formed at the interface between two semiconductors with different band gaps. In the present work a heterojunction made of Si-doped $(Al_{0.33}Ga_{0.67})As$ and intrinsic GaAs is used for that purpose. $(Al_{0.33}Ga_{0.67})As$ has a similar lattice constant as GaAs, which allows a strain-free growth of the heterostructure. Moreover, it has with $E_g \approx 1.99\,\text{eV}$ at $T = 0\,\text{K}$ [28] a larger band gap than GaAs. Fig. 2.2 shows on the left hand side the band diagrams of n-(Al,Ga)As and i-GaAs without being in contact with each other. Upon connecting the two materials electrons flow from the (Al,Ga)As into the GaAs, until the Fermi energies E_F have the same value in both semiconductors. This electron transfer is accompanied by a band bending near the interface. Since the band discontinuities ΔE_c and ΔE_v have to be preserved upon connecting the semiconductors, a triangular potential well is built in the GaAs. If the (Al,Ga)As is sufficiently highly doped, this potential well lies below the Fermi level and a metallically conducting, two-dimensional layer is created at the interface as depicted in Fig. 2.2 on the right hand side [26]. Since the 2DEG is formed in the undoped GaAs, its carriers are spatially separated from the Si-donors in the n-(Al,Ga)As. Hence, impurity scattering is highly suppressed, which makes a high electron mobility μ_e possible. To further eliminate scattering on donors right at the heterointerface, typically a several ten nanometers thick, undoped (Al,Ga)As spacer layer is grown in between the n-doped (Al,Ga)As and the i-GaAs.

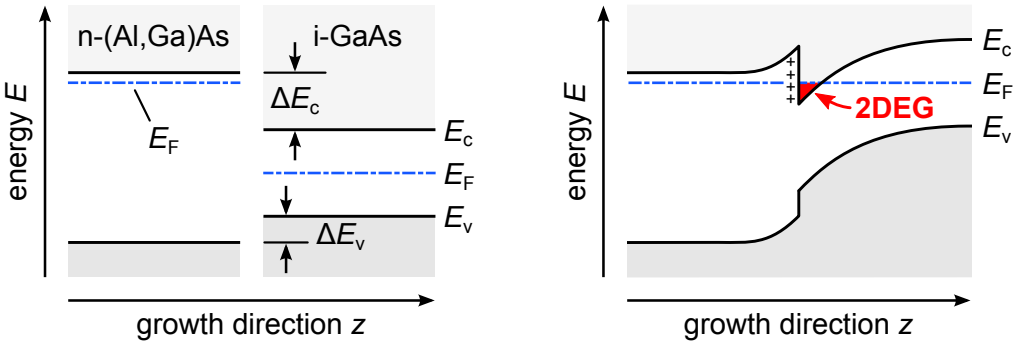

Figure 2.2.: Left: Energy band diagram of n-(Al,Ga)As and i-GaAs without being in contact with each other. ΔE_c and ΔE_v denote the band discontinuities of conduction and valence band, respectively. Right: In contact the Fermi energy E_F is balanced across the heterojunction and a degenerate electron gas is created at the interface (replotted from [26]).

In $(Al_{0.33}Ga_{0.67})As$ the Si donor atoms do not produce shallow, hydrogenic energy levels, as it would be the case e.g. in GaAs. Instead, they form deep trap states within the band gap with a binding energy of roughly 100 meV. The Si atoms do not exist in a substitutional configuration by simply occupying the Ga lattice sites, but are shifted to an interstitial position. The resulting lattice distortion in the vicinity of each donor atom creates a negatively charged, highly localized defect center. This so-called DX center is energetically more favorable than a shallow donor state [29, 30]. Due to the large lattice relaxation, the DX center has a repulsive energy barrier for both electron emission into and capture from the conduction band. This gives rise to an effect, which is called persistent photoconductivity (PPC) [31–33]. When the $(Al_{0.33}Ga_{0.67})As$ is illuminated with photons with energy larger than $\sim 1\,\mathrm{eV}$, electrons are released from the DX centers into the conduction band. At low temperatures ($T \lesssim 150\,\mathrm{K}$) these electrons cannot return back into the DX centers due to the energy barrier. Thus, the carrier density in the conduction band is permanently enhanced and persists even after switching off the light source, as long as the sample is not heated above 150 K.

For a 2DEG formed at an (Al,Ga)As/GaAs interface the PPC offers both advantages and disadvantages. On the one hand, if the sample is carefully illuminated, photoexcited electrons are transfered from the (Al,Ga)As DX centers into the 2DEG (see Fig. 2.3 on the left hand side). Thus, the carrier density of the 2DEG can be permanently increased in a controlled way. This can be of particular importance, if the 2DEG is depleted or has only a small carrier density after sample preparation. On the other hand, if the sample is heavily illuminated, electrons may populate the (Al,Ga)As conduction band as well, as it is shown in Fig. 2.3 on the right hand side. Here, the PPC creates a parallel conduction path in the (Al,Ga)As δ-doping layer next to the 2DEG. It has been shown that the carrier density in this parallel channel can be comparable to the carrier density in the 2DEG. However, the mobility of the electrons in the δ-doping region is found to be rather low; thus, electric transport through the sample is still dominated by

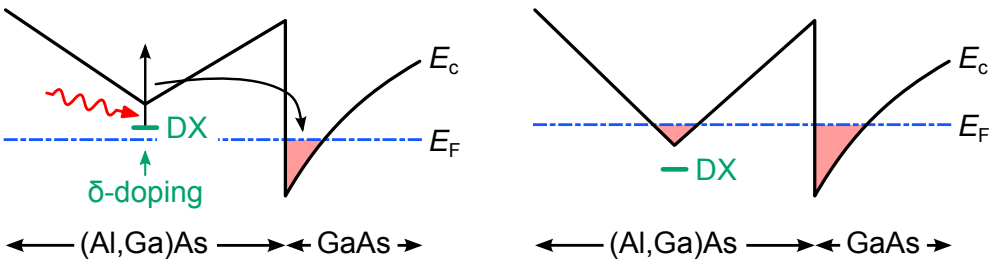

Figure 2.3.: Left: Photoexcitation of DX centers in the (Al,Ga)As δ-doping layer lifts electrons into the conduction band. The excited electrons penetrate into the 2DEG channel and increase its carrier density. Right: After heavy illumination the conduction band edge of the (Al,Ga)As is pulled below E_F and a second channel parallel to the 2DEG is formed (adapted from [34]).

the high-mobility 2DEG [34–36].

2.2. Spin injection into semiconductors

In Sec. 2.1.1 it has been shown that circularly polarized light can be used to induce a spin imbalance in the conduction band of GaAs. This section now is dedicated to the basic principles of electrical spin injection into a semiconductor.

2.2.1. The standard model of spin injection

Electrical spin injection into a semiconductor can be achieved by attaching a metallic ferromagnet to it and driving a current from the ferromagnet (F) into the semiconductor (N) as illustrated in Fig. 2.4 on the top. Ferromagnets are a natural source for spin-polarized currents, since they have different conductivities for spin up and spin down electrons ($\sigma_{\mathrm{F}}^{\uparrow} \neq \sigma_{\mathrm{F}}^{\downarrow}$). Far on the left hand side of the F/N junction in the ferromagnetic region the current densities $j^{\uparrow}$ and $j^{\downarrow}$ are different; thus, the electrons carry not only a charge current $j = j^{\uparrow} + j^{\downarrow}$, but also a spin current $j_s = j^{\uparrow} - j^{\downarrow}$. Far on the right of the interface in the semiconductor side, on the other hand, the electron current has to be unpolarized ($j_s = 0$), since here the electrons of both spin species have the same conductivities ($\sigma_{\mathrm{N}}^{\uparrow} = \sigma_{\mathrm{N}}^{\downarrow} = \sigma_{\mathrm{N}}/2$). Hence, there has to be a transfer of electrons from the spin up channel to the spin down channel near the interface, in order to depolarize the current as it flows from the ferromagnet into the semiconductor (see Fig. 2.4 in the middle). This electron transfer is accompanied by an accumulation of spin up electrons at the interface, which manifests in a splitting of the chemical potentials $\mu^{\uparrow}$ and $\mu^{\downarrow}$ for the two spin species as shown in Fig. 2.4 on the bottom. The spin splitting induces the necessary spin flips from the spin up to the spin down channel, which lead to the adjustment of the incoming and outgoing current densities $j^{\uparrow}$ and $j^{\downarrow}$ across the interface. The resulting spin accumulation $\mu_s = (\mu^{\uparrow} - \mu^{\downarrow})/2$ is not localized just at the interface, but decays with the spin diffusion lengths[2] $\lambda_{s\mathrm{F}}$ and $\lambda_{s\mathrm{N}}$ into the ferromagnet and the semiconductor, respectively [37, 38].

If the ferromagnet and the semiconductor are connected via a low resistive contact C, spin injection into the N side is found to be highly inefficient. Usually the density of states of a metallic ferromagnet is several orders of magnitude larger than that of a semiconductor; for that reason a similar splitting of the chemical potentials on both sides of the F/N junction results in a much larger spin density in the ferromagnet and consequently, the number of spin flips will be much higher in the ferromagnetic side of the F/N junction. The large amount of spin

[2] Spin diffusion will be addressed in Sec. 2.4.

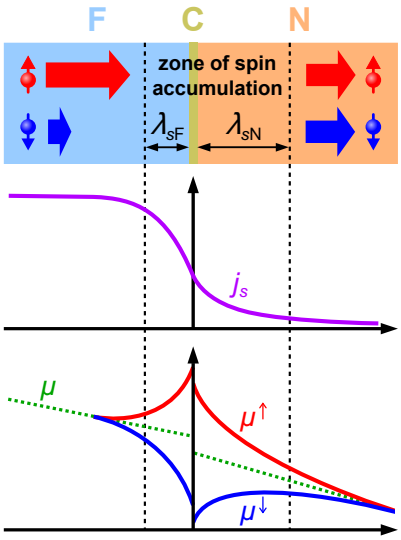

Figure 2.4: Spin injection according to the standard model. Top: Sketch of the investigated F/N junction. A ferromagnetic conductor (F) is connected to a nonmagnetic conductor (N) via a thin contact region (C). Middle: Depolarization of a current as it flows from F to N. Bottom: Splitting of the chemical potentials $\mu^{\uparrow}$ and $\mu^{\downarrow}$ at the interface. The spin accumulation $\mu_s = (\mu^{\uparrow} - \mu^{\downarrow})/2$ decays with the spin diffusion lengths λ_{sF} and λ_{sN} into the F and N region, respectively (adapted from [22, 25, 37]).

flips in the F side leads to a much stronger depolarization of the current in the ferromagnet than in the semiconductor. Thus, the current is already completely depolarized before it enters the N side and as a result, no significant spin accumulation can be injected into the semiconductor [37]. This phenomenon, which was first described by Schmidt *et al.* [39], is known as the "conductivity mismatch problem".

A solution for this problem was provided by E. I. Rashba, who suggested to insert a high resistive tunnel contact C between the F and the N side of the junction [40]. The tunnel barrier decouples the spin accumulation in the N side from the F region. Furthermore, due to the exchange splitting of the electronic states in the ferromagnet, the two spin channels have different tunnel probabilities through the barrier and therefore different tunnel conductances $\Sigma^{\uparrow}$ and $\Sigma^{\downarrow}$, i.e. the contact acts as a spin filter. The spin polarization P_j of the injection current at the F/N interface, better known as "spin injection efficiency", is then given by [41–43]

$$P_j = \frac{R_{\mathrm{F}} P_{\sigma\mathrm{F}} + R_{\mathrm{C}} P_{\Sigma}}{R_{\mathrm{F}} + R_{\mathrm{C}} + R_{\mathrm{N}}}, \tag{2.2}$$

where

$$R_{\mathrm{F}} = \frac{\sigma_{\mathrm{F}}^{\uparrow} + \sigma_{\mathrm{F}}^{\downarrow}}{4\sigma_{\mathrm{F}}^{\uparrow}\sigma_{\mathrm{F}}^{\downarrow}} \lambda_{sF}\,, \qquad R_{\mathrm{C}} = \frac{\Sigma^{\uparrow} + \Sigma^{\downarrow}}{4\Sigma^{\uparrow}\Sigma^{\downarrow}} \qquad \text{and} \qquad R_{\mathrm{N}} = \frac{\lambda_{sN}}{\sigma_{\mathrm{N}}} \tag{2.3}$$

are the effective (spin) resistances of the three involved regions and $P_{\sigma\mathrm{F}}$ and P_{Σ} denote the spin polarizations of the conductivities of the ferromagnet and the contact, respectively. Thus, if the tunnel contact dominates the total resistance of the junction ($R_{\mathrm{C}} > R_{\mathrm{N}} \gg R_{\mathrm{F}}$), it takes control over the current polarization with $P_j \approx P_{\Sigma}$ and a sizable spin accumulation can be injected into the semiconductor.

The spin accumulation μ_s in the semiconductor, which is pumped across the F/N interface by a spin current j_s, is given by [42, 43]

$$\mu_s = R_\mathrm{N} j_s. \tag{2.4}$$

It is proportional to the spin resistance $R_\mathrm{N} = \rho_\mathrm{N}\lambda_{s\mathrm{N}}$ of the semiconductor. This means that a large spin splitting can be achieved in materials with a high resistivity ρ_N. Moreover, a large spin diffusion length $\lambda_{s\mathrm{N}}$ is beneficial as well. The corresponding spin density $s = n^\uparrow - n^\downarrow$ in the semiconductor reads $s = g(E_\mathrm{F})e\mu_s$, where $g(E_\mathrm{F})$ is the density of states at the Fermi level [43].

In this work electrical spin injection into GaAs-based systems is performed using Fe and (Ga,Mn)As as spin aligners. In these cases the Schottky and Esaki barriers, which are naturally formed at the F/N junctions, provide the necessary tunnel barriers to overcome the conductivity mismatch.

2.2.2. Fe/n-GaAs Schottky tunnel barrier

For electrical spin injection into GaAs one typically uses n-type GaAs with a doping level above the metal-to-insulator transition. The degenerate n-doping of the GaAs ensures the presence of electrons in the conduction band of the semiconductor and a metallic conductance even at low temperatures. n-GaAs has a smaller work function than Fe; thus, when Fe is grown on n-GaAs, electrons flow from the conduction band of the semiconductor into the metal, until the Fermi level E_F is balanced across the whole junction and no net current is flowing. In equilibrium a high-resistive depletion zone is created at the interface and the bands of the semiconductor are bent upwards, forming a potential energy barrier for the electrons [26]. Fig. 2.5 illustrates on the left hand side a sketch of such a Schottky barrier.

When an external bias voltage V is applied to the Fe/n-GaAs junction, the quasi Fermi levels of the Fe and the semiconductor are shifted with respect to each other and an electron current I starts to flow from the Fe into the conduction band of the GaAs or vice versa (see Fig. 2.6). For not too highly doped GaAs, i.e. when the barrier is not too thin, the Schottky contact shows a pronounced rectifying behaviour with an exponentially increasing current in forward direction and a small leakage current in reverse direction, as displayed in Fig. 2.5 on the right. However, for larger doping densities the depletion zone can be designed so narrow that also ohmic barriers can be created, as will be shown later in Sec. 4.3.

At low temperatures the main contribution to the current arises from electrons tunneling directly through the Schottky barrier; thermally excited electrons, which are emitted over the top of the barrier, are only relevant at higher temperatures [44]. Thus, the Fe/GaAs junction naturally forms the tunnel barrier,

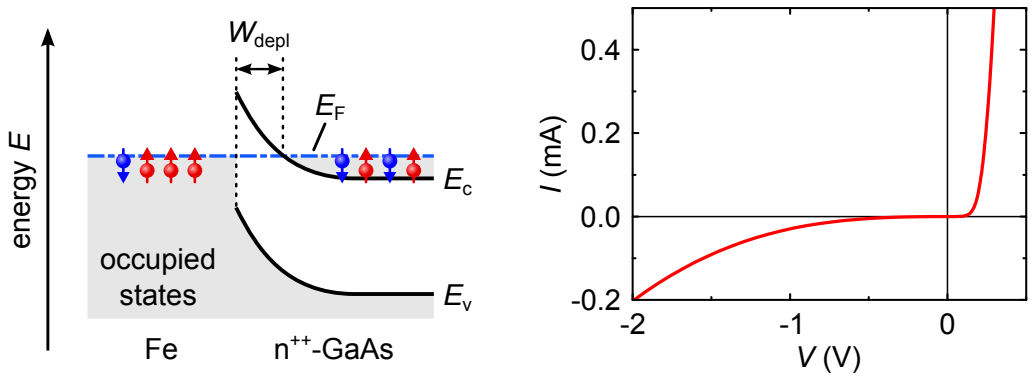

Figure 2.5.: Left: Band diagram of an Fe/n^{++}-GaAs Schottky contact at equilibrium. The band bending creates a depletion zone of width W_{depl}, which acts as a tunnel barrier. Right: Typical I-V-characteristic of a Schottky contact.

which is necessary for the efficient injection of spin-polarized carriers from the Fe into the GaAs. By applying a reverse bias voltage to the junction majority spins are injected from the Fe into the n-GaAs conduction band, resulting in a majority spin accumulation in the semiconductor. A forward bias, on the other hand, leads to an extraction of majority spins from the n-GaAs conduction band into the Fe, thereby leaving a minority spin accumulation in the conduction band behind (see Fig. 2.6).

Theoretical considerations by Wunnicke *et al.* suggest that the Fe/GaAs(001) interface can provide very large current spin polarizations [45,46]. Due to a symmetry mismatch of the minority spin bands of the Fe with the conduction band states of the GaAs, the minority spin electrons are almost totally reflected at the interface. Thus, the Fe/GaAs junction is expected to behave nearly like an ideal spin filter with spin injection efficiences P_j up to 99% for low bias voltages.

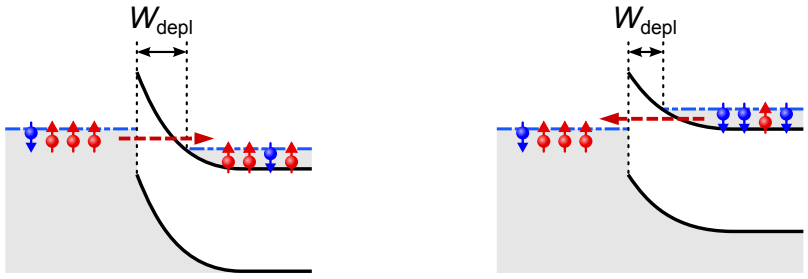

(a) $V < 0$ (b) $V > 0$

Figure 2.6.: Schottky contact under applied bias V. (a) In reverse direction majority spins are injected from the Fe into the GaAs, creating a majority spin accumulation in the GaAs conduction band. (b) In forward direction majority spins are extracted from the GaAs, creating a minority spin accumulation in the GaAs conduction band.

However, it has also been shown, that spin injection may be highly affected by the structural composition of the Fe/GaAs interface and that interfacial states can significantly enhance the role of the minority carriers [47]. Experimentally, electron spin polarizations P_n of up to about 60% were obtained in spin-LED experiments with Fe/($Al_{0.1}Ga_{0.9}$)As Schottky barriers, where the circular polarization of the emitted electroluminescence light was analyzed [48–51]. In other experiments the current spin polarization P_j for spin injection from Fe or FeCo contacts into GaAs has been found to be of the order of a few 10% [17, 52, 53].

2.2.3. (Ga,Mn)As/n-GaAs Esaki tunnel barrier

A different approach to electrically inject a spin imbalance into GaAs is to use an all-semiconductor device with ferromagnetic (Ga,Mn)As as spin aligner. (Ga,Mn)As is a dilute magnetic semiconductor, i.e. a semiconductor which is doped with magnetic impurities [54, 55]. The transition-metal element Mn is introduced into the nonmagnetic GaAs crystal, ideally replacing Ga atoms in the lattice. The Mn atoms provide magnetic moments and at the same time act as acceptors, which makes (Ga,Mn)As a p-type conducting material. Ferromagnetism arises for Mn concentrations of the order of a few percent. For such large doping densities an impurity band is created in the band gap [56] and the itinerant holes in the impurity and the valence band mediate a ferromagnetic order between the Mn atoms (cf. e.g. Refs. [57, 58] for details); a direct exchange interaction between the Mn atoms does not occur due to the large distance between them. This explains the relatively low Curie temperature of (Ga,Mn)As, which is well below room temperature. Currently, the highest reported values for T_C are around 200 K [59–61]. The ($Ga_{0.95}Mn_{0.05}$)As used in this work has a Curie temperature of about 60 K.

Electrical spin injection from (Ga,Mn)As into a GaAs-based heterostructure was first realized by Ohno *et al.* in 1999. In this experiment a hole spin polarization was injected into an undoped (In,Ga)As quantum well [62]. Subsequently, the concept was improved by Kohda *et al.* by growing the (Ga,Mn)As onto a degenerate n-GaAs layer, allowing the injection of spin-polarized electrons into the n-GaAs conduction band [63]. Fig. 2.7 shows on the left a sketch of the resulting (Ga,Mn)As/n^{++}-GaAs Esaki diode structure. Since (Ga,Mn)As is a heavily p-doped material, its Fermi energy lies in the valence band. Thus, spin-polarized electrons can be injected into the n-GaAs by direct interband tunneling from the (Ga,Mn)As valence band into the n-GaAs conduction band or vice versa, as illustrated in Figs. 2.8(a) and (b).

A peculiarity concerning the charge transport through the Esaki diode occurs for larger positive bias voltages, as sketched in Fig. 2.8(c). Here, the conduction band edge of the n-GaAs is raised to energies greater than the valence band edge of

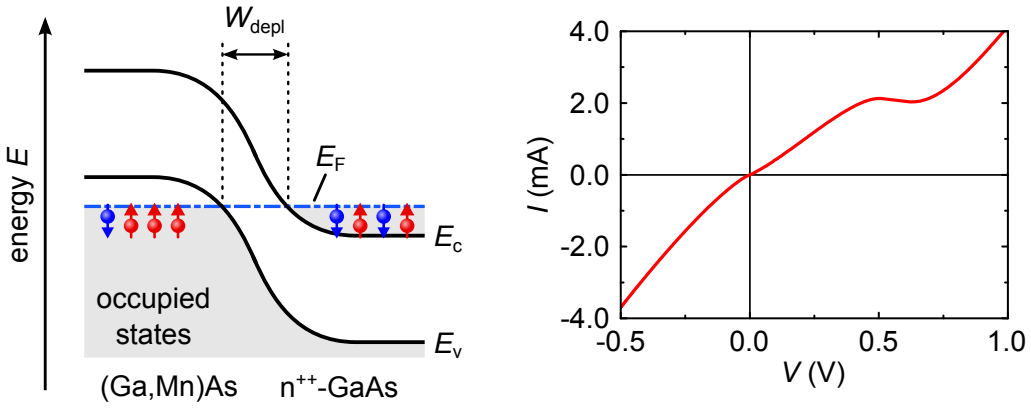

Figure 2.7.: Left: Band diagram of a (Ga,Mn)As/n^{++}-GaAs Esaki diode at equilibrium. The band bending creates a depletion zone of width W_{depl}, which acts as a tunnel barrier. Right: Typical I-V-characteristic of an Esaki diode.

the (Ga,Mn)As. Hence, a direct band-to-band tunneling is not possible. Instead, electrons tunnel by way of the Mn-induced states within the band gap [64]. This excess current regime manifests in a region of negative differential resistance in the I-V-characteristic of the junction (see the Esaki dip at $V \approx 0.6\,\mathrm{V}$ in Fig. 2.7 on the right hand side). However, tunneling via the localized band gap states does not compromise spin extraction from the n-GaAs conduction band, as was experimentally demonstrated in Ref. [65].

Electron spin injection from (Ga,Mn)As into the n-GaAs conduction band was shown to be highly efficient. Van Dorpe *et al.* obtained a large electron spin polarization P_n of about 80% for electrical spin injection from (Ga,Mn)As into an (Al,Ga)As-based spin-LED [66]. Later on, the same group investigated the

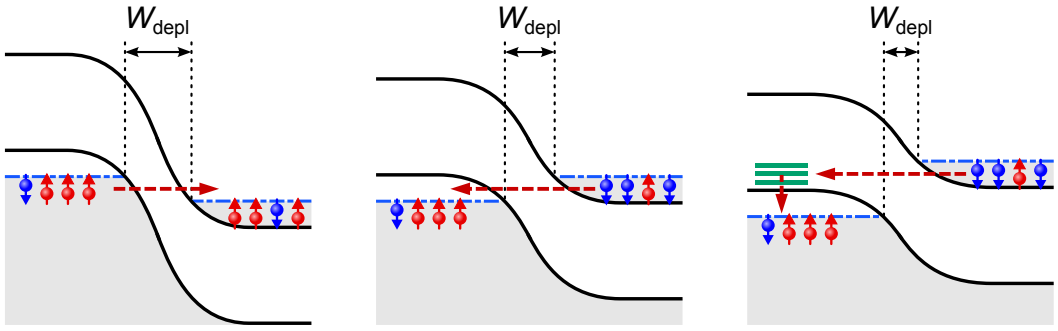

(a) $V < 0$ (b) $V \gtrsim 0$ (c) $V > 0$

Figure 2.8.: Esaki diode under applied bias V. (a) In reverse direction majority spins are injected from the (Ga,Mn)As into the GaAs. (b,c) In forward direction majority spins are extracted from the GaAs. (c) For large positive bias electrons tunnel via impurity-related band gap states from the GaAs into the (Ga,Mn)As.

used spin-LED structure by theoretical means [67]. Their calculations predicted a large current spin polarization P_j of up to 60% for low bias voltages. Nonlocal spin valve experiments by Ciorga *et al.* resulted in even higher spin injection efficiencies of up to 80% [68,69]. Both theory [67] and experiment [68] suggest a pronounced bias voltage dependence of P_j. The largest spin polarizations are obtained near zero bias. For larger bias voltages the current spin polarization decreases due to the increasing contribution of minority spin electrons transmitted through the Esaki barrier.

2.3. Spin relaxation in GaAs-based systems

2.3.1. The D'yakonov-Perel' mechanism

A spin imbalance in the conduction band of a semiconductor system is not an energetically favorable state. Therefore, after switching off the spin current which generates the spin accumulation, the system will return back to its unpolarized ground state. This equilibration process happens within a characteristic decay time, the so-called spin lifetime τ_s.

There are several mechanisms which lead to a relaxation or dephasing of an initial spin polarization (cf. e.g. Refs. [25, 27, 43] for an overview). The most important spin relaxation mechanism for the present work, however, is the D'yakonov-Perel' (DP) mechanism [70–72]. The DP mechanism dominates in degenerate semiconductors without structural inversion symmetry, such as GaAs, and in asymmetrically grown semiconductor heterostructures. These systems have strong internal electric fields. An electron in the conduction band experiences these electric fields due to spin-orbit interaction as an effective magnetic field, which couples to its spin. Both, the direction and the magnitude of these effective magnetic fields depend on the electron $\boldsymbol{k}$-vector. The spin dephasing in the DP mechanism arises now from a combination of Larmor spin precession about the effective magnetic fields and (spin conserving) momentum scattering. Since the $\boldsymbol{k}$-vector of an individual electron changes randomly after each scattering event, both the precession axis and frequency for the electron spin change randomly as well. Hence, after many subsequent scattering events the initial spin polarization is completely lost [25, 27, 43]. Fig. 2.9 shows a schematical sketch of this process.

In the DP mechanism the spin relaxes in between the scattering events. The more rapid the momentum scattering events follow each other, the less time the spin has to precess away from its initial polarization direction in between the scattering events. Thus, a large electron scattering rate stabilizes the initial spin

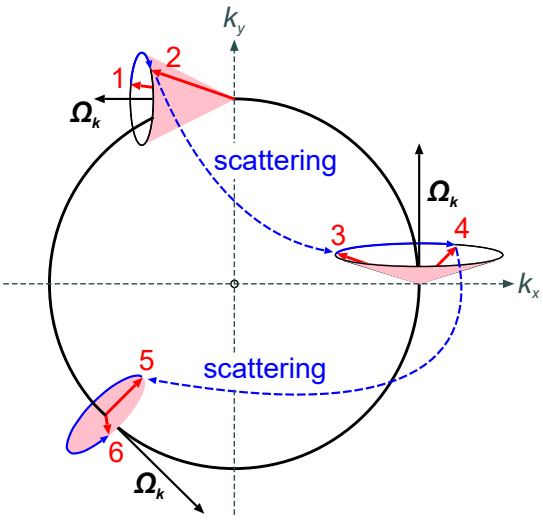

Figure 2.9: Working principle of the D'yakonov-Perel' mechanism. A spin in the initial state "1" precesses about the $\boldsymbol{k}$-dependent spin-quantization axis $\boldsymbol{\Omega_k}$. After scattering from "2" to "3" the electron momentum $\boldsymbol{k}$ and thus the precession axis $\boldsymbol{\Omega_k}$ change randomly. After several scattering events the initial spin polarization is lost. The large circle represents the Fermi surface of a two-dimensional electron gas (adapted from [27]).

polarization and results in a large spin lifetime τ_s [25, 27]. This phenomenon, which is called "motional narrowing"[3], is expressed by the relation [70]

$$\frac{1}{\tau_s} \propto \left\langle \boldsymbol{\Omega_k}^2 \right\rangle \tau_p^*, \tag{2.5}$$

where τ_p^* is the momentum scattering time of an individual electron and $\boldsymbol{\Omega_k}$ is the momentum-dependent Larmor precession frequency arising from spin-orbit interaction. Angle brackets denote the average over all $\boldsymbol{k}$-directions at E_F.

2.3.2. Spin relaxation in bulk GaAs

The effective magnetic field in a bulk III-V semiconductor can be derived from its energy band structure by taking spin-orbit interaction into account. It has been shown by G. Dresselhaus that the effective field is proportional to the cube of the electron wavevector $\boldsymbol{k}$ [73], which, in the case of GaAs, results in an intrinsic Larmor precession vector of the form [25, 70]:

$$\boldsymbol{\Omega_k} = 0.07 \frac{\hbar^2}{\sqrt{2 m_\mathrm{e}^{*3} E_\mathrm{g}}} \begin{pmatrix} k_x \left(k_y^2 - k_z^2\right) \\ k_y \left(k_z^2 - k_x^2\right) \\ k_z \left(k_x^2 - k_y^2\right) \end{pmatrix}, \tag{2.6}$$

[3] Strictly speaking, the motional narrowing limit is only valid for $\langle \Omega_{\boldsymbol{k}} \rangle \tau_p^* \lesssim 1$ [25]. For bulk GaAs one typically has $\langle \Omega_{\boldsymbol{k}} \rangle \tau_p^* \ll 1$. In the 2D case the Larmor frequency can be approximated by $\langle \Omega_{\boldsymbol{k}} \rangle \approx \frac{k_\mathrm{F}}{\hbar} \sqrt{\alpha^2 + \beta^2}$. The spin-orbit parameters for GaAs-based quantum confined systems are typically of the order of $\alpha \approx \beta \approx 5\,\mathrm{meV\AA}$ [43]. For the 2DEG samples in this work one finds $k_\mathrm{F} \approx 1.2 \cdot 10^6\,\mathrm{cm}^{-1}$ and $\tau_p^* \approx 6\,\mathrm{ps}$ (cf. Tabs. 4.1 and 4.2), what proves that the relation $\langle \Omega_{\boldsymbol{k}} \rangle \tau_p^* \lesssim 1$ is also true in the 2D case.

with m_e^* and E_g being the effective mass of the conduction electrons and the energy gap of GaAs, respectively. Eq. 2.6 demonstrates that both the direction and the magnitude of the spin precession vector strongly depend on the electron wavevector $\boldsymbol{k}$. Note that $\boldsymbol{\Omega_k}$ reflects the cubic symmetry of the GaAs crystal. However, it can be shown, that spin relaxation in bulk GaAs exhibits an isotropic behaviour, i.e. the spin lifetime τ_s does not depend on the initial orientation of the spin polarization with respect to the crystallographic directions [25, 43].

In the degenerate case the Fermi wavevector k_F of GaAs increases with the doping density n_D according to $k_F = \sqrt[3]{3\pi^2 n_D}$ [26]. Therefore, the DP mechanism will be of particular importance for larger doping levels. This is illustrated in Fig. 2.10, where the spin lifetime in n-GaAs is plotted as a function of the doping density together with the dominating relaxation mechanism. For low doping densities, in the insulating phase, electron spin relaxation is governed either by hyperfine interaction with nuclear spins of the lattice or by anisotropic exchange interactions of donor-bound electrons [74]. Above the metal-to-insulator transition at $n_D \approx 2 \cdot 10^{16}\,\mathrm{cm}^{-3}$ the spin lifetime is limited by the DP mechanism. Large spin lifetimes of the order of 100 ns can be obtained in the vicinity of the metal-to-insulator phase transition. Increasing the donor concentration makes the DP mechanism more effective and the spin lifetime decreases approximately as $\tau_s \propto 1/n_D^2$ [74].

For electrical spin injection experiments into bulk GaAs it is necessary to use n-GaAs in the metallic phase. Hence, in this work samples with donor concentrations ranging from $2.5 \cdot 10^{16}\,\mathrm{cm}^{-3}$ to $4 \cdot 10^{16}\,\mathrm{cm}^{-3}$ have been investigated. This guarantees a long spin lifetime in combination with a large electron mobility.

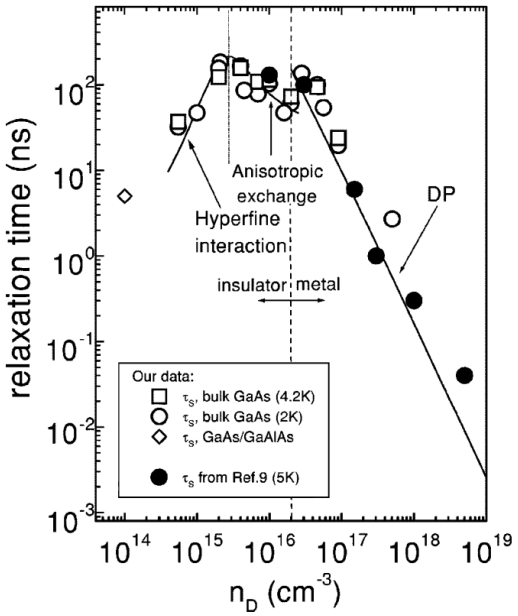

Figure 2.10: Spin lifetime τ_s as a function of doping density n_D in n-GaAs at low temperatures. In the metallic phase ($n_D > 2 \cdot 10^{16}\,\mathrm{cm}^{-3}$) spin relaxation is dominated by the D'yakonov-Perel' (DP) mechanism with maximum lifetimes of the order of 100 ns (adapted from [74]).

2.3.3. Spin relaxation in 2D electron systems

Since spin-orbit coupling in quantum confined systems is usually much larger than in bulk materials [43], spin relaxation in a GaAs-based 2DEG is according to Eq. 2.5 expected to be more effective than in bulk GaAs. Moreover, the long momentum relaxation times τ_p of high-mobility 2DEG samples should additionally contribute to an efficient D'yakonov-Perel' spin relaxation. However, it turns out that one has to be very careful, if one wants to apply Eq. 2.5 to the two-dimensional case, since 2D systems exhibit some important peculiarities, which make the DP mechanism for them less straight forward compared to bulk samples.

The influence of electron-electron interactions

The first peculiarity in 2DEGs concerns the electron scattering time τ_p^*. In the DP mechanism spin precession occurs in between scattering events, which randomize the $\boldsymbol{k}$-vector and thus the momentum-dependent effective magnetic fields. The time span in between the scattering events determines how long a spin can precess about a given $\boldsymbol{\Omega_k}$ and therefore, according to "motional narrowing", how fast it will dephase. For bulk semiconductor samples the scattering time τ_p^* of an individual electron is commonly identified with the momentum relaxation time τ_p of the electron ensemble [70, 71]. The latter is connected with the electron mobility μ_e via $\mu_\mathrm{e} = e\tau_p/m_\mathrm{e}^*$.

However, as was first pointed out by Glazov and Ivchenko, this assumption is no longer valid for two-dimensional structures [75–77]. In this case electron-electron interactions begin to play an important role. Just like scattering processes off phonons or impurities electron-electron scattering randomly reorients the $\boldsymbol{k}$-vectors of the electrons, which leads to a randomization of the precession frequencies $\boldsymbol{\Omega_k}$. Thus, if the spins of the colliding electrons are different, electron-electron interactions will contribute to the DP mechanism as well [78]. The corresponding electron-electron scattering rate for a degenerate 2D electron system is approximately given by [77, 78]

$$\frac{1}{\tau_\mathrm{ee}} \approx 3.4 \frac{E_\mathrm{F}}{\hbar} \left(\frac{k_\mathrm{B} T}{E_\mathrm{F}} \right)^2, \qquad \text{for } \; T \ll T_\mathrm{F}. \tag{2.7}$$

Since electron-electron scattering does not affect the total electron momentum, these kinds of scattering events do not reduce the mobility and thus are not taken into account by the momentum relaxation time τ_p of the electron ensemble. Hence, the effective momentum scattering rate $1/\tau_p^*$ for an individual electron can be written as [77, 79]:

$$\frac{1}{\tau_p^*} = \frac{1}{\tau_p} + \frac{1}{\tau_\mathrm{ee}}. \tag{2.8}$$

It has been argued that the contribution from electron-electron scattering to the DP mechanism can be similarly strong as from other electron scattering events [77]. Moreover, experiments showed that τ_p^* can be significantly smaller than τ_p [78]. Thus, electron-electron interactions in the 2DEG may lead to an enhanced spin relaxation time τ_s.

Anisotropic spin relaxation

In two-dimensional structures spin-orbit interaction consists of two contributions. Apart from the already mentioned Dresselhaus term [73], which has its origin in the lack of an inversion center of the GaAs crystal, the Bychkov-Rashba term [80, 81] has to be taken into account. The latter stems from the built-in electric fields, which are present at the interfaces of an asymmetrically grown heterostructure, which confines the 2DEG. In a (001)-grown GaAs-based 2DEG both Bychkov-Rashba and Dresselhaus spin-orbit interaction create effective magnetic fields, which lie in the quantum confinement plane. In the coordinate system with $x||[1\bar{1}0]$, $y||[110]$ and $z||[001]$ the corresponding momentum-dependent Larmor precession frequencies read [82, 83]:

$$\boldsymbol{\Omega}_{\mathrm{BR}} = \frac{\alpha}{\hbar}\begin{pmatrix} -k_y \\ k_x \\ 0 \end{pmatrix} \qquad \text{and} \qquad \boldsymbol{\Omega}_{\mathrm{D}} = \frac{\beta}{\hbar}\begin{pmatrix} k_y \\ k_x \\ 0 \end{pmatrix}, \tag{2.9}$$

where α and β are the Bychkov-Rashba and Dresselhaus spin-orbit parameters, respectively[4]. Fig. 2.11 illustrates the angular dependence of the superposition $\boldsymbol{\Omega}_{\boldsymbol{k}} = \boldsymbol{\Omega}_{\mathrm{BR}} + \boldsymbol{\Omega}_{\mathrm{D}}$ on the Fermi surface. In the presence of both types of spin-orbit interaction the effective fields show a tendency to be oriented along the [110] crystallographic direction (see Fig. 2.11(a)). In particular, if the Bychkov-Rashba and the Dresselhaus term have equal strengths ($\alpha = \beta$), the effective magnetic field points exactly along $(\pm)[110]$ for all directions of the electron wavevector $\boldsymbol{k}$, as shown in Fig. 2.11(b).

The anisotropy of the effective magnetic fields has direct consequences on electron spin relaxation. Contrary to bulk GaAs, spin relaxation in two-dimensional systems shows a pronounced anisotropy, as has been realized by Averkiev and Golub [85, 86]. The lifetime of an electron's spin in a 2DEG strongly depends on the spin polarization direction with respect to the effective fields. Since the $\boldsymbol{\Omega}_{\boldsymbol{k}}$ are oriented in the quantum confinement plane, a spin polarization perpendicular

[4]Note that the sign of α depends on the direction of the internal electric fields within the quantum well and can in principle be reversed with an applied gate voltage. For the considerations here the sign of α was chosen such that the symmetry of the resulting spin relaxation anisotropy fits to the majority of the experimental reports on spin relaxation in GaAs-based QW systems. A different sign of α would rotate the preferential direction of the effective magnetic fields along the $[1\bar{1}0]$ direction, yet the main ideas of the discussion would be qualitatively unchanged.

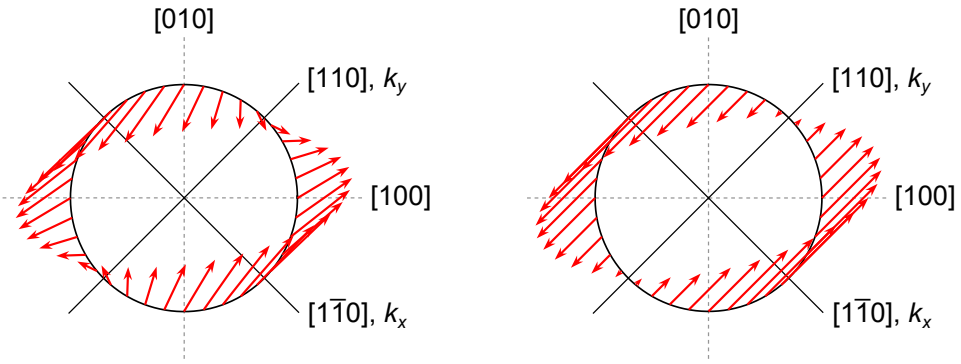

(a) $\alpha = 0.6\beta$ (b) $\alpha = \beta$

Figure 2.11.: Effective magnetic fields on the Fermi surface of a two-dimensional electron gas in the presence of both Bychkov-Rashba and Dresselhaus spin-orbit coupling. (a) For $\alpha = 0.6\beta$ the fields show a tendency to be oriented along the [110] direction. (b) At the extreme $\alpha = \beta$ the fields are perfectly oriented along [110] (replotted from [84]).

to the 2DEG plane will experience a strong spin-orbit torque and accordingly the spin relaxes very rapidly with spin lifetimes of the order of 100 ps [87–89].

For the case of an in-plane polarized spin imbalance a giant spin relaxation anisotropy has been predicted for $\alpha \approx \beta$ [85, 86]. In this case $\boldsymbol{\Omega_k}$ is oriented along [110] for all $\boldsymbol{k}$. Thus, a spin polarization along [110] does not precess at all and therefore it cannot relax via the D'yakonov-Perel' mechanism. On the other hand, a spin accumulation along the perpendicular in-plane direction [1$\bar{1}$0] has a finite relaxation rate. Indeed, it has been experimentally shown that the D'yakonov-Perel' mechanism is strongly suppressed for a spin polarization along the [110] crystallographic direction, with spin lifetimes ranging from a few to several tens of nanoseconds, whereas the spin lifetime for a spin ensemble along the [1$\bar{1}$0] direction typically remains in the sub-nanosecond regime [87, 90, 91].

In a mathematical sense, the spin relaxation anisotropy of a two-dimensional system can be modeled by introducing a spin relaxation tensor $\hat{\boldsymbol{\Gamma}}$. This tensor is diagonal in the coordinate system $x||[1\bar{1}0]$, $y||[110]$ and $z||[001]$ [82, 83]:

$$\hat{\boldsymbol{\Gamma}} = \begin{pmatrix} 1/\tau_x & 0 & 0 \\ 0 & 1/\tau_y & 0 \\ 0 & 0 & 1/\tau_z \end{pmatrix}. \tag{2.10}$$

The eigenvalues, which correspond to the spin relaxation rates for spins polarized

along the principal axes[5], are given by [82, 83]:

$$\frac{1}{\tau_{x,y}} = C\frac{(\alpha \pm \beta)^2}{2} \qquad \text{and} \qquad \frac{1}{\tau_z} = C\left(\alpha^2 + \beta^2\right), \tag{2.11}$$

with $C = k_\mathrm{F}^2 \tau_p^* / \hbar^2$. Note that the spin relaxation rate along [110] vanishes for $\alpha = \beta$ in accordance with the considerations above.

Spin dynamics in a magnetic field

As a final note, the dynamics of a spin ensemble $\boldsymbol{s}$ in an external magnetic field $\boldsymbol{B}$ shall be addressed. Ignoring spin drift and diffusion the time evolution of $\boldsymbol{s}$ is given by the Bloch equation [43, 83]

$$\frac{\mathrm{d}\boldsymbol{s}}{\mathrm{d}t} = \boldsymbol{s} \times \boldsymbol{\omega_0} - \hat{\boldsymbol{\Gamma}}\boldsymbol{s}. \tag{2.12}$$

Here, $\boldsymbol{\omega_0} = g\mu_\mathrm{B}\boldsymbol{B}/\hbar$ is the Larmor precession frequency in the external magnetic field (not to be confused with the intrinsic Larmor frequencies $\boldsymbol{\Omega_k}$ arising from spin-orbit interaction) with g and μ_B being the electron g-factor and the Bohr magneton, respectively. $\hat{\boldsymbol{\Gamma}}$ describes the spin relaxation anisotropy. Assuming an out-of-plane applied magnetic field $\boldsymbol{B}||z$ and an initial spin polarization along x ($\boldsymbol{s}(0) = (s_0, 0, 0)$) the solution of the Bloch equation reads (cf. Ref. [84] and appendix A):

$$s_x(t) = \quad s_0 \exp\left(-\frac{t}{\bar{\tau}}\right)\left[\cos(\tilde{\omega}t) - \left(\frac{1}{\tau_x} - \frac{1}{\tau_y}\right)\frac{\sin(\tilde{\omega}t)}{2\tilde{\omega}}\right], \tag{2.13}$$

$$s_y(t) = -s_0 \exp\left(-\frac{t}{\bar{\tau}}\right)\frac{\omega_0}{\tilde{\omega}}\sin(\tilde{\omega}t), \tag{2.14}$$

where[6]

$$\frac{1}{\bar{\tau}} = \frac{1}{2}\left(\frac{1}{\tau_x} + \frac{1}{\tau_y}\right) \qquad \text{and} \qquad \tilde{\omega} = \sqrt{\omega_0^2 - \frac{1}{4}\left(\frac{1}{\tau_x} - \frac{1}{\tau_y}\right)^2}. \tag{2.15}$$

For $B = 0$ the spin accumulation $s_x(t)$ shows a simple exponential decay with the decay time τ_x. For larger fields a damped precessional motion can be observed, just like in the case of isotropic spin dephasing. However, note that for the anisotropic case both the decay time and the precession frequency are modified. In particular, for large enough fields (when $\tilde{\omega}$ becomes real) the spin polarization decays with the harmonic mean value $\bar{\tau}$ of the two in-plane spin relaxation times τ_x and τ_y. For this reason time resolved pump-probe experiments on precessing spin ensembles are primarily sensitive to the harmonic mean value $\bar{\tau}$ (cf. e.g. Ref. [92]).

[5] The relaxation rate for a spin along the principal axis i ($i = x, y, z$) is given by $\frac{1}{\tau_i} = \left\langle \boldsymbol{\Omega}_{\boldsymbol{k},\perp i}^2 \right\rangle \tau_p^*$ [78]. $\boldsymbol{\Omega}_{\boldsymbol{k},\perp i}$ represents the components of the Larmor frequency $\boldsymbol{\Omega_k}$ perpendicular to the direction i.

[6] Note that $\tilde{\omega}$ can be real or imaginary. However, the solutions for $s_x(t)$ and $s_y(t)$ are always real-valued due to $\cos(\mathrm{i}\omega t) = \cosh(\omega t)$ and $\frac{\sin(\mathrm{i}\omega t)}{\mathrm{i}\omega} = \frac{\sinh(\omega t)}{\omega}$.

2.4. Spin drift and diffusion

After discussing electrical spin injection and spin relaxation the question arises, how the distribution of the spin imbalance in the semiconductor will evolve spatially after being injected. Since the spin density s in the semiconductor is carried by the electrons in the conduction band ($s = n^{\uparrow} - n^{\downarrow}$), its motion can be described as a combination of drift and diffusion, just like the motion of the conduction electrons. An electric field E, for instance, accelerates both spin up and spin down electrons in the same way, and thus also accelerates the spin ensemble s. As the electrons experience friction due to scattering the total electronic system moves on average with the drift velocity [43]

$$v_{\mathrm{d}} = -\mu_{\mathrm{e}} E, \tag{2.16}$$

where the electron mobility

$$\mu_{\mathrm{e}} = \frac{e\tau_p}{m_{\mathrm{e}}^*} \tag{2.17}$$

is determined by the momentum scattering time τ_p of the electron ensemble and the effective mass m_{e}^* of the electrons in the conduction band [26, 43]. Hence, in the presence of an electric field a spin imbalance in the semiconductor travels on average a distance $\lambda_{\mathrm{d}} = v_{\mathrm{d}}\tau_s$ within the spin lifetime τ_s. Note that the mobility μ_{e} is connected with the conductivity σ of the sample via $\sigma = ne\mu_{\mathrm{e}}$ [26]. Therefore, it can be obtained from simple transport experiments, either by measuring the resistivity ρ_{N} of bulk GaAs samples, or by determining the sheet resistance R_{s} of two-dimensional electron systems.

In contrast to the directed drift motion in an applied electric field E, diffusion describes the random walk of electrons due to scattering events off phonons and impurities. In general, electrons at the Fermi surface propagate with the Fermi velocity v_{F} through the semiconductor. After each scattering event the direction of the velocity changes randomly. In between two scattering events an electron travels on average a distance $l_{\mathrm{e,mf}} = v_{\mathrm{F}}\tau_p$, the so-called mean free path [26, 43]. Thus, an initially well confined spatial distribution of electrons or spins broadens with time due to the undirected nature of diffusive motion. The rate of electron diffusion is measured with the diffusivity D, for which the relation [43]

$$D \propto v_{\mathrm{F}}^2 \tau_p \tag{2.18}$$

holds. In degenerate electron systems the diffusivity can be calculated from the electron mobility via Einstein's relation [43]:

$$\frac{eD}{\mu_{\mathrm{e}}} = \frac{n}{g(E_{\mathrm{F}})}, \tag{2.19}$$

where $g(E_\mathrm{F})$ denotes the density of states at the Fermi level. Altogether, the time evolution of the spin density s is determined by the drift-diffusion equation [43]

$$\frac{\partial s}{\partial t} = D\frac{\partial^2 s}{\partial y^2} + \mu_\mathrm{e} E \frac{\partial s}{\partial y} - \frac{s}{\tau_s}. \tag{2.20}$$

The terms with D and E describe spin diffusion and spin drift along the y-direction, respectively. The term with τ_s accounts for spin relaxation. In many cases this one-dimensional model is sufficient to describe the spatial distribution of a spin accumulation in a semiconductor channel. In particular, Eq. 2.20 shows that the spin accumulation decays exponentially as it spreads in the semiconductor. In the purely diffusive case with $E = 0$ the spin polarization decays with the spin diffusion length [43]

$$\lambda_s = \sqrt{D\tau_s}, \tag{2.21}$$

which is determined by the diffusivity and the spin lifetime. When an electric field E is applied, the injected spin polarization additionally drifts with v_d against the field direction. Thus, there will be a superposition of drift and diffusion, which enhances or reduces the decay length with respect to λ_s depending on the direction of the electric field.

The discussion so far assumed that spin diffusion and electron diffusion have equal strenghts. This is a widely used assumption, especially since the standard model of spin injection [41–43] tacitly equates the spin diffusivity D_s with the electron diffusivity D_e. However, both experimental and theoretical work suggest that the assumption $D_s = D_\mathrm{e}$ cannot be true in general. In 1999 Kikkawa and Awschalom, for instance, reported an experiment on bulk n-GaAs, which gave a spin diffusivity D_s, which exceeded the electron diffusivity D_e by more than one order of magnitude [93]. In this experiment the spins have been generated optically by absorption of circularly polarized light. An explanation for this large discrepancy between electron and spin diffusion has been given by Flatté and Byers [94], who pointed out, that optically generated electrons in the conduction band are always accompanied by holes in the valence band. Thus, electron diffusion is limited by the low mobility and diffusivity of the holes, as the electrons drag the holes with them. On the other hand a spin imbalance in the conduction band can exist as a charge-neutral object without a hole density in the valence band, resulting in a larger D_s with respect to D_e [94]. For electrical spin injection experiments into degenerate bulk GaAs this simple model suggests that D_s should be equal to D_e, since in this case electron diffusion is not inhibited by holes. Indeed, B. Endres found no significant difference between electron and spin diffusion in bulk spin injection devices [22] similar to those investigated in this work.

The situation changes when one considers two-dimensional systems. In this case electron-electron interactions play an important role, as has already been discussed in Sec. 2.3.3. Hence, instead of Eq. 2.18 the relation $D_s \propto v_\mathrm{F}^2 \tau_p^*$ should be

used to describe spin diffusion, where τ_p^* is the scattering time of an individual electron. Since τ_p^* is smaller than the ensemble scattering time τ_p (cf. Eq. 2.8), this simple consideration already suggests a less effective spin diffusion with respect to electron diffusion in 2DEG systems. A more elaborate theoretical discussion has been given by D'Amico and Vignale, who demonstrated that Coulomb interactions give rise to an intrinsic source of friction between spin up and spin down electron populations [95–97]. This so-called spin Coulomb drag (SCD) effect has been shown to be of particular importance for 2D systems [98, 99]. The basic working principle of the SCD effect is sketched in Fig. 2.12. Since a spin current is based on a counterflow of oppositely polarized electrons, it is strongly affected by Coulomb scattering events. Charge currents, on the other hand, are not affected by electron-electron scattering, as the total electron momentum is conserved. The SCD leads to the complete decay of a spin current even in the absence of impurity or phonon scattering, since Coulomb scattering between electrons tends to equalize the average momenta of the spin up and spin down electron ensembles [98, 99].

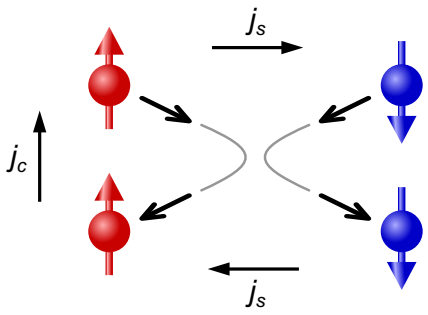

Figure 2.12: General principle of the spin Coulomb drag effect: A spin-up electron (red) and a spin-down electron (blue) interact via Coulomb scattering. Before the scattering event the spin current $\boldsymbol{j}_s$ points to the right; thereafter $\boldsymbol{j}_s$ points to the left. The charge current $\boldsymbol{j}_c$ is not affected by e-e scattering (replotted from [100]).

The SCD effect has been experimentally verified in GaAs/(Al,Ga)As quantum well systems [100, 101]. These experiments show a quite good agreement with the theoretical predictions, with the spin diffusivity D_s being roughly one order of magnitude smaller than the electron diffusivity D_e. An even larger discrepancy between spin and electron diffusion has been measured in Refs. [91, 102]. Here, D_s was reported to be two orders of magnitude smaller than D_e. Although such a large reduction of D_s cannot be explained with the SCD theory alone, the authors of Refs. [91, 102] still regard electron-electron scattering as the main reason for the small D_s.

3. Experimental methods

In this work the spin accumulation in the GaAs-based heterostructures is mainly investigated by employing scanning Kerr microscopy at the cleaved edge of the samples. This measurement technique was developed by Kotissek *et al.* in 2007 [17, 18] and was used afterwards by Endres *et al.* [19–22]. This chapter gives an introduction to this experimental approach. First, it will be shown, how a spin imbalance in the GaAs conduction band can be detected by means of the polar magneto-optic Kerr effect. Subsequently, in Sec. 3.2 the cleaved edge detection technique will be explained, especially focusing on the general sample design and the optical setup. The spatial resolution of the setup and the influence of laser illumination on the electronic system are addressed in Sec. 3.3. The chapter concludes with a discussion of the Hanle effect, which is an important tool to study the dynamical aspects of a spin ensemble.

3.1. Magneto-optic Kerr effect in GaAs

For the polar magneto-optic Kerr effect (pMOKE) measurements the sample is illuminated under normal incidence with a linearly polarized laser beam. After reflection from the surface the polarization plane is tilted by the Kerr angle θ_{K}, which provides a measure for the spin accumulation in the semiconductor. In GaAs-based heterostructures the pMOKE is a consequence of the circular birefringence arising from the spin polarization in the conduction band.

3.1.1. Magneto-optic Kerr effect in bulk GaAs

The origin of the pMOKE in bulk GaAs can be understood by considering the unequal occupation of spin up and spin down states in the conduction band as it is illustrated in Fig. 3.1 on the left hand side. The spin imbalance in the conduction band leads to a difference in the Fermi levels of the two spin populations [103]. This has important consequences for the absorption of photons with energies close to the band gap energy E_{g}. Photons with energies only slightly above E_{g} can exclusively excite transitions into the spin down subband. Transitions into the spin up subband are only possible for photons with larger energies.

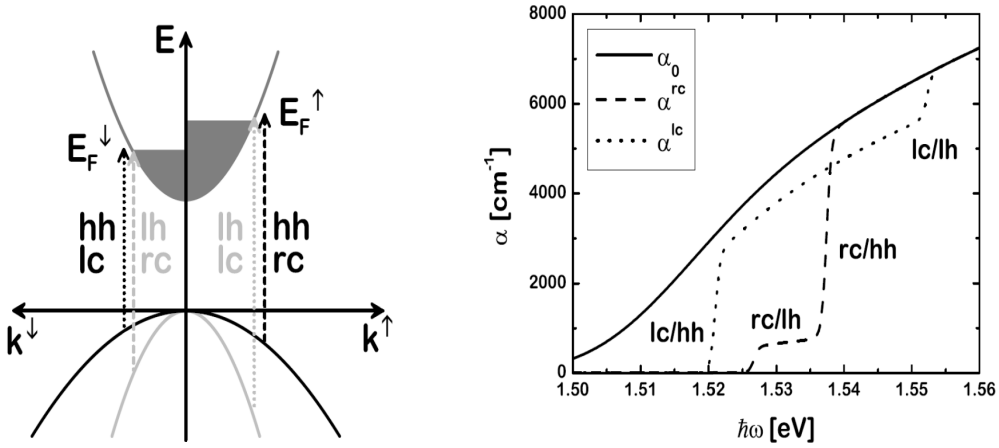

Figure 3.1.: Left: Optical transitions in bulk GaAs for left (lc) and right circularly (rc) polarized light for transitions from the heavy (hh) and light hole (lh) bands into the conduction band (adapted from [103]). Right: Calculated absorption spectrum for $n^{\uparrow} = 1.5 \cdot 10^{17}\,\mathrm{cm}^{-3}$ and $n^{\downarrow} = 0.5 \cdot 10^{17}\,\mathrm{cm}^{-3}$. α_0 denotes the absorption in the unpolarized case (adapted from [103]).

Furthermore, the transitions have to obey the dipole selection rules in GaAs as discussed in Sec. 2.1.1. Therefore, the two circular light modes can only couple to certain transitions. For example, left circularly polarized light can excite a transition from the heavy hole band to the spin down subband, but not from the heavy hole band to the spin up subband [103]. Altogether, the spin imbalance in the conduction band in combination with the optical selection rules causes absorption spectra for left and right circularly polarized light as shown in Fig. 3.1 on the right hand side. The calculated curves clearly reveal a different spectral dependence of the absorption coefficients of the two circular light modes, i.e. the system shows a different response to left and right circularly polarized light. This demonstrates that the spin polarization in the conduction band induces a circular birefringence [103] and for that reason the two circular light modes experience different phase shifts as they propagate through the semiconductor, which results in a rotation of the polarization plane of the incident, linearly polarized light beam.

Figure 3.2 illustrates the expected Kerr rotation spectrum calculated from the absorption coefficients in Fig. 3.1. The Kerr rotation is only non-zero in the vicinity of the GaAs band gap. Moreover, there is a sign reversal in the middle of the spectrum [103]. This shows that the choice of the correct photon energy plays a crucial role for pMOKE measurements in GaAs. Experimentally, it is found that the Kerr rotation spectrum differs slightly from sample to sample. Therefore, the first step in performing pMOKE measurements on an n-GaAs sample is the optimization of the photon energy of the probe laser beam. Most importantly, the calculations of Ref. [103] show, that for a fixed photon energy

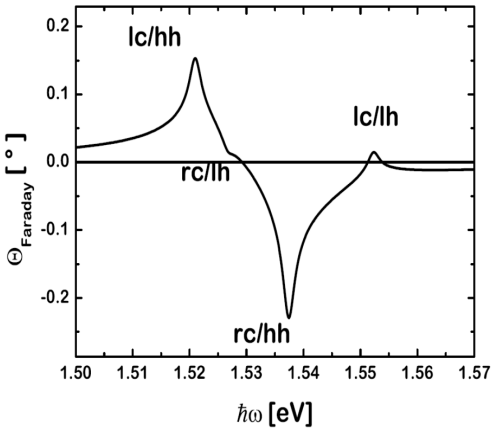

Figure 3.2: Calculated Kerr rotation spectrum for $n^{\uparrow} = 1.5 \cdot 10^{17}\,\mathrm{cm}^{-3}$ and $n^{\downarrow} = 0.5 \cdot 10^{17}\,\mathrm{cm}^{-3}$ at 4.2 K (adapted from [103]).

the Kerr rotation angle θ_{K} is directly proportional to the spin accumulation μ_s in the GaAs conduction band, as long as the electron spin polarization is not too large ($P_n \lesssim 20\%$). As this is always true for the bulk spin injection experiments in this work, θ_{K} directly reflects the spin accumulation μ_s.

3.1.2. Magneto-optic Kerr effect in 2D electron systems

Apart from spin injection experiments into bulk GaAs this work also presents results on spin injection into two-dimensional electron systems. Performing optical measurements on such systems is not as straightforward as performing pMOKE measurements on bulk GaAs samples, as the reduced symmetry of the 2DEG might have a severe influence on the optical selection rules and therefore on the strength of the pMOKE. Indeed, it has been shown that in narrow (some 10 nm wide) GaAs/(Al,Ga)As quantum well (QW) systems the confinement potential forces both the orbital angular momentum and the spin angular momentum of the heavy hole states in the valence band into an out-of-plane direction perpendicular to the QW plane [104, 105]. Furthermore, the confinement lifts the degeneracy of the heavy and light hole states at the Γ-point, shifting the light hole band to lower energies (see Fig. 3.3). Taking both into account, only the out-of-plane polarized heavy holes can contribute to recombination processes with electrons in the conduction band. This has substantial consequences for magneto-optical processes. In the case of an in-plane polarized electron spin polarization angular momentum conservation prohibits the recombination of an electron with a heavy hole under emission of circularly polarized light with a well-defined helicity. Instead, only linearly polarized light will be detectable.

This effect has been verified in spin-LED experiments by a direct comparison of the circular polarization of the electroluminescence in top-emission (with the electron spin polarization oriented perpendicular to the QW) and edge-emission (with the electron spin polarization in the plane). For 10 nm and 15 nm wide QWs

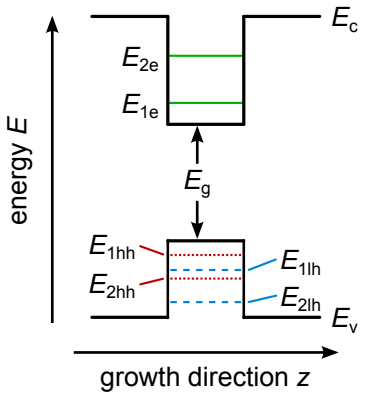

Figure 3.3: Sketch of an (Al,Ga)As/GaAs/(Al,Ga)As quantum well heterostructure. The E_{ne} represent the quantized energy states of the electrons in the conduction band. The $E_{n\mathrm{hh}}$ and $E_{n\mathrm{lh}}$ are the energy states of the heavy and light holes in the valence band, respectively.

no significant circular polarization was found with the edge-emission geometry, although a strong signal was measured in top-emission [51, 106]. For wide (bulk-like) QWs ($d \geq 50\,\mathrm{nm}$), however, a circular polarization can even be detected in edge-emission, indicating that the heavy hole spin obtains in-plane components due to the weakened quantum confinement compared to narrow QWs [51, 105]. So, for wide GaAs/(Al,Ga)As-QW systems the optical selection rules should still allow magneto-optical effects in edge-emission, but with a reduced efficiency compared to bulk GaAs.

The situation changes if one uses a two-dimensional electron gas, which is confined at a GaAs/(Al,Ga)As interface, as it is the case in the present experiments. In such a system only the electrons in the conduction band are confined within a triangular potential well; the holes in the valence band are not confined at all, except of the (Al,Ga)As-barrier right at the interface (see Fig. 2.2 on the right hand side). Therefore, neither is the degeneracy of the light and heavy holes at the Γ-point lifted, nor is there a confinement which forces the hole spins in the out-of-plane direction. The holes will behave like ordinary bulk holes. Hence, the optical selection rules in the 2DEG will be qualitatively unchanged with respect to bulk GaAs and the magneto-optic Kerr effect in edge-emission will be significant.

3.2. Cleaved edge detection of spin accumulation

In this work the spin accumulation in the GaAs is detected by performing pMOKE measurements at the cleaved edge of the sample. The basic idea behind this approach is illustrated in Fig. 3.4. The samples are fabricated in such a way, that they provide optical access to the semiconductor heterostructure from the side of the sample. Thus, by focusing the probe laser beam on the sample edge and utilizing pMOKE detection, it is possible to perform spatially resolved measurements of the spin accumulation in the semiconductor. In particular, the spin density can

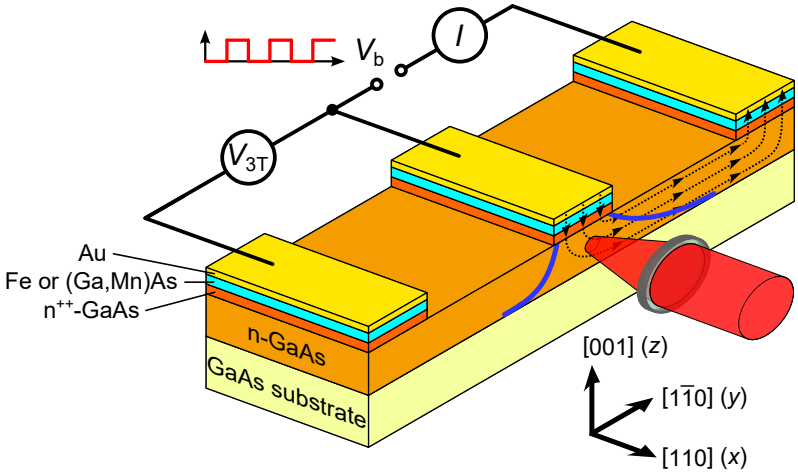

Figure 3.4.: General sample design for spin injection experiments into GaAs-based semiconductor heterostructures. A spin imbalance in the semiconductor can be generated by applying a bias voltage between the center ferromagnetic contact and one of the reference contacts. The spin accumulation can be detected via pMOKE measurements at the cleaved edge of the sample. The dotted arrows indicate the current flow in the sample. The blue solid lines represent the exponentially decaying spin accumulation in the semiconductor channel.

be observed even directly underneath the spin injecting contacts; in that respect the cleaved edge detection approach is superior to other measurement schemes (like e.g. pMOKE experiments from the top of the sample or nonlocal spin valve measurements), which typically are only sensitive to the spin accumulation next to the injector contact.

The samples used for the experiments were grown by molecular beam epitaxy (MBE) on semi-insulating GaAs(001) substrates. The semiconductor layers (GaAs, (Al,Ga)As and (Ga,Mn)As) were grown by Dr. D. Schuh from the group of Prof. Dr. D. Bougeard in a III-V semiconductor MBE system. Fe and Au films were prepared by Dr. M. Kronseder from the group of Prof. Dr. C. H. Back in a metal MBE chamber. Since the two MBE systems are connected to each other, samples can be transfered from the semiconductor MBE to the metal MBE chamber without breaking the vacuum, which is of particular importance for the growth of the Fe/GaAs junctions. A spin imbalance is created and analyzed in both two-dimensional and three-dimensional electron systems. The layer stacks of the corresponding heterostructure wafers are quite different from one another; however, in both cases the heterostructures essentially consist of the same two main elements: an n-conducting semiconductor layer, which serves for the electron transport and the spin accumulation, and a ferromagnetic tunnel junction, which is used to drive a spin-polarized current into the transport layer below. In the case of the bulk GaAs spin injection devices (see Fig. 3.4) a micrometer thick

layer of Si-doped n-GaAs is used for the electron transport layer. The doping density of the n-GaAs is chosen slightly above the metal-to-insulator transition (at about $2 \cdot 10^{16}\,\mathrm{cm}^{-3}$) to ensure a metallic conductance and a large spin lifetime. On top of the n-GaAs a 15 nm thick n $\rightarrow$ n^{++} transition layer, 10 to 15 nm n^{++}-GaAs ($N_\mathrm{D} \sim 5 \cdot 10^{18}\,\mathrm{cm}^{-3}$) and a thin layer of Fe are grown. The gradual increase of the doping density at the Fe/GaAs interface leads to the formation of a narrow Schottky barrier, which allows to drive a sizable spin current into the n-GaAs. For the spin injection experiments into a two-dimensional electron gas, on the other hand, an (Al,Ga)As/GaAs heterojunction is used to confine a 2DEG at its interface, and a (Ga,Mn)As/GaAs Esaki tunnel barrier is used as source for the spin current. Since the exact layer stack differs from wafer to wafer, details on layer thicknesses and doping densities are given later in Chap. 4 together with the experimental results.

Samples are patterned utilizing standard lithography techniques. The general sample design is sketched in Fig. 3.4. The electron transport in the semiconductor is confined to a channel, which has two large reference contacts at its ends. The ferromagnetic contacts, which are used to induce the spin imbalance in the semiconductor channel, are fabricated in the center of the transport channel. Details on the sample geometry and the micro-fabrication process will be presented later in Chap. 4. After patterning the samples they are cleaved along the electron transport channel as shown in Fig. 3.5. To this end the sample surface is scratched with a diamond scriber at the outer edge of the sample, far away from the patterned structures. The scratch defines the predetermined cleaving direction and thus has to be oriented along the channel direction. Since GaAs(001) substrates preferentially break along the $[1\bar{1}0]$ and [110] crystallographic directions, care has to be taken that the transport channels are oriented along either of these two directions. After scratching the sample surface, the sample is put upside down on the concavely curved surface of a wafer transport box. By gently pressing with a scalpel on its rear side, the sample breaks along the transport channel into two halves. As a result a clean and crystallographically perfect GaAs(110) or GaAs($1\bar{1}0$) surface is exposed at the cleaved edge plane, suitable for optical experiments as depicted in Fig. 3.4.

The polar magneto-optic Kerr effect is exclusively sensitive to the component of the spin polarization along the laser beam direction (= x-axis, cf. Fig. 3.4). Thus, since the injected spin density is polarized along the magnetization direction of the ferromagnetic contact, one has to take care, that the remanent magnetization of the contact has a non-zero component along the x-axis. The magnetic easy axis of thin Fe films on GaAs(001) is oriented along the [110] crystallographic direction [107]. Thus, when Fe is used as spin aligner, the transport channel is fabricated along the $[1\bar{1}0]$ direction. In this way the remanent magnetization of the injector contact is aligned perpendicularly to the cleaved edge plane and thereby the injected spin ensemble is fully polarized along the sensitive direction

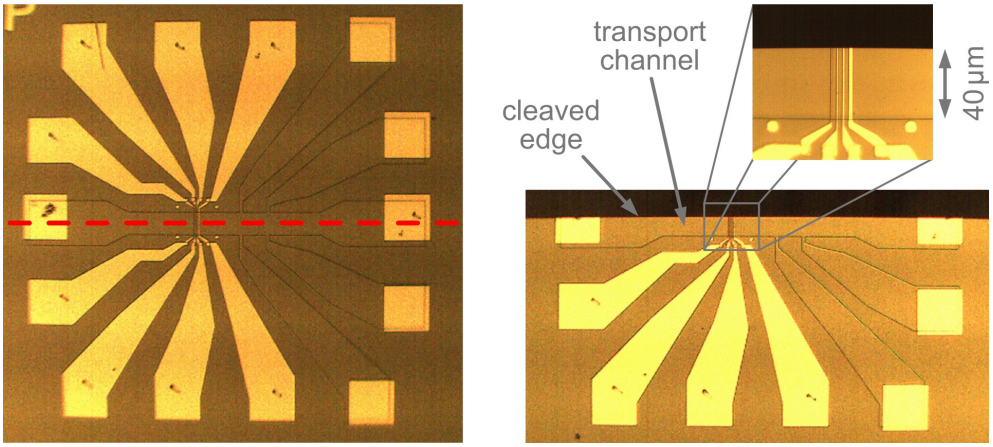

Figure 3.5.: Left: Micrograph of a sample prior to cleaving. The red dashed line indicates the desired cleaving direction along the 50 µm wide mesa channel. Right: Sample after the cleaving process. The zoomed view on the upper right shows the narrow spin injecting contacts at the cleaved edge.

of the experiment. (Ga,Mn)As, on the other hand, has a more complicated magnetic anisotropy in the (001) plane. To a first approximation (Ga,Mn)As has at low temperatures a biaxial magnetic anisotropy with the magnetic easy axes along the in-plane ⟨100⟩ directions [108, 109]. In addition, for the narrow spin injecting contacts used in this work (see the zoomed view in Fig. 3.5) a change of the anisotropy due to a patterning induced strain relaxation has to be taken into account as well [110, 111]. Altogether, the remanent magnetization direction of a (Ga,Mn)As contact is found to be oriented in between the [110] and [1$\bar{1}$0] directions [22, 112] and therefore, the injected spin density has always a non-zero component along the laser beam axis for both [110]- and [1$\bar{1}$0]-cleaved samples.

Figure 3.6 shows a schematic representation of the optical setup. The samples are mounted in vacuum ($p < 10^{-5}$ mbar) on the cold finger of a He flow cryostat, which can be cooled to about 10 K. The samples are located roughly 1 mm underneath the cryostat window with the cleaved edge plane facing upwards. The cryostat is mounted on top of a piezo stage, which itself is attached to an xy table. The piezo stage has a travel range of 100 µm along the axes of the cleaved edge plane of the sample. Thus, by scanning the sample underneath a static laser beam two-dimensional maps of the cleaved edge plane can be made.

For the pMOKE measurements of the electron spin polarization a cw diode laser is used. The photon energy E_{photon} of the laser can be tuned in the range between 1.44 eV and 1.54 eV. Thus, it can be chosen in the vicinity of the GaAs band gap E_{g} (about 1.518 eV at 10 K), which is necessary to optimize the magneto-optic Kerr response of the sample, as discussed in Sec. 3.1. The laser light is guided via several broadband dielectric mirrors to a pellicle beam splitter. Here, roughly

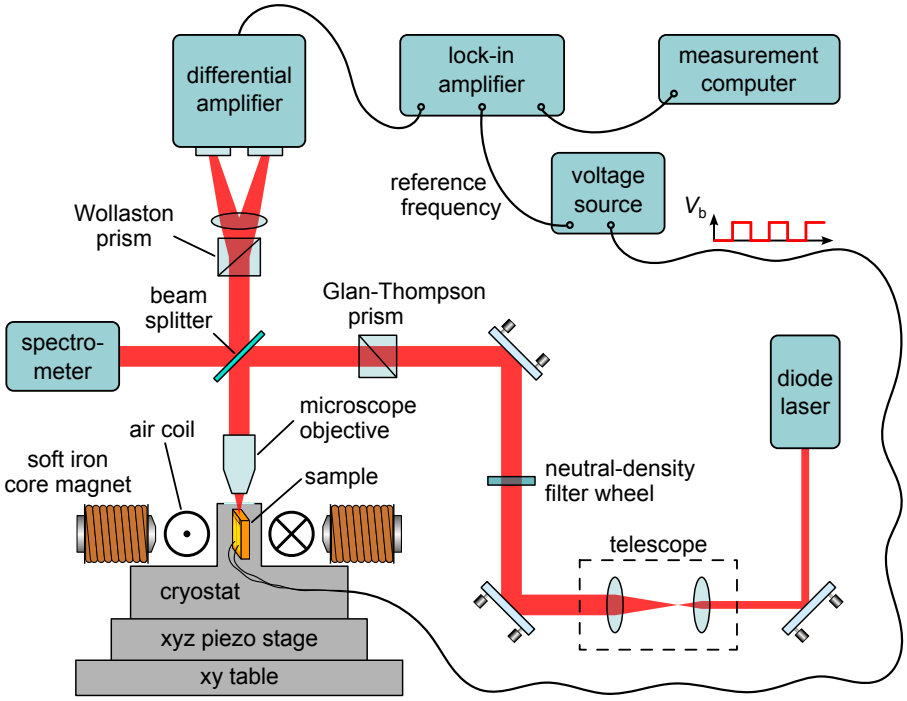

Figure 3.6.: Sketch of the scanning Kerr microscope. The operating principle is described in the text.

90% of the light are transmitted and reach a spectrometer, which is used to determine the laser wavelength. The remaining 10% of the light are reflected to a microscope objective, which focuses the light onto the sample in the cryostat. The objective has a magnification factor of 60, a numerical aperture of 0.70 and a working distance of about 2.5 mm. In order to obtain the smallest possible laser spot diameter on the cleaved edge plane, one has to make sure that the whole aperture of the microscope objective is uniformly illuminated. For that reason, the light beam is widened with a telescope after leaving the diode laser. The light intensity on the sample can be controlled with the aid of a neutral-density filter wheel. For the measurements a probe laser power of approximately 10 µW is used. The laser light is linearly polarized with a Glan-Thompson prism before it hits the sample. Upon reflection from the sample surface the polarization plane of the light is rotated by the Kerr angle θ_K, which is detected by splitting the reflected light with a Wollaston prism into two orthogonally polarized beams and measuring the corresponding intensity difference with a differential amplifier. This difference signal is directly proportional to the Kerr angle and thus also to the spin polarization in the GaAs conduction band.

The magnetization of the ferromagnetic contacts as well as the spin ensemble in the GaAs can be manipulated with two electromagnets, which are located outside the cryostat with the sample sitting in their center, as illustrated in Fig. 3.6. The

air coil magnet is used to switch the magnetization of the injector contact along the sensitive direction of the laser beam (= x-axis, cf. Fig. 3.4). Thus, after switching off the magnetic field it allows to carry out spin injection along the two corresponding remanent magnetization directions of the injector contact. The soft iron core magnet, on the other hand, generates a field in z-direction (= out-of-plane direction of the sample), and is used to perform Hanle depolarization measurements, which will be discussed later in Sec. 3.4.

For the spin injection experiments a unipolar square-wave bias voltage alternating between zero and V_b is applied between a spin injecting contact in the middle of the transport channel and a reference contact at the channel end (see Fig. 3.4). In this way the electron spin accumulation in the semiconductor is periodically switched on and off and thus can be detected phase-sensitively using a lock-in amplifier. Besides the enhanced signal-to-noise ratio the lock-in technique offers the great advantage, that the (quasi-static) magnetization of the ferromagnetic injector contact cannot contribute to the measured Kerr signal; moreover, Faraday effects occuring in the cryostat window or the microscope objective are not detected as well [22]. Fig. 3.7 shows on the left hand side a measurement of the Kerr rotation angle θ_K as a function of the external magnetic field H_x while applying a positive bias voltage V_b to an Fe contact. The signal was detected with the laser spot being located on the n-GaAs channel directly underneath the spin extracting contact. The measured hysteresis loop reflects the magnetization reversal of the Fe contact along its easy axis and thus provides a direct proof for electron spin extraction from the semiconductor into the ferromagnet. Usually the hysteresis curve is not symmetrically centered around $\theta_\mathrm{K} = 0$. The offset can be explained with a not spin-related, electro-optic contribution to the Kerr effect, caused by the square-wave modulated injection current flowing through

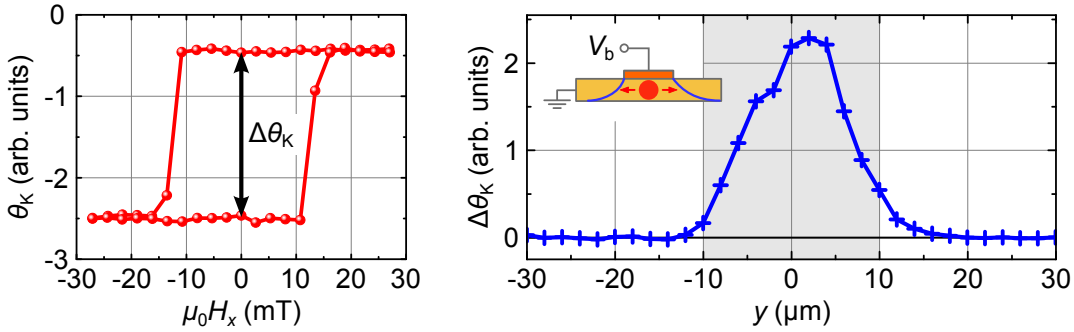

Figure 3.7.: Left: Kerr rotation θ_K in the n-GaAs channel as a function of the applied magnetic field H_x for electron spin extraction from the n-GaAs into an Fe contact. The height of the hysteresis loop in remanence, $\Delta\theta_\mathrm{K}$, is a measure for the spin accumulation in the semiconductor. Right: Linescan of $\Delta\theta_\mathrm{K}$ along the n-GaAs channel. The injector contact position is indicated by the shaded region. The inset illustrates the current path within the sample and the scan direction of the laser spot.

the GaAs. However, the height of the hysteresis loop in remanence, $\Delta\theta_K$, is still strictly proportioanl to the spin density in the GaAs [18, 22]. For that reason, the spin injection experiments are performed in remanence, after saturating the spin aligning contact in $+x$ and $-x$-direction, respectively and taking the difference of both remanent θ_K-values, $\Delta\theta_K$, as a measure for the spin accumulation. Fig. 3.7 displays on the right hand side the spatial dependence of $\Delta\theta_K$ in the n-GaAs channel underneath the spin extracting Fe contact. The measurement was obtained by scanning the laser spot along the cleaved edge plane underneath the contact. The Kerr rotation data directly map the spin density distribution in the n-GaAs channel, illustrating the decay of the spin accumulation outside the contact region.

3.3. Resolution and optically created carrier density

The spatial resolution of the optical setup is determined by the diameter of the laser spot on the cleaved edge plane. The spot size can be estimated by measuring the reflected light intensity while scanning the laser in z-direction across the sample edge (see Fig. 3.8 on the top). From a mathematical point of view, the resulting measurement represents the convolution of the laser spot profile with the sample topography. Since the topography of the cleaved edge plane along the z-axis can be well described by a Heaviside step function, the deconvolution can be performed by simply calculating the derivative of the reflected light intensity. Fig. 3.8 shows on the bottom the resulting, deconvolved laser spot profile. The laser beam has a Gaussian shape with a full width at half maximum (FWHM) of about (0.68 ± 0.02) µm. This value is the minimum achievable laser spot diameter for the present setup.

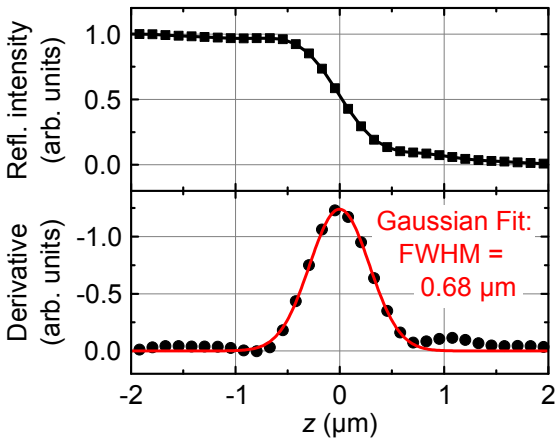

Figure 3.8: Top: Measurement of the reflected light intensity while scanning the laser across the cleaved sample edge. Bottom: The derivative of the reflected light intensity corresponds to the laser spot profile. A Gaussian fit yields a minimum laser spot diameter of about (0.68 ± 0.02) µm.

For the spin injection experiments into bulk GaAs it is sufficient to focus the laser to a spot size of about 1 µm, because the n-GaAs transport channels are grown with thicknesses larger than 1 µm. Moreover, the spin diffusion length in n-GaAs is typically of the order of several micrometers and thus also well above the diameter of the laser spot. For spin injection into the two-dimensional electron gas systems, on the contrary, the electrons in the 2DEG are confined to a width of only several 10 nm along the z-direction. Thus, here it is extremely important that the laser is focused as well as possible in order to obtain a sizable Kerr signal. This difficulty will be discussed in more detail in Sec. 4.2 in conjunction with the corresponding experimental results.

Because of the necessity to use a well focused laser spot, even a small probe laser power of 10 µW may cause a large light intensity on the cleaved edge of the sample. Moreover, since the laser has to be tuned to the vicinity of the GaAs band gap for the pMOKE measurements, laser illumination continuously creates electron-hole pairs in the sample and therefore increases the carrier density in the conduction band. Thus, the question arises as to what extent the electronic system in the sample is disturbed by the laser illumination. In order to answer this question the optically generated charge carrier density is estimated following a calculation presented previously in Ref. [22]:

GaAs has a refractive index of about 3.6 for photon energies near the band gap [113, 114]. Therefore, 32% of the laser light are reflected at the cleaved edge plane of the sample. The remaining 68% of the incident 10 µW laser power are transmitted into the semiconductor and are finally absorbed. The laser power density in the GaAs depends on the laser spot diameter and the penetration depth of the light. As 50% of the light intensity of a Gaussian laser spot are located within the FWHM of the spot profile ($\approx 0.7\,\mu$m, see above), the absorbed laser power per area is calculated to be of the order of $9\,\mu\mathrm{W}/\mu\mathrm{m}^2$. The penetration depth of the laser is determined by the absorption coefficient of the GaAs, which is known to show a strong dependence on the photon energy close to the band gap. For a wavelength of 825 nm, for instance, the absorption coefficient is of the order of $100\,\mathrm{cm}^{-1}$ [115], which corresponds to a penetration depth of 100 µm. Assuming an exponential decay of the light intensity in the GaAs, one finds therefore an average absorbed power density G of the order of $0.06\,\mu\mathrm{W}/\mu\mathrm{m}^3$ within the penetration depth of the light. From that, the optically generated, additional charge carrier density can be estimated via [22]

$$n_{\mathrm{opt}} = \frac{G}{E_{\mathrm{photon}}} \cdot \tau_{\mathrm{r}}, \tag{3.1}$$

where $\tau_{\mathrm{r}} \approx 1\,\mathrm{ns}$ [116–118] is the recombination lifetime in GaAs. This rough estimation results in $n_{\mathrm{opt}} \approx 2.5 \cdot 10^{14}\,\mathrm{cm}^{-3}$ for a wavelength of 825 nm. For 819 nm the optically created electron density is roughly one order of magnitude larger, as

this wavelength is closer to the band gap of the GaAs and thus the penetration depth is roughly one order of magnitude smaller [22]. This calculation shows, that for photon energies close to the band gap energy the additional electron density n_{opt} is at least one order of magnitude below the metal-to-insulator transition in GaAs (at about $2 \cdot 10^{16}\,\mathrm{cm}^{-3}$) and thus small compared to the doping densities of the investigated samples. Therefore, the optically generated electron density should have a negligible influence on the electron distribution in the samples. Indeed, it has already been shown by B. Endres that laser illumination with this light intensity does not notably disturb the spin accumulation in the GaAs conduction band. Moreover, even a one order of magnitude larger laser power was found to leave the electron spin polarization unaffected [22].

3.4. Hanle effect

The Hanle effect provides a useful tool to study the dynamic properties of the spin accumulation. In particular, it can be used to extract a value for the spin relaxation time τ_s. The basic measurement procedure, as sketched in Fig. 3.9, rests on the depolarization of the injected spin density in an external magnetic field, which is applied perpendicular to the spin injection direction. The detection of the spin signal occurs usually on the diffusion side at a certain distance to the injector contact, either by employing optical detection via pMOKE or by using a second ferromagnetic contact, which allows an electrical detection in a nonlocal measurement geometry. The injected spin ensemble performs Larmor precessions about the magnetic field. Due to their diffusive motion different electrons need different time spans to reach the detection position and thus they arrive with different precession angles. As a result, the projection of the spin density along the sensitive direction of the experiment (= x-axis, cf. Fig. 3.9) is suppressed with increasing magnetic field [25, 27, 43].

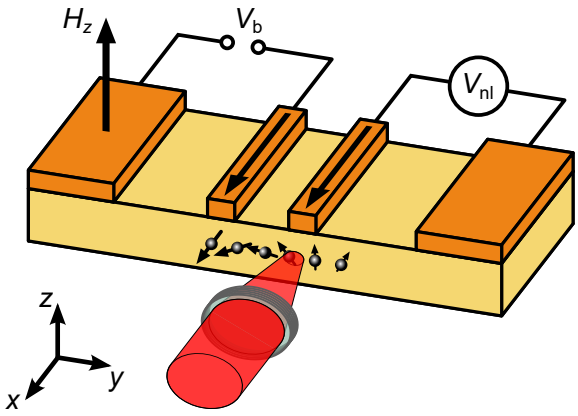

Figure 3.9: Measurement geometry for the Hanle effect. While precessing around an externally applied magnetic field H_z, the injected spin ensemble diffuses from the injector contact to the detection position.

The dependence of the spin polarization on the magnetic field can often be described by a Lorentzian-like curve (see Fig. 3.10), whose width is determined by the spin lifetime τ_s. For a short spin lifetime, for instance, the electrons can only acquire small precession angles within τ_s. Thus, the precession angles of the spins, which reach the detection position, differ only slightly from each other and the suppression of the spin density is small, resulting in a wide Hanle curve. In contrast, electrons with a long spin lifetime can gather large precession angles within τ_s, leading to a strong suppression of the spin signal at the detection position and thus a narrow Hanle curve.

3.4.1. Isotropic spin relaxation

In many cases, the spin dynamics of the Hanle effect can be well described with a one-dimensional model including spin precession, spin diffusion and spin relaxation [43]:

$$\frac{\partial \boldsymbol{s}}{\partial t} = \boldsymbol{s} \times \boldsymbol{\omega_0} + D_s \frac{\partial^2 \boldsymbol{s}}{\partial y^2} - \frac{\boldsymbol{s}}{\tau_s}. \tag{3.2}$$

This model assumes an isotropic spin relaxation with one spin relaxation time τ_s for all components of the spin density $\boldsymbol{s}$. The anisotropic case will be discussed in Sec. 3.4.2. Since in the experiment spins are injected continuously, one has to look for steady-state solutions of Eq. 3.2, i.e. the time derivative has to be taken to zero. Assuming that spins polarized along the x-direction are injected at position $y = 0$, the solution for the spatial spin profile reads [43]:

$$s_x(y) = J_0 \cdot \exp\left(-\frac{\alpha_1}{\lambda_s} y\right) \left[\frac{\alpha_1}{\alpha_1^2 + \alpha_2^2} \cos\left(\frac{\alpha_2}{\lambda_s} y\right) - \frac{\alpha_2}{\alpha_1^2 + \alpha_2^2} \sin\left(\frac{\alpha_2}{\lambda_s} y\right)\right] \tag{3.3}$$

with the parameters

$$\alpha_{1,2} = \frac{1}{\sqrt{2}} \sqrt{\sqrt{1 + (\omega_0 \tau_s)^2} \pm 1}. \tag{3.4}$$

This equation can be used to fit Hanle curves, which have been measured at a distance y next to the injector contact. The external magnetic field B enters through the Larmor precession frequency $\omega_0 = g\mu_B B/\hbar$ where for the g-factor the value of bulk GaAs ($g = -0.44$ [119, 120]) is used. The diffusivity is included in the spin diffusion length $\lambda_s = \sqrt{D_s \tau_s}$. Equation 3.2 suggests that D_s and τ_s are the two fundamental fitting parameters of Hanle depolarization experiments. However, λ_s can be obtained from independent linescan measurements along the cleaved edge of the sample and thus τ_s and the scaling factor J_0 are the only remaining fitting parameters [22]. Fig. 3.10 displays an example for a Hanle depolarization measurement of a bulk GaAs sample, which has been modeled with Eq. 3.3. In this case the Hanle curve is almost perfectly Lorentzian.

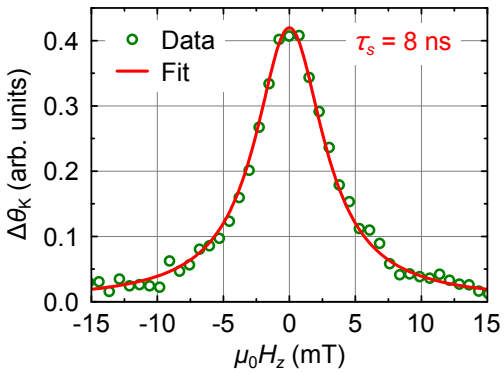

Figure 3.10: Hanle depolarization curve of a spin ensemble in bulk n-GaAs. The fit yields a spin lifetime of about 8 ns.

The considerations so far assumed that the injected spin density is initially polarized along the sensitive direction of the experiment. This is true for pMOKE detection when an Fe contact is used as spin aligner, since the magnetic easy axis of thin Fe films on GaAs(001) is oriented along the [110] direction [107], which can be chosen to be perpendicular to the cleaved edge of the sample. (Ga,Mn)As, on the other hand, shows a more complicated magnetic anisotropy, as was already discussed above in Sec. 3.2. Here, the remanent magnetization direction is in general tilted by an angle ϕ with respect to the x-axis. For that reason the resulting Hanle curves have an asymmetric shape (see Fig. 3.11 on the right hand side) and cannot be fitted with Eq. 3.3 any more. It has been demonstrated by B. Endres that Hanle data resulting from a tilted (Ga,Mn)As magnetization can be analyzed by additionally taking the y-component of the spin density [43]

$$s_y(y) = J_0 \cdot \mathrm{sgn}(\omega_0) \cdot \exp\left(-\frac{\alpha_1}{\lambda_s} y\right) \left[\frac{\alpha_1}{\alpha_1^2+\alpha_2^2} \sin\left(\frac{\alpha_2}{\lambda_s} y\right) + \frac{\alpha_2}{\alpha_1^2+\alpha_2^2} \cos\left(\frac{\alpha_2}{\lambda_s} y\right)\right] \tag{3.5}$$

into account. The general fitting function then reads [22]:

$$s_x(\phi, y) = \cos(\phi) \cdot s_x(y) + \sin(\phi) \cdot s_y(y), \tag{3.6}$$

where the tilt angle ϕ is used as an additional fitting parameter. Fig. 3.11 shows an example for such an asymmetric Hanle measurement. The non-rectangular hysteresis loop of the spin accumulation proves that the magnetization of the (Ga,Mn)As contact is indeed tilted with respect to the x-axis. The resulting asymmetric Hanle curve can be well fitted with Eq. 3.6.

3.4.2. Anisotropic spin relaxation

Up to now the Hanle effect has been discussed for systems with isotropic spin dephasing (e.g. bulk GaAs). Spin relaxation in a (001)-grown 2DEG, however, shows a pronounced spin lifetime anisotropy in the quantum confinement plane (see Sec. 2.3.3). For the Hanle measurements in this work the external magnetic

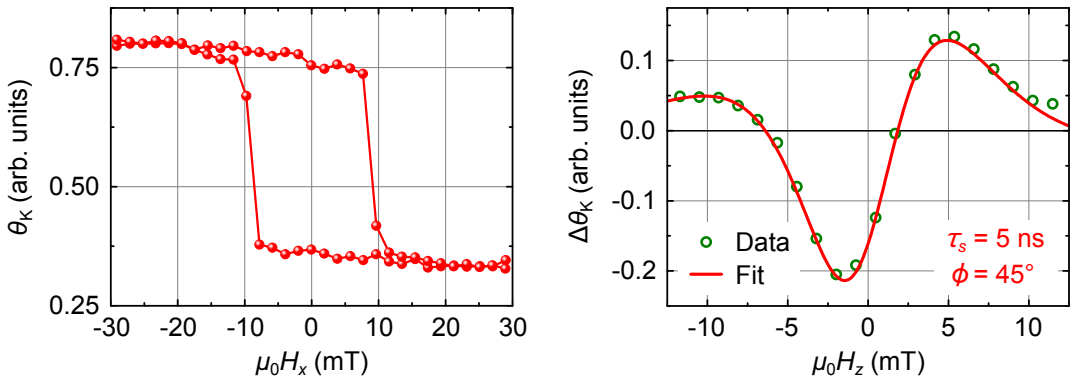

Figure 3.11.: Left: Hysteresis loop of a spin accumulation in bulk n-GaAs for electrical spin injection. The non-rectangular shape of the hysteresis loop indicates an in-plane tilt of the magnetization direction of the (Ga,Mn)As contact with respect to the sensitive axis of the laser beam (= x-axis). Right: Corresponding asymmetric Hanle depolarization curve. The fit yields a tilt angle of 45°.

field is applied along the [001] direction. Thus, the spin accumulation precesses in the (001) plane and probes all relaxation times in the different in-plane directions. Neglecting spin diffusion the resulting Hanle lineshape has a simple analytical solution, which is derived in appendix A:

$$s_x(\omega_0) = \frac{s_0 \tau_x}{1 + (\omega_0 \sqrt{\tau_x \tau_y})^2} \cdot \Big(\cos(\phi) + \omega_0 \tau_y \sin(\phi) \Big). \tag{3.7}$$

Here, τ_x and τ_y are the spin lifetimes along the in-plane x- and y-directions, respectively, and ϕ again allows an in-plane tilt of the easy axis of the injecting contact with respect to the x-axis. Just like in the case of isotropic spin dephasing, the Hanle curve has a Lorentzian shape. However, here its width is determined by $\sqrt{\tau_x \tau_y}$. Note that in Eq. 3.7 τ_x and τ_y cannot be used as independent fitting parameters[1]; only their geometric mean $\sqrt{\tau_x \tau_y}$ remains as a useful fitting parameter. As a result, the spin lifetime extracted from Hanle measurements is given by $\tau_s = \sqrt{\tau_x \tau_y}$ [86, 91].

Equation 3.7 does not take spin diffusion into account. Therefore, it is not fully appropriate to use it as a fitting function for the Hanle experiments within this work. For the general case with diffusion one has to find the solutions of the equation

$$\boldsymbol{s} \times \boldsymbol{\omega_0} + D_s \frac{\partial^2 \boldsymbol{s}}{\partial y^2} - \hat{\boldsymbol{\Gamma}} \boldsymbol{s} = 0, \tag{3.8}$$

where the tensor $\hat{\boldsymbol{\Gamma}}$ describes the anisotropic spin relaxation. However, in contrast to the isotropic case discussed in the last section, this equation has no simple

[1] τ_x and τ_y are highly correlated, since the initial spin density s_0 is in general unknown and has to be used as an open scaling factor.

analytical solutions in the form of Eqs. 3.3 and 3.5 anymore[2]. Fig. 3.12 shows some calculated solutions for spin injection along the x-direction for several values of the spin dephasing anisotropy SDA $= \tau_x/\tau_y - 1$. For all calculations the geometric mean of the relaxation times τ_x and τ_y was fixed at $\tau_s^{\mathrm{geom}} = \sqrt{\tau_x\tau_y} = 1.0\,\mathrm{ns}$. The blue curve (SDA $= 0$) illustrates the isotropic case with $\tau_x = \tau_y$. With increasing anisotropy the amplitude of the Hanle curves increases, as the spins are injected along a direction with increasing spin lifetime, which in turn increases the total spin accumulation; however, the general shape of the Hanle curves remains Lorentzian-like. Most importantly, the widths of the curves do not change much even for large anisotropies, suggesting that the width is still determined by $\sqrt{\tau_x\tau_y}$.

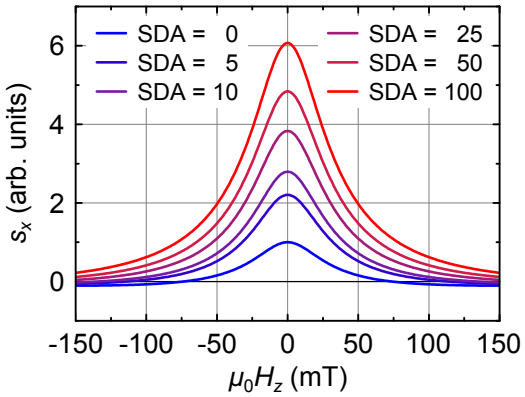

Figure 3.12: Calculated Hanle depolarization curves for spin injection along the x-direction (parameters: $\tau_s^{\mathrm{geom}} = 1.0\,\mathrm{ns}$, $D_s = 100\,\mathrm{cm}^2/\mathrm{s}$, $y = 3.0\,\mu\mathrm{m}$). The curves are shown for several values of the spin dephasing anisotropy SDA $= \tau_x/\tau_y - 1$.

It turns out that fitting the experimental data with this anisotropic model yields no benefit with respect to the isotropic fitting formula. Both methods fit the data equally well, resulting in identical values for the spin diffusivity D_s. Moreover, just like in the diffusion-free case, the anisotropic model does not allow to extract independent values for τ_x and τ_y; the fitting parameters are still highly correlated with their geometric mean being equal to the spin lifetime τ_s extracted with the isotropic model. Thus, it is justified to use the isotropic model, Eq. 3.6, to fit the Hanle data from the 2DEG samples, bearing in mind that the obtained spin lifetime τ_s represents (approximately) the geometric mean of the relaxation times along the two in-plane principal directions:

$$\tau_s \approx \sqrt{\tau_x\tau_y}. \tag{3.9}$$

As a final note it is worth to point out the difference between time-resolved experiments and steady-state Hanle measurements: at the end of Sec. 2.3.3 it has been shown that a spin ensemble, which precesses in a plane with a twofold spin relaxation anisotropy, decays exponentially with the decay time given by the harmonic mean $\bar{\tau}$ of the two in-plane spin lifetimes τ_x and τ_y (cf. Eqs. 2.13 ff.). Thus,

[2]Indeed, Eq. 3.8 still has analytical solutions. However, these solutions are quite lengthy and to the best of the authors knowledge, there is no simple substitution of the form $\tau_s = \sqrt{\tau_x\tau_y}$ or similar, that would transform them into the form of Eqs. 3.3 and 3.5.

although in both cases the spin accumulation performs the same precessional motion, time-resolved measurements are sensitive to the harmonic mean $\bar{\tau}$ of τ_x and τ_y, whereas Hanle measurements yield a value for the geometric mean $\sqrt{\tau_x \tau_y}$.

4. Experimental results

This chapter presents the results of the spin injection experiments. It starts with a discussion of electrical spin injection into bulk n-GaAs using Fe as spin aligning contact. The basic properties like spin diffusion length, spin lifetime and diffusivity will be addressed. Sec. 4.2 continues with experiments on electrical spin injection into a two-dimensional electron gas confined at a GaAs/(Al,Ga)As interface. The electrical and optical properties of the 2DEG will be discussed and the spin accumulation is analyzed using both magneto-optical and electrical detection schemes. Finally, Sec. 4.3 reports on experiments, which aim to generate a spin imbalance in bulk GaAs via a temperature difference between ferromagnet and semiconductor utilizing Seebeck spin tunneling.

4.1. Electrical spin injection into n-GaAs

This section demonstrates electrical spin injection into a 2 µm thick channel of bulk GaAs. The spin accumulation is analyzed by pMOKE measurements at the cleaved edge of the sample. The findings for spin diffusion length λ_s and spin lifetime τ_s are in quite fair agreement with former spin injection experiments into similarly doped n-GaAs using electrical [68,112] and magneto-optical [19,22] detection methods.

4.1.1. Sample

The layer stack of the heterostructure wafer, that was used for the present experiments, is sketched in Fig. 4.1 on the left hand side. The sample consists of a 2 µm thick layer of n-GaAs with a doping density of $N_\mathrm{D} = 4 \cdot 10^{16}\,\mathrm{cm}^{-3}$, which is grown on top of an undoped GaAs(001) substrate. The n-GaAs is used for the electron transport and for the spin accumulation. On top of that follow a 15 nm thick $\mathrm{n} \rightarrow \mathrm{n}^{++}$ transition layer with gradually increasing doping density, a 10 nm thick layer of n^{++}-GaAs ($N_\mathrm{D} = 4 \cdot 10^{18}\,\mathrm{cm}^{-3}$) and a 2 nm thick layer of Fe, which is capped with 5 nm Au to prevent its oxidation. The Fe/n^{++}-GaAs layers form a narrow Schottky barrier, which enables the tunneling of spin-polarized carriers from the Fe into the n-GaAs.

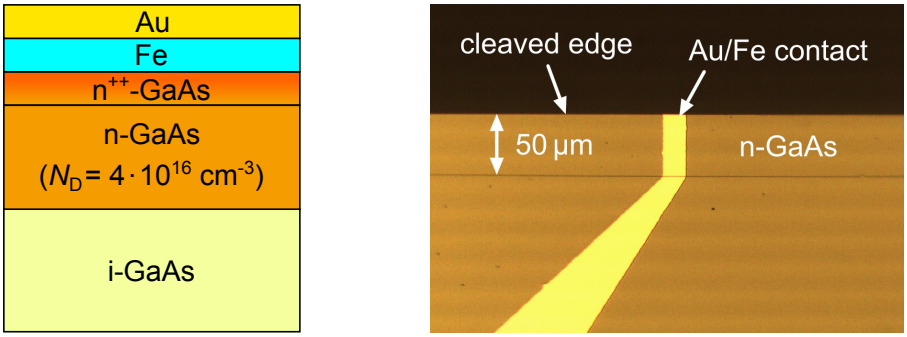

Figure 4.1.: Left: Layer stack for electrical spin injection from Fe into n-GaAs. Right: Micrograph of the cleaved sample showing the 50 µm wide mesa channel and a 20 µm wide Au/Fe contact.

Sample fabrication was performed in the yellow room of Prof. Dr. C. H. Back and the clean room of Prof. Dr. D. Weiss using standard photolithography techniques. In a first step a transport channel oriented along the $[1\bar{1}0]$ direction is created. For that purpose a 100 µm wide and 1.5 mm long strip of photoresist is defined on the sample acting as an etching mask for the following process steps. The topmost Au and Fe layers besides the resist are removed by Ar ion etching; subsequently, the n-GaAs layer is etched away via wet chemical etching with peracetic acid (volume ratio: $CH_3COOH : H_2O_2 : H_2O = 5 : 1 : 5$), leaving a 2 µm high and 100 µm wide n-GaAs mesa channel on the semi-insulating substrate behind. After that spin injecting contacts on the channel and bond pads are defined in a second optical lithography step and evaporation of a 160 nm thick layer of Cr/Au. The evaporation is performed under an angle of 45° with respect to the sample plane to ensure a continuous metallization across the mesa edge and thus a proper electrical connection between the bond pads and the Schottky contacts on top of the transport channel. Afterwards, the Au, Fe and n^{++}-GaAs layers on the mesa channel in between the spin injecting contacts are removed by Ar ion milling and peracetic acid etching, in order to confine the electron transport solely to the n-GaAs channel. For this last etching step no resist is necessary to protect the spin injecting contacts, since the thick Au layer itself can be used as an etching mask. Finally, the sample is cleaved in the $[1\bar{1}0]$ direction along the transport channel, halving the channel width to 50 µm. Spin injection experiments are performed on a 20 µm wide Au/Fe contact (see Fig. 4.1 on the right hand side) at a temperature of 10 K.

4.1.2. Results and discussion

For electrical spin injection a rectangular bias voltage alternating between 0 and V_b is applied between the 20 µm wide contact and a reference contact at the end

of the mesa channel. The detection of the spin accumulation occurs via pMOKE measurements at the cleaved edge of the sample utilizing a lock-in technique. The Kerr rotation angle θ_K as a function of the magnetic field, which is applied along the [110] direction (= x-direction), is plotted in Fig. 4.2 on the left hand side for $V_b = 10\,V$. The measurement is performed with the laser spot being located on the n-GaAs channel, 1 µm underneath the spin injecting contact. Thin Fe films on GaAs(001) exhibit a strong uniaxial in-plane anisotropy with the easy axis oriented along the [110] crystallographic direction [107]. Thus, the rectangular switching behaviour of the pMOKE signal exactly reproduces the magnetization reversal of the Fe contact along its easy axis. This proves that the Kerr signal in the n-GaAs stems from electrical spin extraction from the Fe contact. In the following, to further eliminate any electro-optical contribution to the Kerr signal the difference of both remanent θ_K-values, $\Delta\theta_K$, is used as a measure for the spin polarization.

Figure 4.2 shows on the right hand side the photon energy dependence of the Kerr rotation, which was measured underneath the contact under spin injection conditions. The spectrum reflects the general shape as expected from theory (see Fig. 3.2) with a zero-crossing near the band gap energy of GaAs. However, compared to the calculations the spectrum is slightly shifted to lower energies. This shift can be explained with the smaller doping density that was used in the experiment, since a smaller electron density in the conduction band reduces the Fermi energy and thus smaller photon energies are sufficient to lift electrons into the conduction band (see Sec. 3.1.1). Furthermore, the higher temperature in the experiment smears out the Fermi level and thus leads to a smoothing of the theoretically expected curve, which results e.g. in the experimentally observed absence of the sign reversals near 1.55 eV in Fig. 3.2.

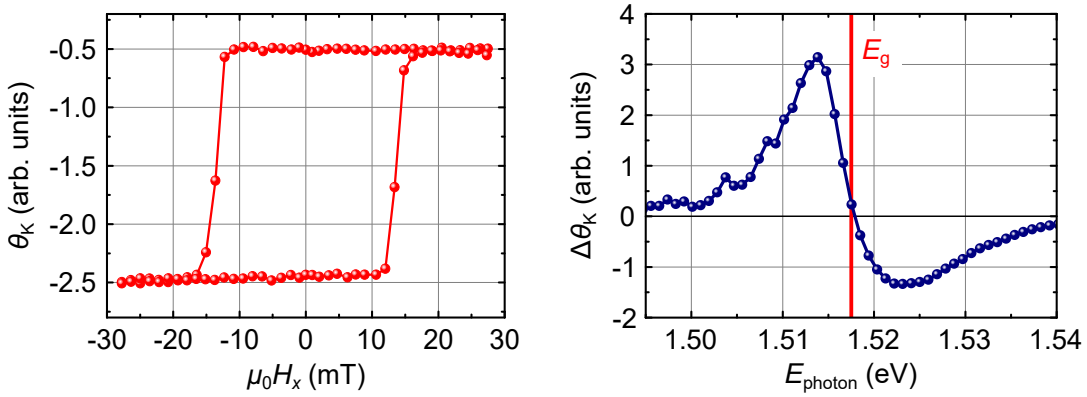

Figure 4.2.: Left: Hysteresis loop of the injected spin polarization in the n-GaAs channel for $V_b = 10\,V$. The loop reflects the magnetization curve of the Fe contact along [110]. Right: Kerr rotation spectrum in the n-GaAs channel underneath the spin injecting contact. The red line indicates the band gap of GaAs.

The fact, that the Kerr signal is only non-zero in the vicinity of the GaAs band gap, is a further proof that the experiment is exclusively sensitive to the spin imbalance in the GaAs conduction band. For the following measurements the photon energy is chosen slightly above the band gap near the extremum at $\sim 1.522\,\mathrm{eV}$. Here, the best signal-to-noise ratio is given. As has already been pointed out in Ref. [22], the lateral confinement of the n-GaAs to a $50\,\mu\mathrm{m}$ wide mesa channel requires the use of a relatively large photon energy. For photon energies below the band gap the penetration depth of the light becomes so large that the light can reach the rear edge of the transport channel and thus the back reflected light produces interference effects, that noticeably affect the signal quality.

Figure 4.3 illustrates linescans of the Kerr rotation angle along the n-GaAs channel for various positive bias voltages V_b. The latter is applied between the $20\,\mu\mathrm{m}$ wide contact located between $y = -10\,\mu\mathrm{m}$ and $+10\,\mu\mathrm{m}$ and a reference contact on the right hand side at a distance of $650\,\mu\mathrm{m}$. Thus, electrons flow from the right into the Fe contact and create a spin imbalance in the n-GaAs by majority spin extraction. The Kerr data directly map the spatial distribution of the spin density in the semiconductor channel. As expected the spin polarization is largest directly underneath the contact and decays exponentially outside the contact region. On the right hand side of the contact the spin density is affected by spin diffusion and spin drift. The electric field drives the spin imbalance to the left underneath the Fe contact. In particular, with increasing bias voltage, the maximum of the spin distribution moves slightly further to the left, as already observed earlier in Ref. [20]. On the left hand side of the contact no electric field is present and thus spin propagation is solely governed by spin diffusion. Therefore, the spin accumulation can spread much further outside the contact region than on the drift side. The decay of the Kerr rotation signal on this side can be well fitted by an exponential, yielding a spin diffusion length of $4\,\mu\mathrm{m}$.

The spin relaxation time in the n-GaAs can be obtained from Hanle measure-

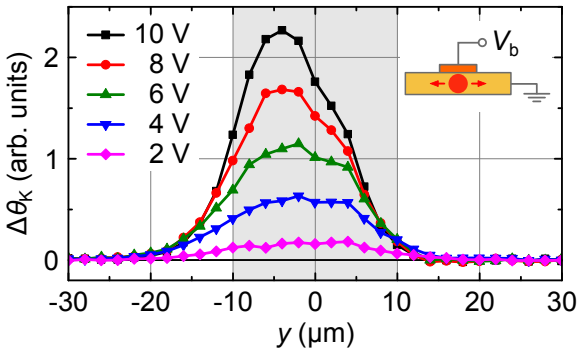

Figure 4.3.: Kerr rotation scans along the n-GaAs channel for electrical spin extraction under various applied bias voltages. The position of the injecting contact is indicated by the shaded region. The inset illustrates the current path within the sample.

ments, i.e. by a depolarization of the spin ensemble in a transverse magnetic field H_z. Fig. 4.4 shows such a measurement for a bias voltage of $V_\mathrm{b} = 4\,\mathrm{V}$, measured on the diffusion side of the contact. The Hanle curve has a symmetric shape, in accordance with the fact that the magnetic easy axis of the Fe contact is aligned parallel to the sensitive direction of the laser beam (cf. the rectangular switching behaviour of the contact in Fig. 4.2 on the left hand side). Fitting the data with the model introduced in Sec. 3.4.1 suggests a spin lifetime of about 9.5 ns. Note that Hanle data are frequently distorted by dynamic nuclear polarization (DNP) effects [53, 121]. These arise from hyperfine interaction of the spin-polarized conduction electrons with the GaAs nuclear spins. The nuclei are dynamically polarized by the injected electron spin polarization, creating a nuclear magnetic field, which in turn affects the electron spin precession. This leads to an artificial narrowing of the Hanle curves. However, since the nuclear spin relaxation time is of the order of a few minutes [122], DNP effects can be avoided by a fast periodic switching of the injector contact magnetization [123]. In the present experiment the magnetization of the contacts is reversed every $\sim 5\,\mathrm{s}$. Hence, DNP effects are eliminated in this work and the measured Hanle curves provide reliable values for the electron spin lifetime.

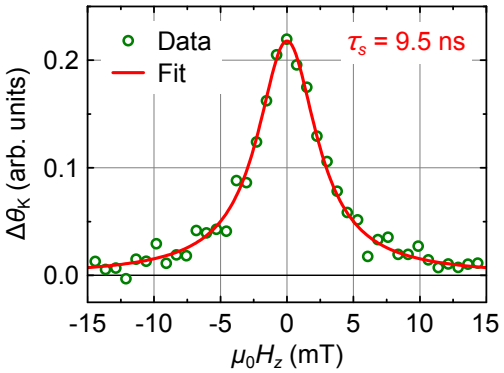

Figure 4.4: Hanle depolarization measurement in the n-GaAs channel for $V_\mathrm{b} = 4\,\mathrm{V}$. The fit yields a spin lifetime of about 9.5 ns.

To conclude the discussion on electrical spin injection into bulk GaAs, a comparison between electron and spin diffusion shall be given. The electron diffusivity D_e can be determined with the aid of Einstein's relation [43]

$$\frac{eD_\mathrm{e}}{\mu_\mathrm{e}} = \frac{n}{g(E_\mathrm{F})}, \tag{4.1}$$

where the electron mobility can be obtained from resistivity measurements of the n-GaAs channel. For the present sample one finds $\mu_\mathrm{e} = 4600\,\mathrm{cm}^2/\mathrm{Vs}$. The electron density is given by the doping density of the n-GaAs, thus $n = 4 \cdot 10^{16}\,\mathrm{cm}^{-3}$. Finally, the density of states at the Fermi level, $g(E_\mathrm{F})$, has to be determined. Since the GaAs conduction band can be described as an isotropic, parabolic band in the vicinity of the Γ-point, one can use the equations [26]

$$g(E_\mathrm{F}) = \frac{3n}{2E_\mathrm{F}} \qquad \text{and} \qquad E_\mathrm{F} = \frac{\hbar^2}{2m_\mathrm{e}^*}\left(3\pi^2 n\right)^{2/3}, \tag{4.2}$$

which are true for a three-dimensional electron gas with a spherical Fermi surface. Altogether, the electron diffusivity of the investigated sample is found to be $D_\mathrm{e} \approx 20\,\mathrm{cm}^2/\mathrm{s}$. The spin diffusivity D_s, on the other hand, can be obtained from the spin diffusion length λ_s and the spin lifetime τ_s via the expression $D_s = \lambda_s^2/\tau_s$, which results for the above measured values in $D_s \approx 17\,\mathrm{cm}^2/\mathrm{s}$. Thus, electron and spin diffusivities are of the same order of magnitude, as observed earlier by B. Endres on a similar bulk GaAs spin injection device [22]. This justifies the widely used assumption $D_s = D_\mathrm{e}$ for the case of electrical spin injection into bulk GaAs.

4.2. Electrical spin injection into a two-dimensional electron gas

The previous section has shown how a spin imbalance behaves in bulk GaAs. The findings for spin diffusion length and spin lifetime agree nicely with former spin injection experiments into n-GaAs. In particular, it was demonstrated that spin diffusion and electron diffusion have comparable strengths. All in all, electrical spin injection into bulk GaAs seems to be well understood by now and the standard drift-diffusion model of spin injection [41–43] provides in general the correct description. The situation changes, however, when one investigates spin injection into two-dimensional systems.

The demonstration of efficient electrical spin injection into a two-dimensional electron gas is a crucial step towards the development of future spintronic devices like the spin field-effect transistor as proposed by Datta and Das [16]. Spin injection into 2DEGs has by now been reported by several groups [124–127]; however, it turns out that ballistic transport effects need to be taken into account to fully understand the experimental data [124,125,127,128]. This means that the standard drift-diffusion model of spin injection [41–43] that is commonly used to interpret bulk spin injection experiments cannot be used adequately which in turn makes the interpretation of spin injection data into 2DEGs difficult. Only little data is available concerning electrical spin injection into 2DEGs; furthermore, the injected spins are detected exclusively using electrical techniques.

Here, a combination of electrical and magneto-optical detection is used to investigate electrical spin injection from ferromagnetic (Ga,Mn)As contacts into a 2DEG formed at an (Al,Ga)As/GaAs interface. The experiments are performed on a heterostructure system that was developed and first studied by Oltscher *et al.* in 2014 [127]. The topic of this section has been published in Physical Review B **95**, 035304 (2017). Therefore, parts of this section have been directly taken from Ref. [129].

4.2.1. Samples

The layout of the investigated wafers is sketched in the middle part of Fig. 4.5. The semiconductor layers are grown by molecular beam epitaxy (MBE) on a semi-insulating GaAs(001) substrate. The layer sequence starts with a 1000 nm thick GaAs/(Al,Ga)As superlattice (not shown), followed by 75 nm $(Al_{0.33}Ga_{0.67})As$, a Si δ-doping layer, 50 nm $(Al_{0.33}Ga_{0.67})As$, 50 nm i-GaAs, 100 nm n-GaAs ($N_D \approx 7 \cdot 10^{16}\,cm^{-3}$), a 15 nm thick n $\rightarrow$ n^{++} transition layer and 8 nm n^{++}-GaAs with $N_D \approx 5 \cdot 10^{18}\,cm^{-3}$. The top layer of 50 nm $(Ga_{0.95}Mn_{0.05})As$ is grown using low-temperature MBE. Additionally, a layer of 2.2 nm $(Al_{0.33}Ga_{0.67})As$ was grown in between the n^{++}-GaAs and the (Ga,Mn)As layers to prevent diffusion of Mn atoms into the underlying n-GaAs layers. The p-type (Ga,Mn)As and the n-GaAs layers form an Esaki diode structure, enabling tunneling of spin-polarized carriers between (Ga,Mn)As and GaAs. The 2DEG is confined at the GaAs/(Al,Ga)As interface as depicted by the red layer in Fig. 4.5.

Figure 4.5 shows on the left hand side simulations of the band-profile and the electron density for the full layer stack. In addition to the 2DEG at the GaAs/(Al,Ga)As interface there is a bulk electron distribution in the highly doped GaAs layers above. This region with bulk carriers is necessary to ensure an efficient charge transport between the (Ga,Mn)As and the 2DEG [127].

The spin injection devices have been prepared by M. Oltscher and T. Kuczmik from the chair of Prof. Dr. D. Weiss. Details on the sample fabrication can be found in Refs. [130, 131]. The general sample design is sketched in Fig. 4.6. A

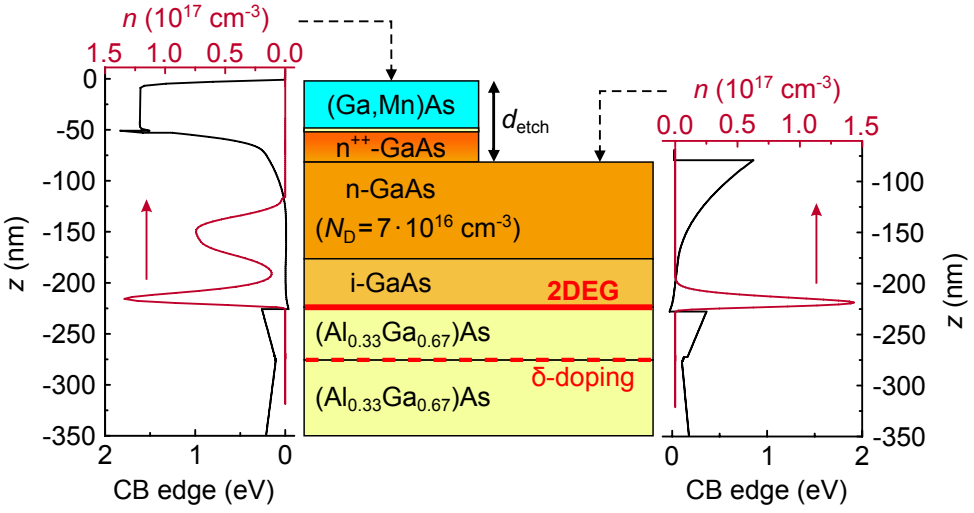

Figure 4.5.: Layer stack of the investigated devices. The diagrams on the left and right hand side show calculations for the conduction band (CB) edge (black) and the electron density (red) at $T = 4.2\,K$ for the full layer stack and with the topmost layers removed, respectively (adapted from [127]).

chemical wet etching technique is used to confine the electron transport to a 50 µm wide and 750 µm long channel oriented along the [110] direction. Contacts are defined by standard optical and electron-beam lithography techniques and evaporation of Ti/Au pads. In contrast to the bulk spin injection sample from the previous section, these samples have several narrow spin injecting contacts with varying widths between 0.5 µm and 4 µm located close to each other on the transport channel. Two 150 µm × 150 µm large contacts at the ends of the channel are used as references. In a last etching step the (Ga,Mn)As and n^{++}-GaAs layers in between the contacts are removed to limit the electron transport between the contacts exclusively to the 2DEG. The etching depth d_{etch} is a critical parameter to obtain a good 2DEG. It is chosen deep enough to ensure a complete depletion of the bulk carrier density above the 2DEG, in order to avoid transport parallel to the 2DEG. In many cases the 2DEG itself is also depleted or has only a small carrier density after this etching process. However, it can be re-populated by carefully illuminating the sample, which transfers carriers from the δ-doping layer to the GaAs/(Al,Ga)As interface, as discussed in Sec. 2.1.2. Fig. 4.5 shows on the right hand side the simulated electron density in the heterostructure with the (Ga,Mn)As and the n^{++}-GaAs being etched away. In this case the bulk electrons are fully depleted and the 2DEG is the only remaining electronic system [127].

Finally, the sample is cleaved in [110] direction along the transport channel, reducing the channel width to about 30 to 40 µm. This exposes the $(1\bar{1}0)$ surface, which enables direct magneto-optical access to the spin accumulation underneath the injecting contacts. Additionally to the pMOKE measurements at the cleaved edge the sample design allows an electrical detection of the spin accumulation by measuring the nonlocal voltage V_{nl} while injecting spins at a neighbouring contact

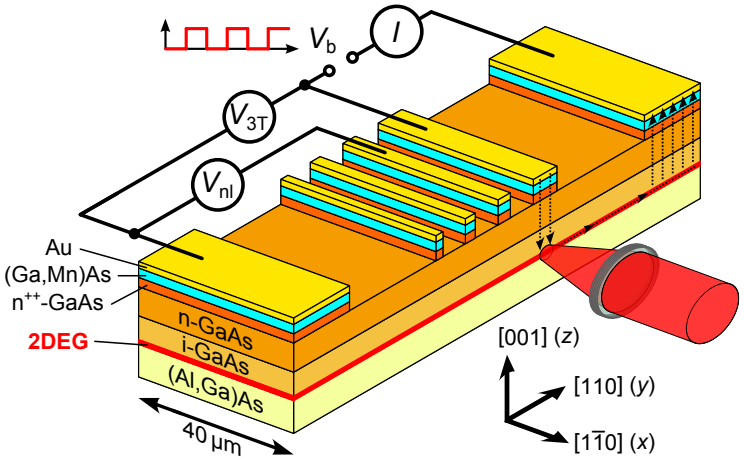

Figure 4.6.: Sample layout and measurement techniques. Apart from optical measurements at the cleaved edge the experiment allows electrical spin detection by using a nonlocal measurement geometry.

(see Fig. 4.6). Fig. 4.7 shows a light microscope image of one of the investigated samples, illustrating the narrow spin injecting contacts in the center part of the 2DEG channel.

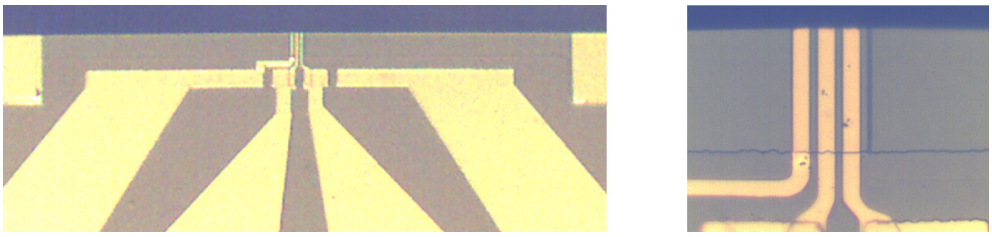

Figure 4.7.: Left: Micrograph of a cleaved sample for spin injection into a two-dimensional electron gas. Right: Zoom onto the center part of the sample illustrating three 4 µm wide contacts on the 30 µm wide 2DEG channel.

4.2.2. Electrical and optical properties

Experiments are performed on samples from four different wafers, which will be labeled with the letters A to D in the following. The electrical properties of the wafers were characterized by M. Oltscher and T. Kuczmik utilizing magnetotransport experiments. In all cases the formation of a high-quality 2DEG could be observed, albeit sometimes the samples had to be illuminated to populate the 2DEG with carriers. Fig. 4.8 shows on the left hand side magnetotransport measurements of a sample from wafer B. In this case it was not necessary to illuminate the sample to populate the 2DEG. The data reveal clear quantum Hall plateaus and pronounced Shubnikov-de Haas oscillations, both being characteristic features of truely two-dimensional transport without any bulk carrier conductance parallel to the 2DEG. From the magnetotransport data the electron sheet density n_s and the mobility μ_e can be extracted, which are summarized in Tab. 4.1 together with other important properties for all four investigated wafers. In all cases the 2DEGs have high mobilities of the order of several $10^5\,\mathrm{cm}^2/\mathrm{Vs}$, which exceeds the mobility of bulk GaAs samples by two orders of magnitude.

For the pMOKE measurements at the cleaved edge the samples have to be illuminated with a linearly polarized probe laser beam. Thus, the important question arises, how the system is affected by the laser illumination. In contrast to magneto-optical measurements on bulk GaAs samples, where illumination was shown to have a negligible effect on the electron distribution [18, 22], laser illumination may disturb the electronic system of the present heterostructures in two ways. First, it continuously creates electron-hole pairs within the GaAs-layers above the 2DEG, which increases the carrier densities within the 2DEG channel and the n-doped GaAs region underneath the spin injecting contacts. However, a simple estimation shows, that for wavelengths $\geq 820\,\mathrm{nm}$ this optically created,

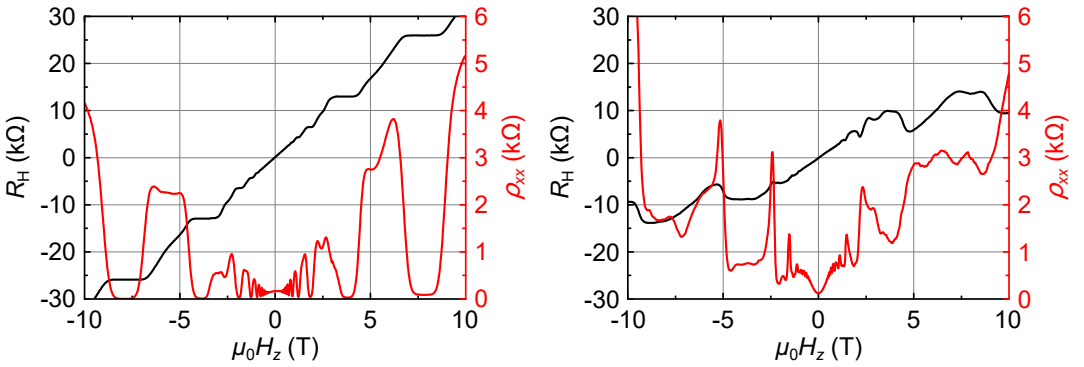

Figure 4.8.: Left: Magnetotransport measurement of a sample from wafer B at $T = 1.4\,\mathrm{K}$. The data show the quantum Hall effect (black) and the Shubnikov-de Haas oscillations (red). The sample was not illuminated for this measurement (data taken from [132]). Right: After illumination the data become distorted, which indicates the presence of a parallel conduction channel (data taken from [132]).

additional electron density lies well below the electron density of the 2DEG and therefore this effect should have a negligible influence on the electron distribution of the system. Considering a recombination lifetime in n-GaAs of about 1 ns [116–118], in equilibrium between electron-hole pair generation and relaxation, one can roughly estimate the additionally generated electron density in the conduction band for the used laser power of 10 µW to be of the order of $\sim 10^{14}\,\mathrm{cm}^{-3}$ to $\sim 10^{15}\,\mathrm{cm}^{-3}$, which is well below the metal-to-insulator transition of GaAs (see Sec. 3.3). So, optical generation of carriers in the n-GaAs above the 2D channel will not play an important role next to the contacts, where the bulk electrons have been depleted by chemical etching; bulk carriers will only be present directly underneath the spin injecting contacts.

The second effect, which plays a more severe role for the present system, is the persistent photoconductivity effect [29–34] (see Sec. 2.1.2). Persistent photo-

Table 4.1.: Characteristic properties of the investigated 2DEGs. The electron density n_s, electron mobility μ_e, electron mean free path $l_\mathrm{e,mf}$, electron diffusivity D_e, Fermi energy E_F, Fermi temperature T_F and electron momentum relaxation time τ_p have been extracted from magnetotransport measurements at $T = 1.6\,\mathrm{K}$.

wafer	n_s cm^{-2}	μ_e $\frac{\mathrm{cm}^2}{\mathrm{Vs}}$	$l_\mathrm{e,mf}$ µm	D_e $\frac{\mathrm{cm}^2}{\mathrm{s}}$	E_F meV	T_F K	τ_p ps
A	$2.3 \cdot 10^{11}$	$5.0 \cdot 10^5$	4.0	4200	8.2	95	19
B	$1.8 \cdot 10^{11}$	$2.1 \cdot 10^5$	1.5	1300	6.3	73	8.0
C	$2.5 \cdot 10^{11}$	$3.2 \cdot 10^5$	2.6	2900	9.0	105	12
D	$2.2 \cdot 10^{11}$	$3.3 \cdot 10^5$	2.5	2500	7.9	91	12

conductivity has its origin in the photoexcitation of deep impurity levels (DX centers) in the (Al,Ga)As layer. Photon absorption excites electrons into the (Al,Ga)As conduction band and hence leads to an increased conductivity, which persists even after switching off the light source since the electrons cannot return to the traps at low temperatures due to a repulsive energy barrier. Therefore, laser illumination of the sample creates an additional, parasitic transport channel in the δ-doping region of the (Al,Ga)As. This parallel channel becomes visible in the magnetotransport measurements, as can be seen in Fig. 4.8 on the right hand side. In contrast to the case without illumination the Shubnikov-de Haas-oscillations do not reach zero any more and the Hall resistance is distorted as well. However, the data show that the parallel channel in the (Al,Ga)As does not destroy the 2DEG at the GaAs/(Al,Ga)As interface, as the illuminated sample still exhibits clear Shubnikov-de Haas-oscillations. In particular, the electronic properties of the 2DEG (like the mobility or the electron mean free path) do not change significantly under illumination. Thus, one can conclude, that transport in the illuminated sample can be described as parallel transport in the 2DEG and the (Al,Ga)As channel, as reported earlier in Refs. [35, 36]. However, transport should still be dominated by the 2DEG due to its high mobility of several $10^5\,\mathrm{cm}^2/\mathrm{Vs}$.

Figure 4.9 shows the I-V-characteristic of one of the spin injecting contacts. The kink in forward direction at $V_{3\mathrm{T}} \approx 0.45\,\mathrm{V}$ is a typical feature of Esaki diodes and confirms proper Esaki tunneling, which is a necessary prerequisite for electrical spin injection from the (Ga,Mn)As into the GaAs-based 2DEG. Since the I-V-characteristics of the contacts are found to be unchanged under illumination, one can conclude that the process of spin injection itself is unaffected by laser illumination.

In order to characterize the optical properties of the heterostructure, microphotoluminescence (μ-PL) measurements are performed at the cleaved edge of the sample. The μ-PL spectrum of the transport channel clearly reveals three optically active regions in the sample (see Fig. 4.10 on the left): On the one hand one observes the GaAs and the (Al,Ga)As layers with recombination peaks in

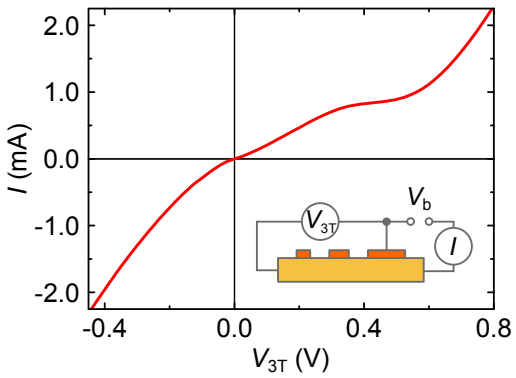

Figure 4.9: Typical I-V-characteristic of an Esaki tunnel barrier contact (contact area: $2\,\mu\mathrm{m} \times 40\,\mu\mathrm{m}$). The inset illustrates the measurement geometry.

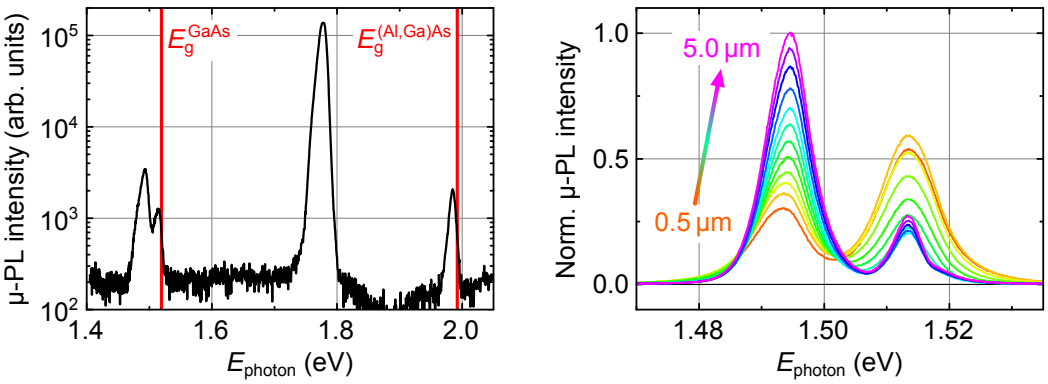

Figure 4.10.: Left: Microphotoluminescence measurement of the topmost layers of the heterostructure. The measurement is performed at the cleaved edge of a sample from wafer A. Right: μ-PL in the vicinity of the GaAs band gap with the distance of the exciting laser spot to the surface of the layer stack ranging from 0.5 μm to 5.0 μm.

the vicinity of the corresponding band gaps. On the other hand there is a strong peak at $E_{\text{photon}} \approx 1.78\,\text{eV}$, which stems from the superlattice grown between the substrate and the (Al,Ga)As. The latter does not contribute to charge (and hence to spin) transport and thus does not play a role for the electrical and magneto-optical investigations of the spin accumulation in the system. The luminescence peak at $E_{\text{photon}} \approx 1.98\,\text{eV}$ mainly originates from transitions in the δ-doping area of the (Al,Ga)As and therefore represents the parallel, parasitic transport channel. The μ-PL feature at the GaAs band gap consists of two single peaks. Here, the lower-energy peak is the well-known carbon band in GaAs [133, 134]. This peak mainly stems from carbon impurities in the GaAs substrate as it is significantly weaker in the topmost, MBE-grown layers compared to the GaAs substrate (see Fig. 4.10 on the right hand side). The higher-energy peak at the GaAs band gap is in part due to excitons which are bound to Si-donors in the GaAs, but it also stems from optical transitions between the 2DEG and the valence band.

With the magneto-optical spin detection approach it should be easy to distinguish the spin accumulation in the 2DEG from a possible spin signal in the parallel transport channel within the (Al,Ga)As layer by simply tuning the laser to the GaAs band gap. Fig. 4.11 displays a Kerr rotation spectrum measured at the cleaved edge in the transport channel underneath a narrow contact under spin extraction conditions. The Kerr signal is only nonzero in the vicinity of the GaAs band gap and therefore it can be clearly attributed to the spin polarization in the GaAs-based 2DEG. A possible spin accumulation in the (Al,Ga)As-based parallel transport channel does not contribute to the Kerr rotation at these photon energies as the corresponding band gap is much larger and would only create a significant Kerr rotation near $E_{\text{photon}} \approx 1.98\,\text{eV}$. Therefore, in the case of Fig. 4.11, a photon energy of 1.503 eV is chosen for the Kerr measurements of the spin polarization. Here, on the one hand the influence of the laser on the

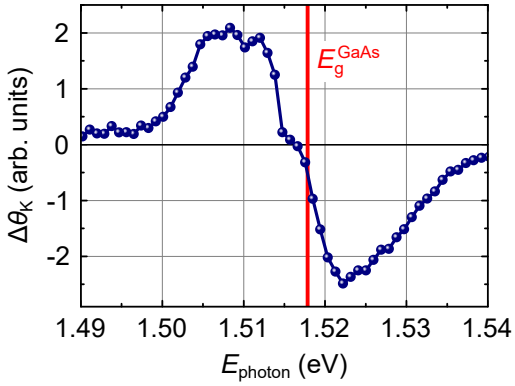

Figure 4.11: Kerr rotation spectrum in the transport channel measured under spin extraction conditions.

electronic system in the GaAs is reduced to a minimum as the photon energy lies below the band gap and on the other hand one can rule out any Kerr signal originating from the parasitic transport channel underneath the 2DEG.

Note that the height of the transport channel of the 2DEG samples is only about 300 nm [130, 131]. Thus, interference effects due to back-reflections of the laser light from the rear edge of the transport channel, as commonly observed in pMOKE experiments on bulk GaAs samples with a micrometer high mesa channel, are not such a severe problem here. Therefore, in contrast to the bulk spin injection experiments, where the photon energy had to be chosen above the band gap to obtain a good signal-to-noise ratio, here it is also possible to choose the photon energy below the band gap of GaAs.

4.2.3. Spin density distribution

Spin injection into the two-dimensional electron gas is carried out in an analogous way to the spin injection experiments into bulk GaAs, i.e. by applying a square-wave bias voltage alternating between zero and V_b between a spin injecting contact and a reference contact on the end of the 2DEG channel and employing lock-in detection. Fig. 4.12 shows on the left the Kerr rotation angle θ_K as a function of the magnetic field H_x for $V_b = 1\,V$, detected on the cleaved edge underneath a (Ga,Mn)As contact. The measurement reproduces the (Ga,Mn)As hysteresis loop along the x-direction, which demonstrates electrical spin extraction from the semiconductor heterostructure into the ferromagnetic (Ga,Mn)As. Note that the magnetic easy axes of (Ga,Mn)As are along the in-plane $\langle 100 \rangle$ directions [108, 109]. Thus, magnetization reversal along the x-direction proceeds by magnetization rotation and an irreversible jump due to the formation of 90° domains (see Fig. 4.12 on the right hand side and Ref. [109]). Due to the tilted easy axes of the (Ga,Mn)As contacts with respect to the sensitive direction of the laser beam, the Kerr signals in remanence are slightly reduced with respect to the values at saturation. However, the height of the hysteresis loop in remanence is

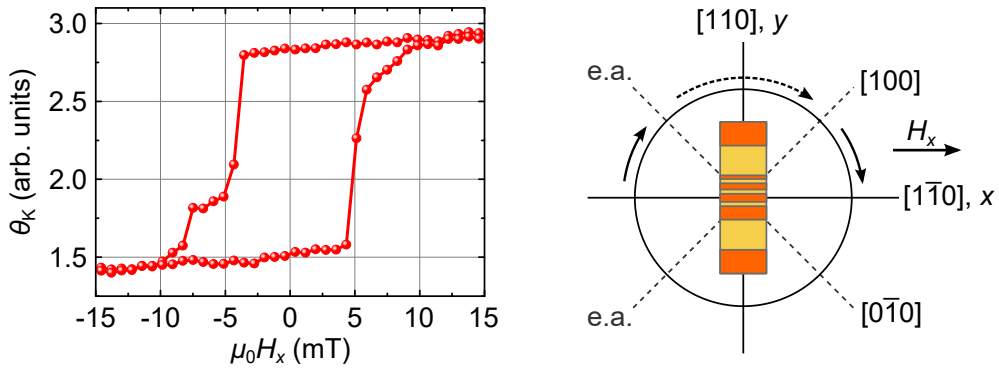

Figure 4.12.: Left: Hysteresis loop of the spin accumulation measured underneath a (Ga,Mn)As contact while extracting spins at $V_\mathrm{b} = 1\,\mathrm{V}$. The loop reflects the magnetization reversal of the (Ga,Mn)As contact. Right: Magnetization reversal process in (Ga,Mn)As along the x-direction. The magnetic easy axes are along the in-plane $\langle 100 \rangle$ directions. Starting from a saturated state along $-x$ the magnetization reversal takes place via a rotation to [010], a jump to [100] and a final rotation to [1$\bar{1}$0].

still proportional to the spin density in the heterostructure (cf. Ref. [22]). Thus, Kerr measurements are performed in remanence after saturating the sample along [1$\bar{1}$0] and [$\bar{1}$10], respectively, and taking the difference $\Delta\theta_\mathrm{K}$, just like in the case of spin injection into bulk GaAs.

One of the major challenges in detecting a 2D spin accumulation with pMOKE at the cleaved edge arises from the fact that the electron distribution is confined to less than 100 nm along the growth direction of the wafer (cf. Fig. 4.5). The probe laser with a photon energy in the vicinity of the GaAs band gap (corresponding wavelength $\approx 817\,\mathrm{nm}$), on the other hand, can be focused to a minimal spot size of roughly 700 nm (see Sec. 3.3). Thus, less than 10% of the laser light actually experience a Kerr rotation. This is shown in Fig. 4.13, where the laser is scanned along the growth direction of the heterostructure over the sample edge, while extracting spins at a positive bias voltage. The measurement is performed at the position of a spin injecting contact[1]. The Kerr signal has a Gaussian shape with a FWHM of 720 nm. This shape arises from the convolution of the laser spot profile (FWHM $\approx 700\,\mathrm{nm}$) with the distribution of the spin accumulation along the z-direction. Since the spin distribution is much narrower than the laser spot diameter, the measurement essentially reflects the laser spot profile. This underlines the importance of a well focused laser for these measurements. In particular, the laser spot has to be carefully aligned with respect to the 2DEG plane, as a small misalignment of only a few hundred nanometers already drastically reduces the Kerr signal originating from the 2D spin polarization.

[1]Note that the maximum of the Kerr signal in Fig. 4.13 is deeper under the sample surface than expected from the position of the electron density in Fig. 4.5, due to the presence of a thick Ti/Au layer on top of the (Ga,Mn)As.

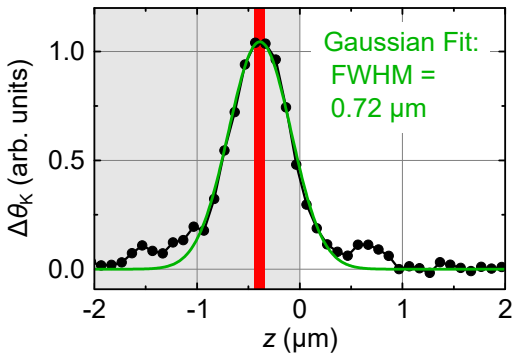

Figure 4.13: Linescan of the Kerr rotation signal while scanning the laser spot in z-direction over the sample edge (at $z = 0$). The red stripe indicates roughly the calculated width of the electron density in the sample (cf. Fig. 4.5). A Gaussian fit yields an apparent width of the spin profile of about (0.72 ± 0.02) µm.

Figure 4.14 illustrates linescans of the Kerr rotation along the 2DEG channel for $V_\mathrm{b} = \pm 0.75$ V in a sample from wafer B, representing the spatial spin distribution within the 2DEG. The bias voltage is applied between the 2 µm wide contact at $y = 0$ and the large reference contact on the right-hand side. For positive voltages electrons flow from the right into the contact at $y = 0$, creating a spin accumulation within the 2DEG by majority spin extraction; for negative voltages electrons flow from the contact to the right, injecting majority spins at the contact position. In both cases the spin polarization exhibits a sharp peak right at the position of the injector contact. The decay of the Kerr rotation signal on the left-hand side can be well fitted by an exponential in both cases, yielding spin decay lengths in the field-free region of $\lambda_s = (2.0 \pm 0.2)$ µm and $\lambda_s = (1.8 \pm 0.2)$ µm, respectively. On the right-hand side of the contacts one has to consider a superposition of spin diffusion and drift. Therefore, the decay length is reduced (enhanced) for spin extraction (injection), which is clearly visible in the measurements.

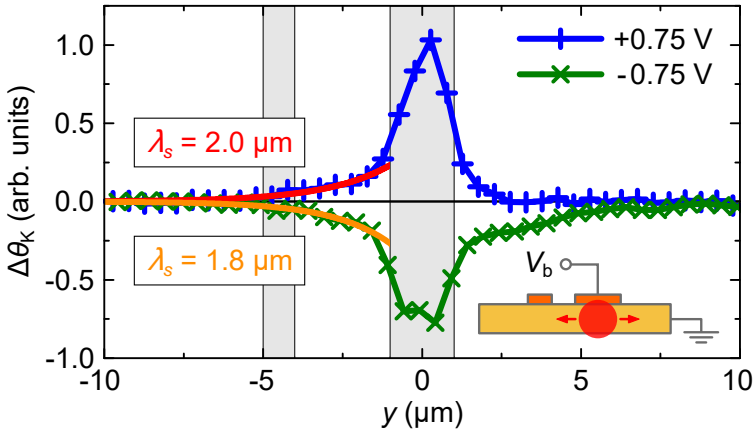

Figure 4.14.: Kerr rotation scans along the 2DEG channel for spin injection ($V_\mathrm{b} = -0.75$ V) and spin extraction ($V_\mathrm{b} = +0.75$ V) in sample B. The bias voltage is applied between the 2 µm wide contact at $y = 0$ and the reference contact on the right-hand side. The contacts are indicated by shaded regions. The red and orange lines represent exponential fits to the data in the field-free region with the corresponding values of the spin decay lengths λ_s. The inset illustrates the current path within the sample.

The spin decay lengths λ_s measured on other samples are altogether found to lie in a range from 2 µm to 7 µm. Thus, the magneto-optically determined decay lengths are in quite fair agreement with the nonlocal measurements of Kuczmik *et al.*, where decay lengths between 2 µm and 12 µm were reported [135].

4.2.4. Signal enhancement due to ballistic tunneling

The bias dependence of the spin polarization in the heterostructure is shown in Fig. 4.15 on the left for two different, 4 µm wide injector contacts of a sample from wafer A. In both cases the Kerr signals are measured in the transport channel directly underneath the contacts. The curves exhibit an almost perfectly antisymmetric shape with the expected sign reversal when passing from spin injection to spin extraction. However, in contrast to contact 2, contact 1 exhibits a clear non-linearity for small bias voltages. The discrepancy between the two contacts becomes even more pronounced when normalizing the data with respect to the current I flowing in the device and when plotting the normalized data vs. the three-terminal voltage V_{3T}, which is shown in Fig. 4.15 on the right hand side. Here, contact 2 exhibits a maximum signal at $V_{3T} = 0$ which monotonically decreases with increasing $|V_{3T}|$, whereas contact 1 has two maxima at $V_{3T} \approx \pm 0.6$ V and a minimum signal at $V_{3T} = 0$.

The nonmonotonic behaviour of contact 1 strikingly resembles the bias dependence which has been reported by Oltscher *et al.* on similar samples [127], where it was detected electrically in a nonlocal geometry (see Fig. 4.16). There, the peaks at $V_{3T} \approx \pm 0.6$ V have been linked to a signal enhancement which occurs due to direct, ballistic tunneling of spin-polarized carriers from (Ga,Mn)As to the 2DEG or vice versa. This is sketched in Fig. 4.17. For small voltages electrons

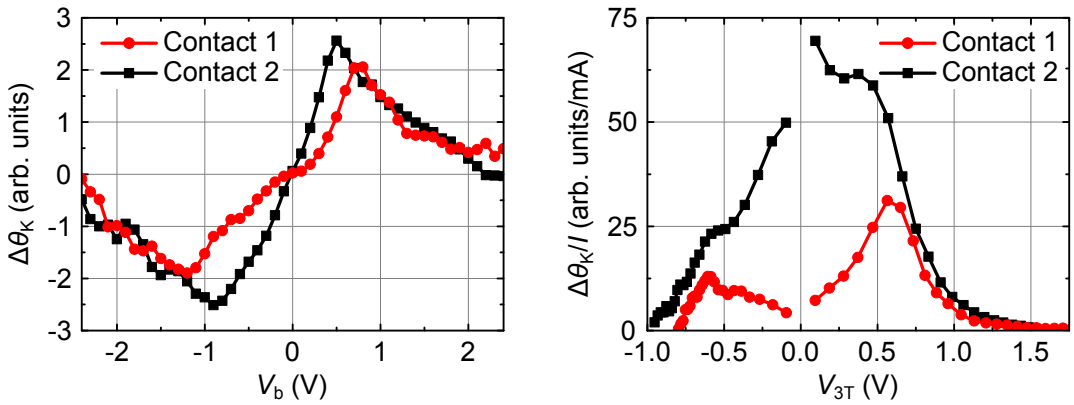

Figure 4.15.: Left: Bias dependence of the Kerr rotation signal $\Delta\theta_K$ for two different contacts of a sample from wafer A. Right: Kerr rotation normalized to the current I plotted vs. V_{3T} for the same two contacts.

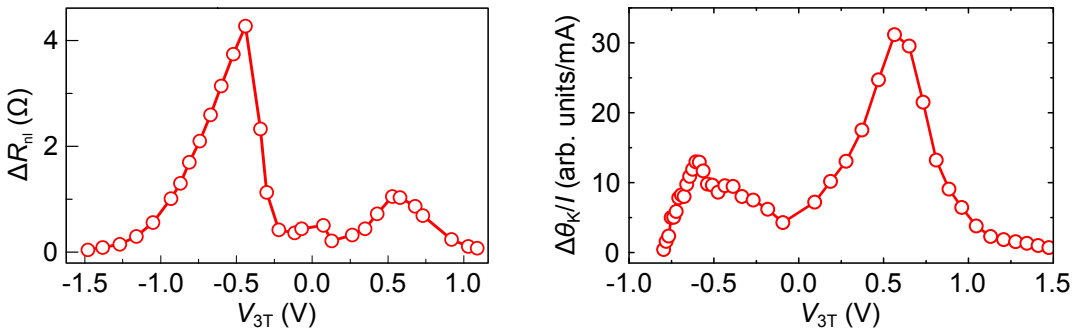

Figure 4.16.: Left: Bias dependence of the nonlocal resistance $\Delta R_{\mathrm{nl}} = \Delta V_{\mathrm{nl}}/I$. The positive- and negative-bias peak correspond to a spin injection efficiency of ∼150% and ∼650% (adapted from [127]). Right: The same data as in Fig. 4.15 on the right hand side for contact 1. Apart from the peak amplitude ratio the data reproduce the nonmonotonic behaviour of the nonlocal measurements.

travel via the bulk electronic states in the n-GaAs layer between the (Ga,Mn)As and the 2DEG. In this case it is expected that a spin accumulation is generated in the n-GaAs underneath the injector contact. For larger bias voltages, however, electrons can tunnel directly from the (Ga,Mn)As to the 2DEG or vice versa, i.e. without involving 3D states. Analyzing the nonlocal data near $V_{3\mathrm{T}} \approx \pm 0.6\,\mathrm{V}$ with the standard drift-diffusion model of spin injection [41–43] resulted in highly unphysical spin injection efficiencies exceeding 100% [127]. Oltscher *et al.* attributed this discrepancy to the standard model to be caused by the ballistic motion of the electrons underneath the injector contact [127]. Recently, a signal enhancement in a truly 2D geometry has been explained theoretically by introducing a ballistic contribution to the spin chemical potential and solving the corresponding spin ballistic-diffusion equations [128]. It has been argued that for optically injected spin polarizations such an enhancement should not

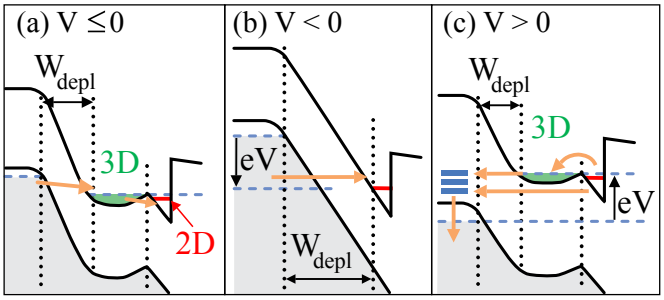

Figure 4.17.: Possible transport paths between the (Ga,Mn)As and the 2DEG. (a) At small voltages transport includes the bulk states in the n-GaAs. (b) At large negative bias electrons tunnel directly from the (Ga,Mn)As into the 2DEG. (c) At large positive bias tunneling takes place with and without bulk electron states involved (taken from [127]).

be observable due to the absence of ballistic tunneling during optical orientation. Therefore, the experimentally observed nonmonotonic bias dependence of the spin polarization is a clear signature that the magneto-optical approach is sensitive to the electrical spin injection into the 2DEG.

Contact 2 shows a different bias dependence with a maximum at $V_{3\mathrm{T}} = 0$ (see Fig. 4.15 on the right hand side). The origin of this maximum is most probably the contribution of bulk-like electronic states in the highly n-doped GaAs layers right underneath the injector contact, which increase the total Kerr rotation. The spin accumulation μ_s in the nonmagnetic material is proportional to its resistivity (cf. Eq. 2.4), i.e. in the case of the electronic states within the bulk n-GaAs one has $\mu_s \propto \rho_{\mathrm{N}}$ with the resistivity ρ_{N} of the n-GaAs, whereas for the 2D channel $\mu_s \propto R_s$ applies, with R_s being the sheet resistance of the 2DEG. Hence, due to the large resistance of n-GaAs with respect to the high mobility 2DEG, a sizable spin accumulation can build up in the highly n-doped GaAs layers underneath the contacts. For spin injection into (Ga,Mn)As/GaAs-based bulk systems it has been shown both theoretically [67] and experimentally [68] that the spin injection efficiency is largest for zero bias. This is a robust feature of electrical spin injection experiments into bulk GaAs and has also been measured for FeCo/GaAs Schottky contact injectors [17]. Thus, the maximum signal of contact 2 at zero bias can be attributed to the spin accumulation in the n-GaAs region above the 2DEG. However, the kinks in the bias dependence of contact 2 at $V_{3\mathrm{T}} \approx -0.5\,\mathrm{V}$ and $V_{3\mathrm{T}} \approx +0.3\,\mathrm{V}$ and the fact that the data for both contacts merge for voltages $|V_{3\mathrm{T}}| > 0.6\,\mathrm{V}$, show that the bias dependence of contact 2 still contains the contributions from the pure 2D spin polarization. Note that these subtle differences in the bias dependence of different (but nominally same) contacts can be detected in magneto-optical experiments, but are difficult to extract from all-electrical measurements.

All in all, these measurements show that the magneto-optical detection method is sensitive to the 2D spin accumulation. However, as shown by the signal below contact 2, directly underneath the spin injecting contacts the bulk-like electronic states within the highly n-doped GaAs layers might become visible as an additional contribution to the optically detected spin signal. Note that this bulk carrier distribution is only present directly underneath the injector contacts; in between the contacts it has been completely removed by wet-chemical etching. Hence, Kerr rotation signals, which are detected next to the contacts, stem solely from the 2D spin accumulation.

As a final remark it should be noted that the nonmonotonic bias dependence of the spin polarization signal could only be observed on samples from wafer A, which is true for both the pMOKE and the all-electrical spin valve experiments [136]. Wafer A has a slightly different doping profile compared to the other wafers, which manifests e.g. in a roughly one order of magnitude larger resistance of

the Esaki barrier. This suggests that the discussed signal enhancement strongly depends on the properties of the investigated 2DEG as well as on the properties of the tunnel barrier. However, apart from this effect all investigated wafers show a similar behaviour concerning the spatial spin distribution or the spin dynamics. The latter of the two will be addressed in the following.

4.2.5. Hanle measurements

The dynamical aspects of the 2D spin injection are investigated by performing Hanle depolarization measurements, which provide values for the electron spin lifetime τ_s and the spin diffusivity D_s. Fig. 4.18 displays on the left hand side a Hanle depolarization curve of a sample from wafer A, measured on the diffusion side 1 µm away from the injecting contact to rule out any influence of the injector contacts on the spin polarization. Although the large electron mean free path of a few micrometers (cf. Tab. 4.1) suggests that the system has to be considered to be in a crossover regime between ballistic and diffusive transport, the data can be well modeled using the standard drift-diffusion theory of spin injection. A fit of the data yields a spin lifetime of $\tau_s = (1.5 \pm 0.1)$ ns. Fig. 4.18 on the right shows a Hanle curve from a sample from wafer B. For this measurement the distance between injector and the laser spot is chosen to be 3 µm. Again, the fit yields a spin lifetime of the order of 1 ns.

The spin lifetime τ_s extracted from the Hanle curves is given by the geometric mean of the spin lifetimes along the two principal axes [110] and $[1\bar{1}0]$ (see Sec. 3.4.2):

$$\tau_s = \sqrt{\tau_{s,[110]}\tau_{s,[1\bar{1}0]}}. \tag{4.3}$$

For GaAs-based two-dimensional electron systems the relaxation time for electron spins oriented along the [110] direction was shown to be of the order of several

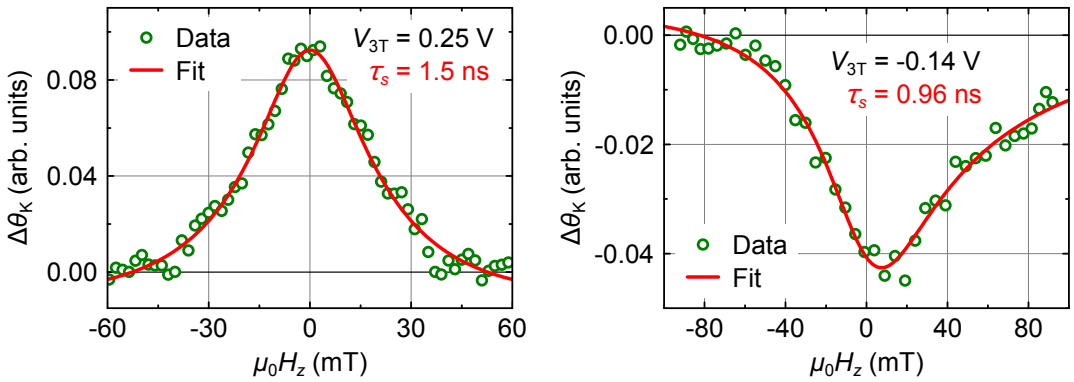

Figure 4.18.: Hanle depolarization curves of samples from wafer A (left) and wafer B (right). The fits yield spin lifetimes of (1.5 ± 0.1) ns and (0.96 ± 0.09) ns, respectively.

nanoseconds, whereas $\tau_{s,[1\bar{1}0]}$ is typically in the range of a few 100 ps [87, 90, 91]. Thus, the averaged in-plane spin lifetime τ_s of the order of 1 ns measured for the present samples, is fully consistent with these lifetime reports. Note, however, that the present experiment does not allow to extract individual values for $\tau_{s,[110]}$ and $\tau_{s,[1\bar{1}0]}$. Hence, the magnitude of the spin dephasing anisotropy remains an unknown quantity.

To rule out that the spin accumulation is affected by optically generated charge carriers, additionally all-electrical nonlocal voltage measurements are performed without laser illumination on the cleaved edge. In these measurements neither are there optically generated electron-hole pairs in the n-GaAs, nor are the (Al,Ga)As DX centers excited. The electrical measurements are carried out using a second ferromagnetic contact to probe the spin imbalance in the 2DEG (see Fig. 4.6). The injected spin accumulation spreads from the injector to the nearby detector contact, where it generates a nonlocal voltage signal V_{nl} via spin-charge coupling [9]. Fig. 4.19 shows on the left hand side the magnetic field dependence of V_{nl} using a 2 µm wide contact as injector and the neighbouring 1 µm wide contact as detector (injector-detector distance 3 µm). The value of the nonlocal voltage depends on the relative orientation of the magnetizations of injector and detector contact, as it is proportional to the projection of the injected spin polarization direction onto the magnetization direction of the detector contact [9]. In the present case the two contacts have very similar coercive forces; furthermore, the magnetization reversals proceed by a gradual rotation of the magnetization within a quite broad field range of about 10 mT (see Fig. 4.19 on the right hand side), which happens due to the tilted easy axes of the (Ga,Mn)As contacts with respect to the applied magnetic field direction. Hence, the nonlocal voltage mea-

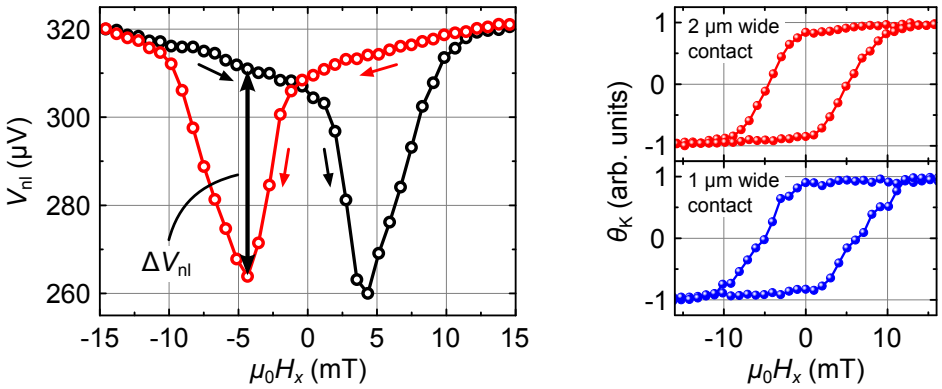

Figure 4.19.: Left: Nonlocal voltage V_{nl} as a function of the applied magnetic field H_x while extracting spins at $V_{\mathrm{b}} = +0.75$ V from a 2 µm wide contact and using the neighbouring 1 µm wide contact as detector. The amplitude of the spin valve signal ΔV_{nl} is used as a measure for the spin polarization. Right: Hysteresis loops of the two contacts.

surement does neither show the expected rectangular form as typically observed in spin valve experiments, nor the maximum achievable amplitude. However, the amplitude of the spin valve signal ΔV_{nl} can still be regarded as a good measure for the spin polarization in the heterostructure.

Figure 4.20 illustrates on the left hand side the bias-dependence of both the nonlocal voltage ΔV_{nl} and the Kerr rotation angle $\Delta\theta_{\mathrm{K}}$ using the same 2 µm wide contact as injector. The Kerr signal is detected directly underneath the injector contact. Both detection techniques show a similar bias dependence, which demonstrates the equivalence of both methods. Fig. 4.20 on the right shows a Hanle depolarization curve measured in a nonlocal voltage geometry without laser illumination on the cleaved edge. Just like in the case of magneto-optical detection, the measurement is free of dynamic nuclear polarization effects, since the contact magnetizations are reversed every $\sim$ 5 s. The Hanle curve can be well modeled with the diffusive theory. The fit yields a spin lifetime of $\tau_s = (1.6 \pm 0.5)$ ns, in good agreement with the optically detected spin lifetimes.

Recently, the spin lifetime in a similar sample has been calculated using the expression $\lambda_s = \sqrt{D_e \tau_s}$ with the electron diffusivity D_e determined from magneto-transport measurements and the spin decay length λ_s extracted from nonlocal spin valve measurements [127]. This simple estimation led to a spin lifetime in the range of a few tens of picoseconds, in accordance with former spin lifetime measurements of 2D electron systems confined in GaAs(001)-based quantum well structures [87–89, 124]. However, when performing Hanle experiments Oltscher *et al.* were able to detect nonlocal depolarization curves suggesting spin lifetimes in the range of a few nanoseconds [127], which is comparable to the present measurements. In Ref. [127] the observed Hanle signals have been linked to DNP

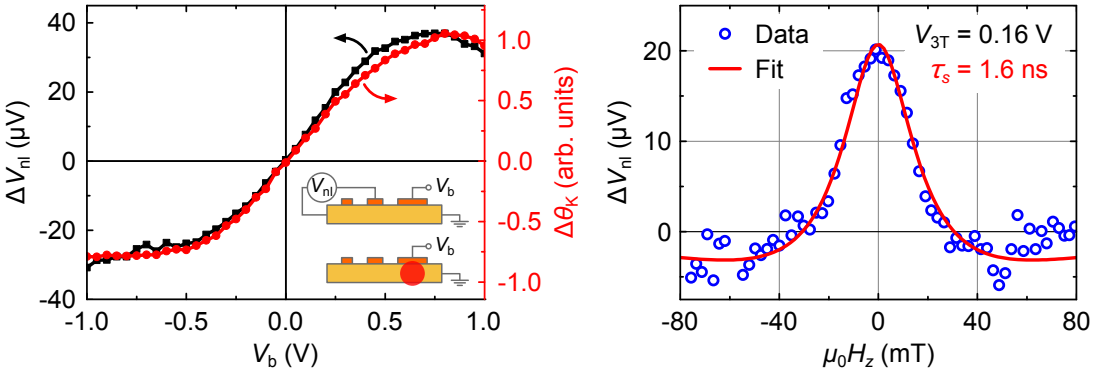

Figure 4.20.: Left: Comparison of the bias dependence of the nonlocal voltage ΔV_{nl} and the Kerr rotation angle $\Delta\theta_{\mathrm{K}}$. The insets illustrate the measurement configurations. Right: Hanle depolarization measurement of a sample from wafer B using the nonlocal voltage geometry without illuminating the sample with the laser. The fit yields a spin lifetime of $\tau_s = (1.6 \pm 0.5)$ ns.

effects appearing for certain bias conditions. However, as mentioned above, DNP cannot arise in the present experiment. To resolve the discrepancy between the spin lifetimes estimated via $\lambda_s = \sqrt{D_e \tau_s}$ and the lifetimes resulting from Hanle measurements one can consider two possible explanations:

First, as has already been pointed out in Ref. [127], the standard, diffusive model of spin injection [41–43] might be unsuitable to describe high-mobility 2D systems. In the case of Oltscher *et al.*, evaluating the data with the diffusive theory resulted in unphysical spin injection efficiencies larger than 100%. It has been argued that the standard model cannot be applied to samples with ballistic transport properties [127]. Therefore, naively modeling Hanle data with the standard model might lead to artificially enhanced spin lifetimes as the theory does not take into account the (quasi-)ballistic transport between injection and detection position. However, it seems unlikely that ballistic effects play a crucial role in the present Hanle measurements. In contrast to the process of spin injection, which is affected by ballistic tunneling [127], spin transport along a 40 µm wide transport channel should already exhibit diffusive transport characteristics. Thus, the Hanle effect, which is detected at a distance of a few micrometers to the injector contact, should still be governed by the spin drift-diffusion equations, which is further supported by the fact that the measured Hanle lineshapes can be well modeled with the diffusive theory (see Figs. 4.18 and 4.20 on the right hand side).

The second, more likely explanation for the difference between the spin lifetimes extracted from Hanle measurements and the lifetime estimation of Ref. [127] is the fact that the expression $\lambda_s = \sqrt{D_e \tau_s}$ might not be applicable in the case of a 2D electron system. Indeed, it has been argued that the high electron-electron scattering rates in high-mobility 2DEGs can lead to a reduction of the spin diffusivity D_s with respect to the charge diffusivity D_e [95–99], resulting in an enhanced spin relaxation time [75–78] (see Secs. 2.3.3 and 2.4). Therefore, spin relaxation is affected by D_s rather than D_e, suggesting that $\lambda_s = \sqrt{D_s \tau_s}$ should be the correct link between λ_s and τ_s. Using this expression one can estimate a value for the spin diffusivity D_s by measuring the spin decay length λ_s and the spin relaxation time τ_s. Fig. 4.21 shows an example for such a measurement, carried out on a sample from wafer B. The left hand side of this figure illustrates the spatial spin distribution in the 2D channel while injecting spins at $V_{3T} = -0.09\,\mathrm{V}$. An exponential fit to the data on the field-free side of the injecting contact yields a spin decay length of $\lambda_s = (3.3 \pm 0.2)\,\mu\mathrm{m}$. The right hand side of Fig. 4.21 shows the corresponding Hanle depolarization curve measured for the same bias condition with the laser spot being located at $y = 4\,\mu\mathrm{m}$. Fitting these Hanle data with λ_s being fixed at 3.3 µm suggests a spin lifetime of $\tau_s = (1.0 \pm 0.1)\,\mathrm{ns}$ (see Sec. 3.4.1 for details on the fitting procedure). Altogether, by taking these values for λ_s and τ_s one obtains a spin diffusivity of $D_s = \lambda_s^2/\tau_s \approx (110 \pm 20)\,\mathrm{cm}^2/\mathrm{s}$, which

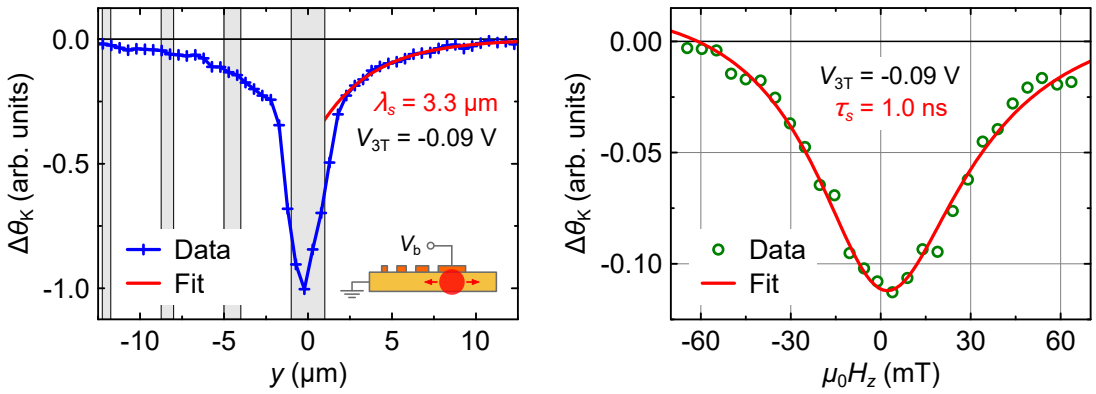

Figure 4.21.: Left: Linescan of the Kerr rotation angle along the 2DEG channel while injecting spins at $V_{3T} = -0.09\,\mathrm{V}$. An exponential fit in the field-free region yields a spin decay length of $\lambda_s = (3.3 \pm 0.2)\,\mu\mathrm{m}$. Right: Hanle depolarization curve measured at $y = 4\,\mu\mathrm{m}$. The fit yields a spin lifetime of $\tau_s = (1.0 \pm 0.1)\,\mathrm{ns}$.

is one order of magnitude smaller than the charge diffusivity $D_\mathrm{e} = 1300\,\mathrm{cm}^2/\mathrm{s}$ for this wafer.

As an alternative to the determination of D_s by measuring both λ_s and τ_s, the spin diffusivity can also be extracted from Hanle measurements alone without explicitly measuring the spin decay length. In the latter case D_s is used as an additional fitting parameter for the Hanle experiments. Fig. 4.22 shows the spin diffusivities determined with this method on a sample from wafer D, together with the spin diffusivities obtained with the above described method for wafer B, both measured for various bias conditions. All in all, the spin diffusivity is found to lie in a range from about 50 to $150\,\mathrm{cm}^2/\mathrm{s}$, which is between one and two orders of magnitude smaller than the corresponding charge diffusivities (cf. Tab. 4.1). A comparable reduction of D_s with respect to D_e has already been observed in Refs. [91, 100–102].

The large discrepancy between spin and charge diffusion can be understood by

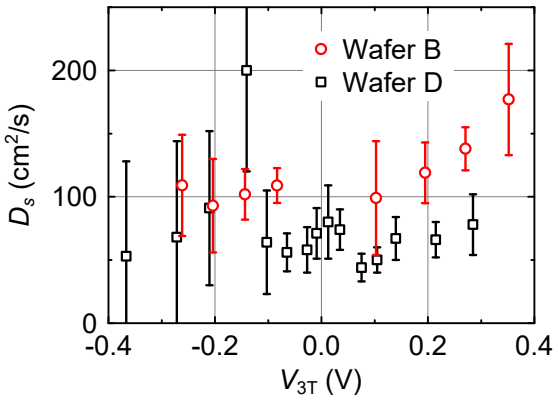

Figure 4.22: Spin diffusivities D_s for various bias conditions. The values for wafer B have been extracted from a combination of spin decay length and spin lifetime measurements via $D_s = \lambda_s^2/\tau_s$ (see Fig. 4.21). The data for wafer D represent fitting parameters from Hanle measurements.

taking electron-electron interactions into account as discussed in Sec. 2.4. Charge diffusion is governed by electron scattering events off impurities or phonons, thus the charge diffusivity D_e is determined by the momentum relaxation time τ_p of the electron ensemble (cf. Eq. 2.18). The ensemble momentum relaxation times for the present samples lie in a range between 8 ps and 19 ps at $T = 1.6\,\mathrm{K}$ (see Tab. 4.2). At this temperature τ_p is mainly limited by impurity scattering events. Up to about 10 K the momentum relaxation time exhibits only a slight temperature dependence; only for temperatures above $\sim 10\,\mathrm{K}$ the momentum relaxation time shows a significant decrease with temperature due to the onset of phonon scattering [137]. Spin diffusion, on the other hand, is determined by the momentum relaxation time τ_p^* of an individual electron, which additionally includes the contributions from electron-electron scattering (cf. Eqs. 2.7 and 2.8). Tab. 4.2 summarizes values for τ_p^* calculated at $T = 4.2\,\mathrm{K}$ and $T = 10\,\mathrm{K}$ for the wafers investigated above. At 4.2 K electron-electron scattering is found to be as strong as impurity scattering, which leads to an effective electron scattering rate $1/\tau_p^*$ being twice as large as the ensemble momentum relaxation rate $1/\tau_p$. At a temperature of 10 K, which corresponds to the temperature of the spin injection experiments presented above, τ_p^* even drops below 2 ps, which is roughly one order of magnitude smaller than τ_p. Thus, these considerations are in line with the observation that $D_s \ll D_\mathrm{e}$ and further substantiate the picture of electron-electron interactions playing a crucial role for the investigated 2DEG samples.

Table 4.2.: Electron scattering times in the four investigated heterostructure wafers. The ensemble momentum relaxation time τ_p is extracted from transport measurements. The effective electron scattering times τ_p^* are calculated with Eqs. 2.7 and 2.8.

wafer	τ_p	$\tau_p^*(4.2\,\mathrm{K})$	$\tau_p^*(10\,\mathrm{K})$
A	19 ps	7.4 ps	1.9 ps
B	8.0 ps	4.3 ps	1.4 ps
C	12 ps	6.4 ps	2.0 ps
D	12 ps	6.0 ps	1.8 ps

In summary, electrical spin injection into a GaAs-based, high-mobility 2DEG was investigated using electrical and optical measurement techniques. Similar to the data presented in Ref. [127] a signal enhancement is found in the bias dependence that may be attributed to a ballistic contribution to the injection process. Both detection methods independently show a clear Hanle depolarization, yielding averaged in-plane spin lifetimes of the order of one nanosecond. The experiments further suggest a spin diffusivity D_s which is significantly smaller than the charge diffusivity D_e. This finding underlines the important role of electron-electron interactions for 2D spin systems.

4.3. Thermal spin injection into n-GaAs

In the experiments discussed so far the spin accumulation in the GaAs conduction band was created via electrical spin injection, i.e. by driving a spin-polarized charge current through a ferromagnetic contact into the semiconductor. A quite different mechanism to create a spin imbalance in a semiconductor was reported in 2011 by Le Breton *et al.*, the so-called Seebeck spin tunneling [138]. Seebeck spin tunneling belongs to the class of spin caloritronic effects [139], which make use of the interplay between heat and spin transport. Le Breton *et al.* showed that a temperature gradient across a magnetic tunnel junction induces a pure spin current from the ferromagnet into the semiconductor. In contrast to electrical spin injection, thermal spin injection can in principle be achieved without employing charge currents, which dissipate energy. Thus, it might offer an energy-saving alternative to electrical spin injection and help to reduce energy consumption in future spintronic devices.

In this section, attempts to generate a thermal spin flow from an Fe contact into a bulk GaAs channel are presented. The experiment is based on former studies on thermal spin injection into n-GaAs carried out by B. Endres [22]. The temperature gradient across the Schottky tunnel barrier is created by utilizing Joule heating and the injected spin accumulation is detected by pMOKE measurements at the cleaved edge of the sample.

4.3.1. Seebeck spin tunneling

The basic working principle of Seebeck spin tunneling is sketched in Fig. 4.23, which illustrates the spin-resolved density of states of the semiconductor and the ferromagnet of a magnetic tunnel junction. The occupation of the electronic states is governed by the Fermi-Dirac statistics. In the ferromagnet, which is assumed to be at $T = 0$, all states below the Fermi level are occupied and all states above E_F are empty. In the hot semiconductor, on the other hand, a finite number of electrons is lifted above E_F due to their thermal energy, leaving an equal number of unoccupied states below E_F behind. The unequal occupation of the electronic states in the semiconductor and the ferromagnet leads to an energy dependent electron transfer between the two materials. Electrons with energy larger than E_F flow from the hot semiconductor to the cold ferromagnet; simultaneously, electrons below E_F tunnel in the opposite direction as denoted by the red arrows in Fig. 4.23. In an open-circuit geometry the total net charge current has to be zero, i.e. the electron currents above and below the Fermi level have to cancel each other. However, the two currents are spin-polarized. Thus, if the two oppositely oriented electron currents have different spin polarizations, a pure spin current across the tunnel barrier may arise [138].

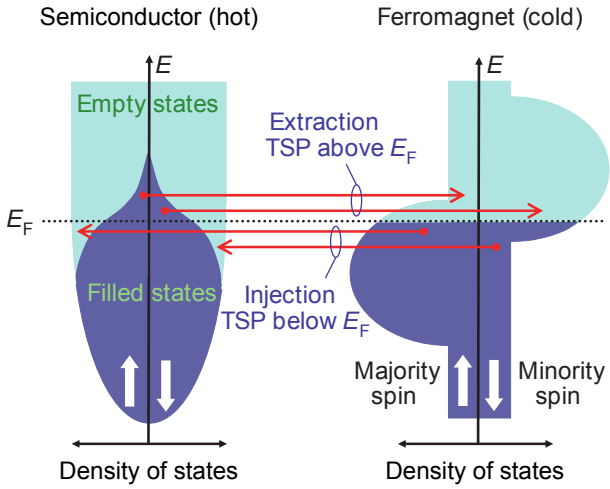

Figure 4.23.: Basic principle of Seebeck spin tunneling in a semiconductor/ferromagnet tunnel junction: electrons above E_F flow from the hot semiconductor to the cold ferromagnet, whereas electrons below E_F flow in the opposite direction. In an open-circuit geometry the total net charge current is zero. However, the tunneling electrons may carry a pure spin current if their tunnel spin polarizations (TSP) above and below E_F are unequal (adapted from [138]).

The spin current originating from Seebeck spin tunneling is not determined by the spin polarization of the tunnel barrier conductance P_Σ, but by its energy derivative $\partial P_\Sigma / \partial E$ at the Fermi level [138]. In principle, this derivative can become arbitrarily large, if one uses a tunnel junction with suitable material composition. The spin current arising from electrical spin injection, on the contrary, is limited by the spin polarization of the injecting charge current, which cannot exceed 100%. Thus, it has been argued that for properly designed tunnel junctions thermal spin injection should be more efficient than electrical spin injection [140]. Moreover, since the tunnel currents in the junction decay exponentially with barrier thickness, also the induced spin current decreases with increasing barrier width. For that reason thermal spin injection is expected to be most effective for narrow tunnel barriers [138, 140], in contrast to electrical spin injection, which requires a reasonably large tunnel resistance to overcome the conductivity mismatch between semiconductor and ferromagnet.

Thermal spin injection into silicon and germanium has by now been demonstrated by several groups (see Tab. 4.3). In all reported experiments the spin accumulation was detected utilizing a three-terminal Hanle geometry with only one ferromagnetic contact. In this technique a single contact is used both to inject and to detect the spin accumulation in the semiconductor at the same time and the spin signal is quantified by applying an external magnetic field and measuring the Hanle depolarization of the three-terminal voltage (cf. e.g. Refs. [146, 147]). The temperature gradient across the tunnel junction was applied by sending a

Table 4.3.: Overview about the reports on thermal spin injection into semiconductors via Seebeck spin tunneling. All experiments used a three-terminal Hanle geometry at room temperature to detect the spin accumulation. P_{max} denotes the maximum heating power density in the semiconductor channel. The resistance area products $R_{3\mathrm{T}}A$ of the tunnel contacts have been estimated from the reported I-V-characteristics of the tunnel contacts.

Reference	material system	P_{max} $\frac{\mathrm{nW}}{\mu\mathrm{m}^3}$	$R_{3\mathrm{T}}A$ $\Omega\mu\mathrm{m}^2$
Le Breton *et al.* [138]	Py/Al_2O_3/p-Si	7.6	$3 \cdot 10^7$
Jain *et al.* [141]	CoFeB/MgO/n-Ge	20000	$8 \cdot 10^6 - 5 \cdot 10^7$
Jeon *et al.* [142]	CoFe/MgO/n-Ge	667	$2 \cdot 10^6$
Jeon *et al.* [143]	CoFe/MgO/n-Si		$2 \cdot 10^6$
Dankert and Dash [144]	Co/SiO_2/n-Si	1200	$1 \cdot 10^6$
Jeon *et al.* [145]	CoFe/MgO/n-Si		$2 \cdot 10^6$
	CoFe/MgO/n-Ge		$1 \cdot 10^6$

Joule heating current either through the semiconductor or through the ferromagnet, or by employing a laser heating technique to increase the temperature of the ferromagnet. Although all authors report quite comparable spin splittings in the conduction band between 0.2 meV and 0.9 meV, the heating power densities to achieve these spin splittings differ by several orders of magnitude, as shown in Tab. 4.3. The authors of Refs. [141, 142] explain this large discrepancy with a less sophisticated sample design compared to Le Breton *et al.* [138].

Up to now Seebeck spin tunneling was not demonstrated for GaAs-based systems. Furthermore, since all reports are based on three-terminal Hanle measurements, an experiment employing other detection schemes like nonlocal spin valve or magneto-optical detection would be highly desirable. A first step in this direction has already been taken by B. Endres, who attempted to create a thermal spin accumulation by Joule heating and utilizing pMOKE detection at the cleaved edge of the sample [22]. However, in these experiments part of the heating current was shunted by the Fe/GaAs tunnel contact due to the low interface resistance of the two investigated samples of only $1 \cdot 10^4\,\Omega\mu\mathrm{m}^2$ and $4 \cdot 10^4\,\Omega\mu\mathrm{m}^2$. This current shunting made a direct observation of Seebeck spin tunneling impossible, as will be explained in more detail below.

4.3.2. Samples

The wafers that are used for the experiments on thermal spin injection have basically the same layer stack as the one that was investigated in Sec. 4.1 in

conjunction with electrical spin injection into bulk GaAs (cf. Fig. 4.1 on the left hand side). The spin imbalance is created in an n-doped GaAs layer of micrometer thickness grown on a semi-insulating GaAs(001) substrate. Spin injecting contacts are formed by a 15 nm thick n $\rightarrow$ n^{++} transition layer with gradually increasing doping level, a 15 nm thick layer of n^{++}-GaAs and a 2.5 nm thick Fe layer, followed by a 4 nm thick Au capping. The width of the resulting Schottky tunnel barrier is determined by the doping profile of the GaAs; details on that are given below.

The wafers are patterned by standard optical lithography using techniques similar to those described in Sec. 4.1.1. The contact geometry of the lateral devices is shown in Fig. 4.24. The sample preparation starts with the fabrication of an n-GaAs mesa channel. This is done by defining a 70 µm wide and 1.25 mm long strip of photoresist along the $[1\bar{1}0]$ crystallographic direction; subsequently, the Au and Fe layers besides the resist are removed by Ar ion etching and the n-doped GaAs layers are etched down to the undoped GaAs substrate using peracetic acid. Contacts are defined in two successive optical lithography steps and evaporation of Cr/Au. First, a U-shaped contact is patterned in the middle part of the mesa. This contact is later on used to electrically heat the Fe layer. Afterwards reference contacts and Au bonding pads to the U-shaped contact are fabricated. The latter have a thickness of $\sim$ 150 nm. The thickness of the U-shaped contact can be chosen to be thinner to enhance the heating current density on the mesa channel. The U-type contact can either be fabricated with a homogeneous thickness or in such a way that its middle part is thinner than its outer parts (see Fig. 4.24 on the right hand side). Finally, the Au, Fe and n^{++}-GaAs layers in between the contacts are removed by Ar ion and peracetic acid etching. For this last etching step the contacts are protected by an etching mask, defined by optical lithography, which is of particular importance for the thin U-shaped contact. The fabricated lateral device is then cleaved in the $[1\bar{1}0]$ direction across the mesa, reducing the channel width to about 40 to 50 µm and exposing the GaAs(110) surface at the cleaved edge.

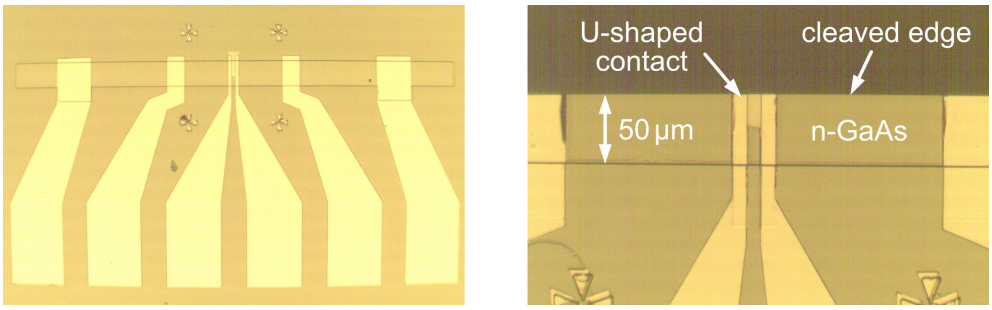

Figure 4.24.: Left: Micrograph of a sample for thermal spin injection prior to cleaving. Right: Zoom onto the center part of a cleaved sample. The U-shaped Au contact can be fabricated in such a way that its middle part is thinner than its outer parts.

4.3.3. Experimental Results

In the following samples from two different wafers are investigated employing pMOKE detection at the cleaved edge of the sample. The measurements are carried out at a base temperature of $\sim 10\,\mathrm{K}$. The first sample has a $1.5\,\mu\mathrm{m}$ thick n-GaAs channel with a nominal doping density of $N_\mathrm{D} = 2.5 \cdot 10^{16}\,\mathrm{cm}^{-3}$. The n^{++}-GaAs layer at the Fe/GaAs interface is doped up to about $6 \cdot 10^{18}\,\mathrm{cm}^{-3}$. Fig. 4.25 illustrates the I-V-characteristic of the resulting Schottky barrier. The characteristic was measured at a U-shaped contact with a homogeneous Au-layer thickness of 150 nm. Due to the high doping level of the $\mathrm{n} \rightarrow \mathrm{n}^{++}$ transition layer the contact exhibits an ohmic behaviour with a barrier resistance of $R_\mathrm{3T} = 83\,\Omega$. With the known contact area of about $2400\,\mu\mathrm{m}^2$, the resistance area product $R_\mathrm{3T}A$ of the contact is calculated to $2 \cdot 10^5\,\Omega\mu\mathrm{m}^2$. This value is one order of magnitude smaller than the $R_\mathrm{3T}A$ products of the tunnel contacts that were used for thermal spin injection into Si and Ge (see Tab. 4.3). Hence, since a thermal spin current is expected to increase with decreasing tunnel resistance [138, 140], thermal spin injection should be observable in the present sample.

Before discussing the experiments on Seebeck spin tunneling, electrical spin injection into the sample is demonstrated. For that purpose a bias voltage is applied between the U-shaped contact and a reference contact on the end of the transport channel and the Kerr rotation is detected in the n-GaAs channel underneath the U-type contact. Fig. 4.26 shows the magnetic field dependence of the Kerr rotation angle θ_K at $V_\mathrm{b} = 10\,\mathrm{V}$. The hysteresis loop reflects the magnetization reversal process of the Fe contact along the [110] direction, thus demonstrating electrical spin extraction from the semiconductor channel into the Fe contact. As usual, the height of the hysteresis loop $\Delta\theta_\mathrm{K}$ is used as a measure for the spin accumulation in the GaAs. Beyond that, the measurement in Fig. 4.26 contains a second piece of information, which manifests in the fact that the hysteresis loop is not symmetrically centered around $\theta_\mathrm{K} = 0$. This offset $\theta_\mathrm{K}^\mathrm{offset}$ (calculated as the average of both remanent θ_K-values) arises from a not spin-related, electro-optic contribution to the Kerr effect. Since the experiment is based on a lock-in

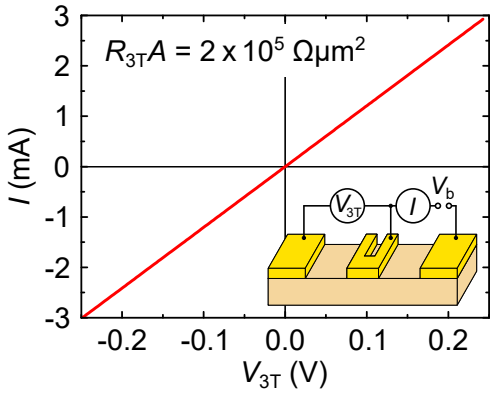

Figure 4.25: I-V-characteristic of the U-shaped Schottky barrier contact of sample 1 (contact area: $2400\,\mu\mathrm{m}^2$). The inset illustrates the measurement geometry.

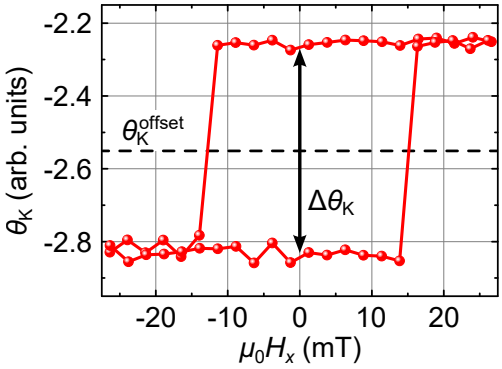

Figure 4.26: Hysteresis loop of the Kerr rotation in the n-GaAs channel while electrically extracting spins at $V_b = 10\,V$. The height of the hysteresis loop $\Delta\theta_K$ is a measure for the spin accumulation. The non-zero offset θ_K^{offset} arises from the electro-optic contribution to the Kerr effect.

technique, which is phase sensitive to the square-wave modulated injection current, this electro-optic contribution has to stem from the injection current itself. Therefore, the offset Kerr signal θ_K^{offset} can provide information about the electric field distribution of the injection current in the n-GaAs channel. This is shown in Fig. 4.27, which displays linescans of both $\Delta\theta_K$ and θ_K^{offset} along the n-GaAs channel while injecting ($V_b = -10\,V$) and extracting ($V_b = +10\,V$) spins at the 60 µm wide U-shaped contact. The left part of the figure illustrates the spatial distribution of the spin accumulation underneath the contact. For $V_b = +10\,V$ electrons are driven from the reference contact on the right end of the channel into the U-type contact and induce a spin polarization by majority spin extraction; for $V_b = -10\,V$ electrons flow from the contact to the right and inject majority spins. In both cases the spin accumulation is exclusively concentrated on the right edge of the contact. For spin injection the applied electric field additionally drives the spin-polarized electrons to the right, which leads to a significant spin accumulation outside the contact region; in contrast for spin extraction the electric field pushs the spins underneath the contact region. Hence, in this case the spin density decays to a negligible value next to the contact. The observation

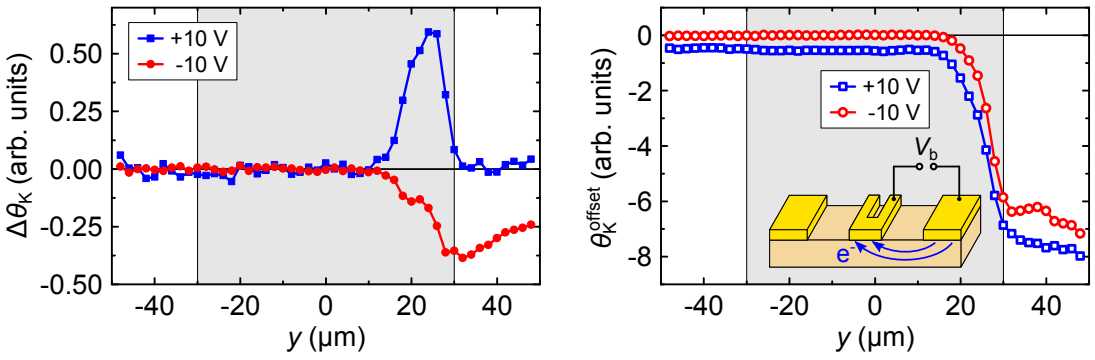

Figure 4.27.: Linescans of the Kerr rotation angle (left: $\Delta\theta_K$, right: θ_K^{offset}) along the n-GaAs channel for electrical spin injection ($V_b = -10\,V$) and spin extraction ($V_b = +10\,V$) in sample 1. The shaded region indicates the position of the U-shaped contact. The inset illustrates the current path within the sample.

that the spin accumulation is mainly localized on the right contact edge can be explained with the low interface resistance of the injecting contact compared to the channel resistance, as was already discussed earlier in Ref. [19]. The channel resistance underneath the contact region is of the same order of magnitude as the tunnel resistance. Therefore, the current flows mainly on the right edge into the contact. The Kerr offset signal $\theta_{\mathrm{K}}^{\mathrm{offset}}$ substantiates this interpretation (see Fig. 4.27 on the right hand side). It has a large value to the right of the contact, where the injection current exclusively flows in the n-GaAs channel. However, as soon as the injection current enters the contact region, $\theta_{\mathrm{K}}^{\mathrm{offset}}$ drops within about 15 µm to almost zero, since the current flows here from the n-GaAs into the Au/Fe contact. Thus, $\theta_{\mathrm{K}}^{\mathrm{offset}}$ indeed reflects the electric field distribution in the n-GaAs channel, providing a useful tool to interpret the Joule heating experiments discussed below.

For the Seebeck spin tunneling experiments a Joule heating current is driven either through the n-GaAs channel or through the U-shaped Au contact in order to create a temperature gradient across the Schottky barrier. Just like in the case of electrical spin injection, the current is modulated in the form of a unipolar square-wave; thus, the temperature gradient (and consequently the resulting thermal spin current) is periodically switched on and off and the same lock-in technique as for electrical spin injection can be used [22]. Fig. 4.28 on the left illustrates linescans of the Kerr rotation along the transport channel while passing a heating current through the semiconductor. For that purpose a voltage of $\pm 10\,\mathrm{V}$ is applied between the two reference contacts at the ends of the channel. Similar to the case discussed above, the spin accumulation is mainly concentrated on the contact edges. However, here a spin density is present at both ends of the Fe contact and the spin polarizations at the two opposing contact edges have a different sign. Moreover, the general shape of the spin distribution is mirrored at $y = 0$ when the direction of the heating current is changed. Thus, the observed spin accumulation cannot stem from a thermal spin current. Instead, the measurements can be explained by ordinary electrical spin injection, if one considers that the heating current is shunted by the Fe contact (see inset of Fig. 4.28 on the right). The heating current enters the Fe contact at one contact edge and leaves it at the other edge, thus creating an electron spin accumulation by spin extraction and injection at the two edges. Exactly the same current shunting effect has already been observed by B. Endres on similar samples [22]. The electro-optic Kerr signal $\theta_{\mathrm{K}}^{\mathrm{offset}}$, which is shown in Fig. 4.28 on the right, confirms this explanation. It has a large value outside the contact region, where the heating current induces a strong electro-optic Kerr effect in the GaAs. Right at the contact position, however, the signal drops to zero, as the heating current flows here through the Au/Fe contact and not through the semiconductor. Thus, the GaAs underneath the Schottky barrier is not heated at all. Since almost 100% of the heating current seem to be shunted by the thick Au/Fe contact, one could expect that

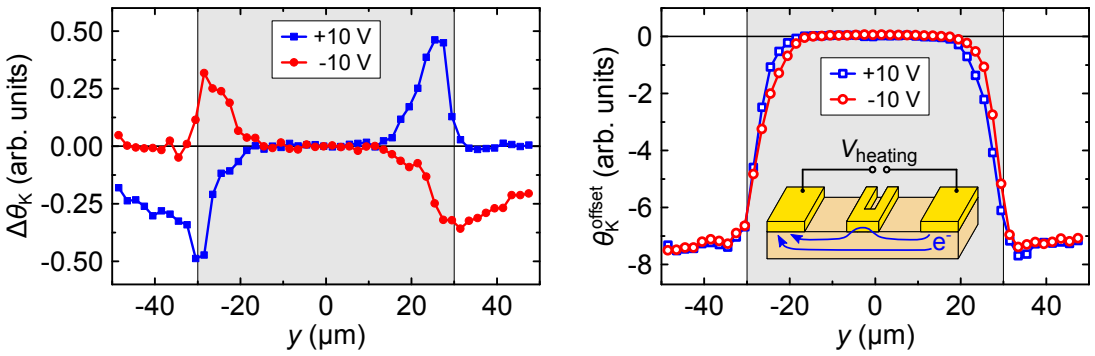

Figure 4.28.: Linescans of the Kerr rotation angle (left: $\Delta\theta_\mathrm{K}$, right: $\theta_\mathrm{K}^\mathrm{offset}$) along the n-GaAs channel of sample 1 while heating the semiconductor with an electron current from right to left (+10 V) and vice versa (−10 V).

actually the Fe layer in the middle part of the contact might be heated. However, the absence of any significant Kerr rotation $\Delta\theta_\mathrm{K}$ in this region demonstrates that there is no thermal spin current arising from a possible Fe heating.

When a heating current is passed through the U-shaped Au contact in order to increase the temperature of the Fe with respect to the GaAs, a similar current shunting effect can be observed. This is shown in Fig. 4.29, where the Au was heated with a current of ±58 mA. Here, a part of the heating current flows into the GaAs and thereby creates a small, electrically induced spin accumulation at the contact edges. However, due to the low resistance of the Au the current shunting is here less pronounced than in the case of the GaAs heating. The corresponding $\theta_\mathrm{K}^\mathrm{offset}$ signal confirms the presence of part of the heating current in the GaAs by a small but non-zero signal underneath the contact. The measurement even suggests the presence of a quite strong electric stray field outside the contact region.

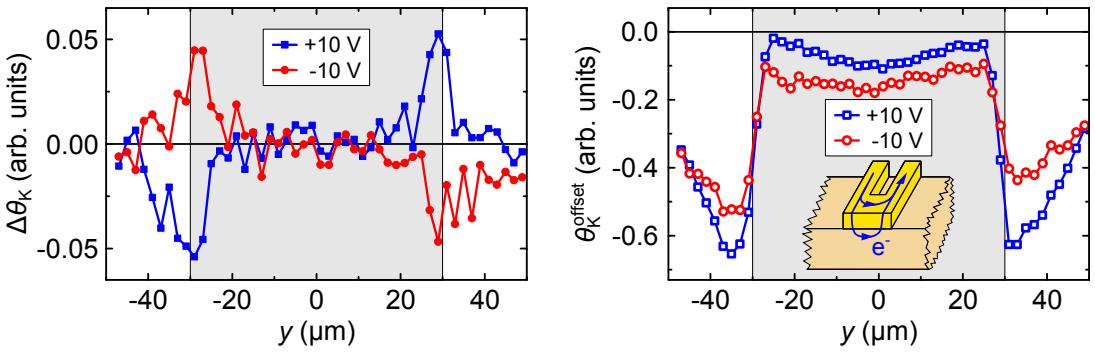

Figure 4.29.: Linescans of the Kerr rotation angle (left: $\Delta\theta_\mathrm{K}$, right: $\theta_\mathrm{K}^\mathrm{offset}$) along the n-GaAs channel of sample 1 while heating the ferromagnet by driving a heating current of 58 mA through the Au/Fe contact layers.

These measurements show that electrical heating cannot be used to create a temperature difference between the Fe and the GaAs in this sample due to its low interface resistance of only $2 \cdot 10^5\,\Omega\mu m^2$. Therefore, a second sample from another wafer was prepared. This second wafer has a 2 µm thick n-GaAs layer with a nominal doping density of $N_D = 4 \cdot 10^{16}\,cm^{-3}$. The thickness of the n^{++}-GaAs layer at the Fe/GaAs interface is reduced to 10 nm and the doping in this region is lowered to $4 \cdot 10^{18}\,cm^{-3}$. The smaller doping density at the Fe/GaAs interface leads to the formation of a wider Schottky barrier for sample 2, as can be seen from the I-V-characteristic of its U-type contact (see Fig. 4.30). The characteristic indicates a strongly rectifying behaviour of the Schottky contact with a large resistance in reverse direction. At $V_{3T} = -3\,V$ the resistance is roughly $1 \cdot 10^7\,\Omega\mu m^2$, which is comparable to the tunnel resistance reported by Le Breton *et al.* [138]; in the vicinity of $V_{3T} = 0$ the resistance is even larger. Thus, current shunting by the tunnel barrier should play a less important role for this sample.

Figure 4.31 displays a linescan of the Kerr rotation angle along the cleaved edge underneath the U-type contact, while electrically extracting spins at $V_b = 10\,V$. The bias voltage is applied between the 60 µm wide U-shaped contact (with a homogeneous Au layer thickness of $\sim$ 150 nm above the Fe) and a reference contact on the left end of the electron transport channel. The measurement reveals a large spin accumulation underneath the Fe contact. In this sample the resistance of the Schottky barrier is much larger than the channel resistance. Thus, in contrast to sample 1, the density of the injection current shows a gradual decrease along the channel from the left to the right edge of the Fe contact (see Fig. 4.31 on the right), which results in an almost homogeneous spin current across the whole contact area (cf. also Ref. [19]). This in turn induces a more or less uniform spin accumulation along the whole contact length as shown in Fig. 4.31 on the left.

Figure 4.32 illustrates a linescan of the Kerr rotation angle while electrically heating the Fe layer by driving a current of 50 mA through the U-shaped contact. The

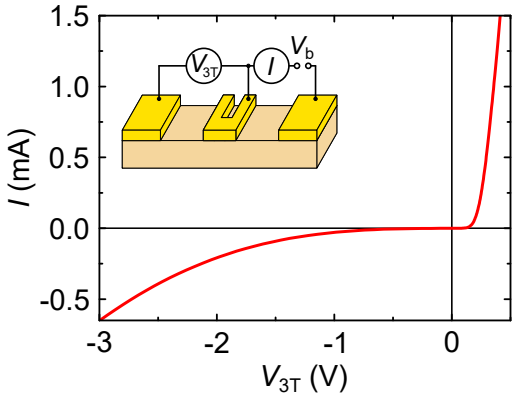

Figure 4.30: I-V-characteristic of the Schottky barrier of sample 2 (contact area: 2400 µm^2). The inset illustrates the measurement geometry.

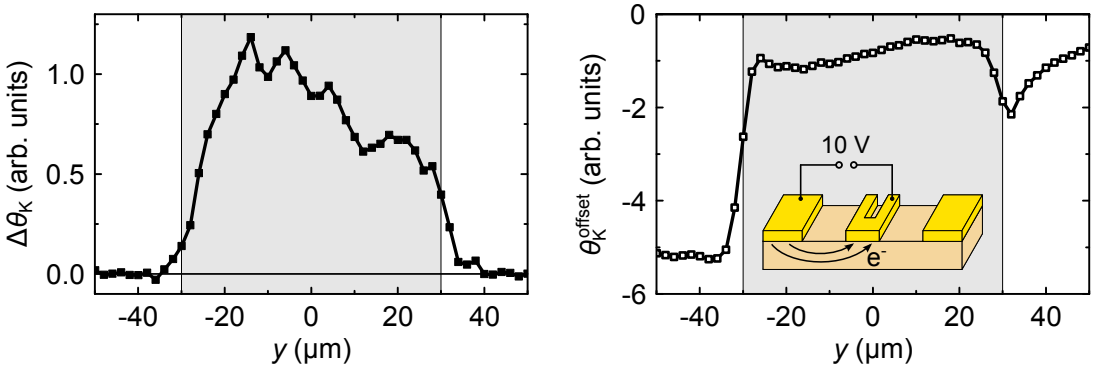

Figure 4.31.: Linescan of the Kerr rotation angle (left: $\Delta\theta_\mathrm{K}$, right: $\theta_\mathrm{K}^\mathrm{offset}$) along the n-GaAs channel for electrical spin extraction at $V_\mathrm{b} = 10\,\mathrm{V}$ in sample 2.

measurement of the electro-optic Kerr signal shows that the heating current does not enter the n-GaAs channel. Hence, the large interface resistance in conjunction with the low resistance of the thick Au U-type contact prevents a current shunting in this case. However, no significant thermal spin accumulation can be detected. A reason for the absence of the latter might be the $\sim 150\,\mathrm{nm}$ thick Au layer above the Fe, which acts as an efficient heat sink and thus might inhibit the emergence of a large enough thermal gradient across the interface. Heating the n-GaAs channel, on the other hand, does not create any significant thermal spin accumulation either (see Fig. 4.33). Here, the electro-optic Kerr signal shows a reduction right at the contact position with respect to the signal next to the contact. However, $\theta_\mathrm{K}^\mathrm{offset}$ does not fully vanish underneath the contact. This suggests that at least some part of the heating current flows through the GaAs channel, in contrast to sample 1, where the heating current was completely shunted by the Au/Fe contact. All in all, the large interface resistance of sample 2 successfully suppresses the current shunting effect. However, again no significant thermal spin accumulation can be observed.

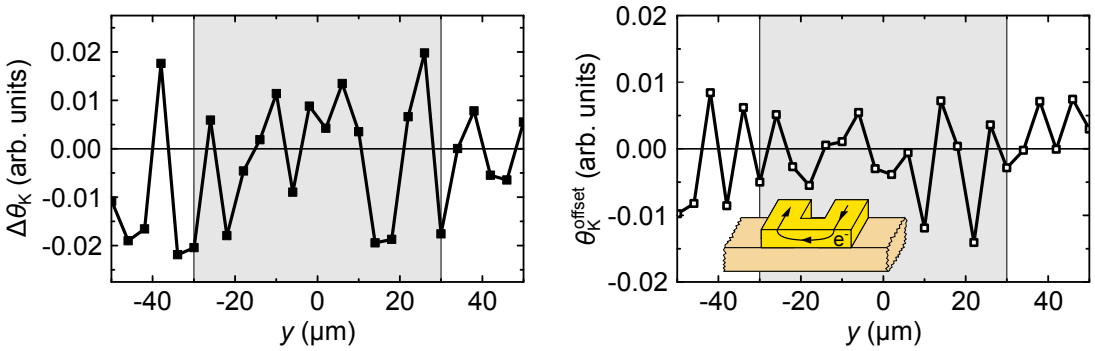

Figure 4.32.: Linescan of the Kerr rotation angle (left: $\Delta\theta_\mathrm{K}$, right: $\theta_\mathrm{K}^\mathrm{offset}$) along the n-GaAs channel of sample 2 while heating the ferromagnet by driving a heating current of 50 mA through the Au/Fe contact layers.

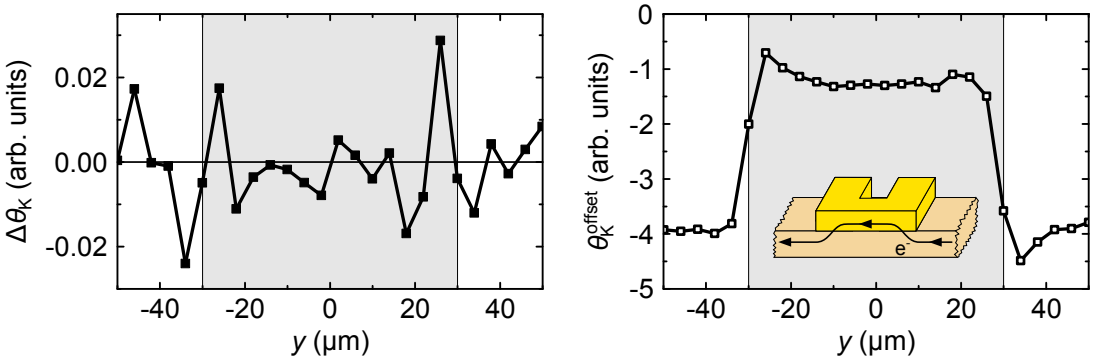

Figure 4.33.: Linescan of the Kerr rotation angle (left: $\Delta\theta_\mathrm{K}$, right: $\theta_\mathrm{K}^\mathrm{offset}$) along the n-GaAs channel of sample 2 while heating the semiconductor with an electron current. The heating power density in the GaAs is $\sim 350\,\mathrm{nW}/\mu\mathrm{m}^3$.

Since in sample 2 no current shunting is observed when heating the Fe contact, another sample was fabricated from the same wafer. This sample has a 30 µm wide U-shaped Au contact, whose thickness is reduced to 20 nm in the middle 10 µm wide section. Due to the reduced thickness in the middle part of the heater a larger current density and thus a larger temperature gradient can be expected. However, when driving a current through this structure, again a large electro-optic Kerr signal $\theta_\mathrm{K}^\mathrm{offset}$ can be detected in the n-GaAs underneath the contact (see Fig. 4.34 on the right), which indicates that the heating current is shunted by the GaAs channel. $\theta_\mathrm{K}^\mathrm{offset}$ is largest in the middle third of the heater; this suggests that the heating current flows into the GaAs channel in order to avoid the 20 nm thin part of the heater contact. Therefore, again no efficient Fe heating can be achieved and consequently the magneto-optic Kerr signal $\Delta\theta_\mathrm{K}$, which is shown in Fig. 4.34 on the left, does not reveal any significant thermal spin accumulation.

Nevertheless, the observation that the heating current is not flowing through the

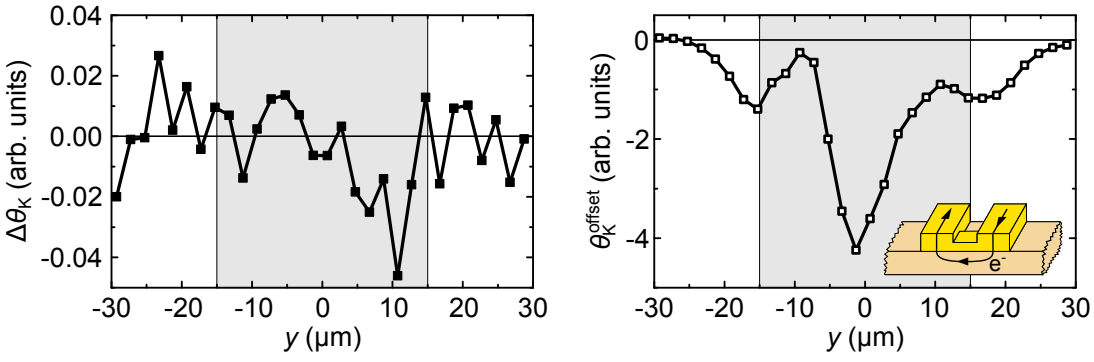

Figure 4.34.: Linescan of the Kerr rotation angle (left: $\Delta\theta_\mathrm{K}$, right: $\theta_\mathrm{K}^\mathrm{offset}$) along the n-GaAs channel of sample 3 while heating the ferromagnet by driving a heating current through the Au/Fe contact layers.

thin part of the U-type contact offers the possibility to electrically heat the semiconductor without a current shunting in this region. This is shown in Fig. 4.35, where the heating current is sent through the n-GaAs channel. The electro-optic Kerr signal $\theta_{\mathrm{K}}^{\mathrm{offset}}$ drops significantly in the outer parts of the U-shaped contact, indicating that the current flows here into the $\sim 150\,\mathrm{nm}$ thick Au layer above; however, in the middle, 20 nm thin part of the heater contact $\theta_{\mathrm{K}}^{\mathrm{offset}}$ has the same value as next to the contact. Thus, here the current is exclusively flowing in the semiconductor underneath the Fe contact and therefore should provide an efficient heating of the semiconductor. However, although the GaAs is heated with power densities up to $\sim 6000\,\mathrm{nW}/\mu\mathrm{m}^3$, no significant thermal spin accumulation can be detected. Note that other samples have been heated with even larger power densities. However, even for power densities, which reach the values reported by Jain *et al.* (cf. Tab. 4.3), no significant thermal spin current into the GaAs could be generated.

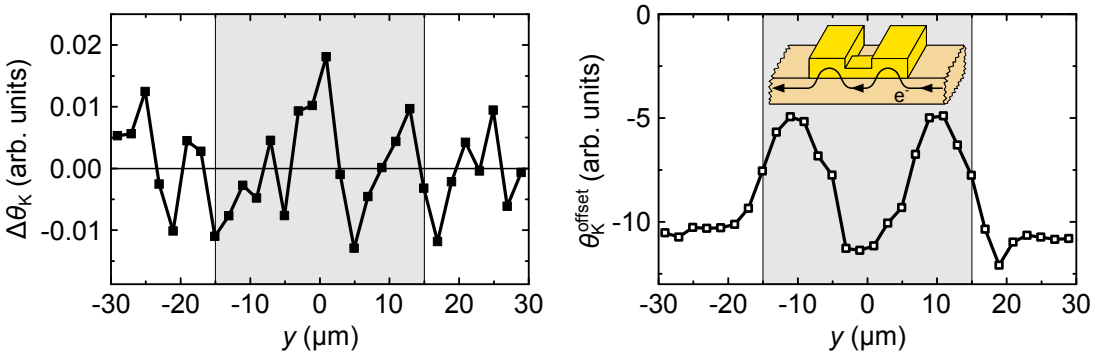

Figure 4.35.: Linescan of the Kerr rotation angle (left: $\Delta\theta_{\mathrm{K}}$, right: $\theta_{\mathrm{K}}^{\mathrm{offset}}$) along the n-GaAs channel of sample 3 while driving a heating current through the semiconductor. The heating power density in the GaAs is $\sim 6000\,\mathrm{nW}/\mu\mathrm{m}^3$.

4.3.4. Discussion

Altogether, the experiments demonstrate that Joule heating is no reliable way to observe Seebeck spin tunneling in the present Fe/GaAs devices. The current shunting effect, which can be observed in samples with transparent tunnel barriers, can in principle be avoided by using a highly blocking tunnel barrier. However, in this case no significant thermal spin accumulation can be detected. The absence of a thermal spin current in such samples may not be surprising, since according to Refs. [138, 140] Seebeck spin tunneling is expected to be suppressed by a large tunnel resistance. On the other hand, the use of samples with an ohmic barrier, which is expected to be beneficial for thermal spin injection, does not allow to directly observe a thermal spin accumulation either. In this case the current shunting effect hampers the emergence of a temperature gradient

across the tunnel barrier and a spin accumulation may be injected by the heating current via ordinary electrical spin injection instead of Seebeck spin tunneling.

Nevertheless, thermal spin injection into sample 1 should be feasible due to its rather low interface resistance (see Fig. 4.25), if one applies a thermal gradient across the Schottky barrier without employing Joule heating currents (e.g. by utilizing laser heating of the ferromagnet as done in Refs. [142, 143]). The spin polarization of the electronic states around E_F, which are responsible for Seebeck spin tunneling, can in principle be probed by electrical spin injection at low bias voltages. Fig. 4.36 shows on the left hand side the bias dependence of the spin signal $\Delta\theta_\mathrm{K}$ in sample 1 while electrically injecting spins at the U-shaped contact. The measurement demonstrates that spin extraction is roughly twice as efficient as spin injection. According to the basic working principle of Seebeck spin tunneling (see Fig. 4.23) spin injection is sensitive to the spin polarization of the tunnel barrier conductance P_Σ below the Fermi level, whereas spin extraction is determined by the spin polarization P_Σ above E_F. Thus, the non-linear behaviour of the bias dependence of $\Delta\theta_\mathrm{K}$ in sample 1 suggests that this sample should be suitable to generate a thermal spin imbalance. As discussed in Sec. 2.2.1 the spin accumulation μ_s arising from electrical spin injection is given by [43]

$$\mu_s = R_\mathrm{N} P_\Sigma j, \tag{4.4}$$

where $R_\mathrm{N} = \rho_\mathrm{N}\lambda_s$ is the spin resistance of the GaAs and j is the density of the injection current I. Thus, since $\Delta\theta_\mathrm{K}$ is proportional to the spin accumulation μ_s in the GaAs, the quantity $\Delta\theta_\mathrm{K}/I$ provides a measure for P_Σ. Fig. 4.36 shows on the right hand side the bias dependence of $\Delta\theta_\mathrm{K}/I$. The data suggest that P_Σ increases more or less linearly for low bias voltages. Hence, the measurement reveals, that sample 1 has a non-zero energy derivative $\partial P_\Sigma/\partial E$ in the vicinity of the Fermi level and therefore it basically meets all prerequisites for the successful generation

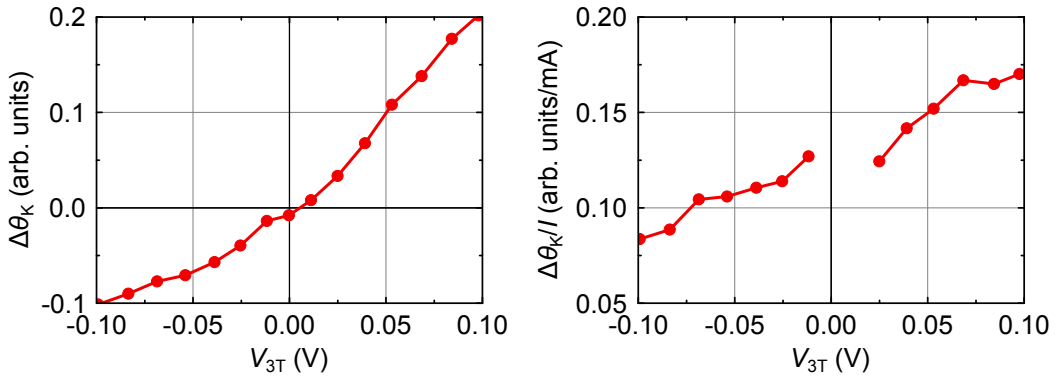

Figure 4.36.: Left: Bias dependence of the spin signal $\Delta\theta_\mathrm{K}$ while electrically injecting spins in sample 1. The measurement was performed with the laser spot located at $y = 18\,\mu\mathrm{m}$ (see Fig. 4.27). Right: The same data normalized to the injection current I.

of a thermal spin current. Similar profiles for $P_\Sigma(E)$ have been assumed in Ref. [138] to explain the Seebeck spin tunneling effect on a phenomenological basis using a free-electron model.

Seebeck spin tunneling arises from a temperature difference ΔT between ferromagnet and semiconductor. The authors of Refs. [138, 142, 144] expect ΔT to lie well below 1 K in their samples; nevertheless Refs. [138, 140] suggest that differences up to 10 K should be feasible. Since the Seebeck coefficient of tunnel junctions is of the order of $\sim 100\,\mu\mathrm{V/K}$, this temperature difference results in a Seebeck voltage across the interface of roughly 1 mV [140]. This value is consistent with the simple model of Seebeck spin tunneling presented in Fig. 4.23, where the electron tunnel currents arise from the different occupation of the density of states of the ferromagnet and the semiconductor. The Fermi-Dirac statistics exhibits an energy smearing around E_F of the order of $4k_\mathrm{B}T$ [26]. Thus, assuming that the ferromagnet is cooled to $T = 0$ and the semiconductor is heated to $T = 10\,\mathrm{K}$, only electrons in an energy range of about $\pm 2\,\mathrm{meV}$ around the Fermi level can contribute to a thermal spin transport. For sample 1 electrical spin injection and extraction at $V_{3\mathrm{T}} = \pm 2\,\mathrm{mV}$ is below the detection limit of the optical setup. The corresponding current density j across the Fe contact is of the order of $1 \cdot 10^4\,\mathrm{A/m^2}$. By taking a spin injection efficiency of $P_\Sigma = 30\%$ for low bias voltages [17] and the spin resistance of sample 1 of $R_\mathrm{N} = 1.5 \cdot 10^3\,\Omega\mu\mathrm{m}^2$, this results in a spin accumulation μ_s of the order of $\sim 5\,\mu\mathrm{V}$. Since thermal spin injection originates from the counterflow of electrons above and below the Fermi level with a spin polarization P_Σ comparable to the case of electrical spin extraction and injection at $|V_{3\mathrm{T}}| \leq 2\,\mathrm{mV}$, the resulting thermal spin accumulation μ_s^th is expected to lie well below $5\,\mu\mathrm{V}$. Indeed, the free-electron model, that was used by Le Breton *et al.* to explain Seebeck spin tunneling, also suggests maximal thermal spin accumulations μ_s^th of the order of $\sim 5\,\mu\mathrm{V}$ for a temperature difference of $\sim 1\,\mathrm{K}$ across the tunnel junction [138, 142]. Thus, one can conclude that a thermal spin current cannot induce a detectable spin accumulation in this sample.

The efficiency of thermal spin injection can be described by introducing the Seebeck spin tunneling coefficient S_st, which is defined by [138, 140]

$$S_\mathrm{st} = \frac{2\mu_s^\mathrm{th}}{\Delta T}. \tag{4.5}$$

Both the considerations on sample 1 presented above and the free-electron model of Le Breton *et al.* suggest that S_st should be smaller than $10\,\mu\mathrm{V/K}$. However, contrary to their own theory Le Breton *et al.* as well as all other authors in Tab. 4.3 experimentally find large three-terminal Hanle signals of more than $100\,\mu\mathrm{V}$, from which the authors calculate a Seebeck spin tunneling coefficient S_st of the order of $1\,\mathrm{mV/K}$ (cf. e.g. Refs. [138, 142, 144]). Le Breton *et al.* explain the large discrepancy between theory and experiment with shortcomings of their

model due to the unknown shape of $P_\Sigma(E)$ and the neglect of magnon-assisted tunneling, which is expected to enhance the Seebeck voltage across the tunnel barrier [148] and thereby also the Seebeck spin tunneling coefficient. However, the spin accumulations, which are obtained with three-terminal Hanle experiments, exceed not only the theoretical expectations for thermal spin injection by several orders of magnitude, but also for ordinary electrical spin injection [149, 150]. Moreover, three-terminal Hanle signals show an anomalous scaling with the resistance of the tunnel barrier [151], making these experiments especially sensitive to samples with a large interface resistance. The unexpectedly large signals have been explained by the presence of a spin accumulation in localized electronic states at the semiconductor/oxide interface, which greatly enhances the detected voltage signals [152, 153]. Thus, today it is believed that three-terminal Hanle experiments are sensitive to the spin imbalance at the ferromagnet/semiconductor interface, rather than to the spin accumulation in the semiconductor [150]. In this sense, three-terminal Hanle measurements provide in general no reliable values for the magnitude of the spin polarization in the semiconductor.

What is even more important is the observation that Lorentzian-shaped magnetoresistance effects can be obtained even in all-nonmagnetic tunnel junctions, i.e. without employing a ferromagnetic electrode and thus without a source for a spin-polarized current [154, 155]. These findings were attributed to resonant tunneling via impurity states within the tunnel barrier, which applies both for nonmagnetic and magnetic tunnel junctions [154, 156] and thus provides another possible explanation for the unexpectedly large, Hanle-like signals in three-terminal experiments. Most importantly, Song and Dery argue that the three-terminal Hanle signals, detected by Le Breton *et al.* in their thermal spin injection experiments, originate predominantly from this impurity-assisted tunneling mechanism caused by the heating current flowing past the tunnel barrier, and not from Seebeck spin tunneling [156].

Recently, Wagner *et al.* estimated the electronic contribution to thermal spin injection in an Fe/GaAs heterostructure with a layer stack similar to the samples investigated in this work [157]. In these experiments the samples were patterned into nonlocal spin valve devices and characterized utilizing all-electrical measurement techniques. Instead of actually generating a temperature difference between the ferromagnet and the semiconductor by employing a Joule or laser heating approach, the authors apply an electrical noise source to the injector contact in order to mimic a temperature gradient across the Fe/GaAs Schottky barrier. The low amplitude voltage noise induces electrical spin injection and extraction across the tunnel barrier, and thus probes the spin polarization of the tunneling electrons at energies slightly below and above the Fermi level in a similar way to the Seebeck spin tunneling mechanism. The effective temperature difference between the Fe and the GaAs is determined by the standard deviation of the Gaussian distributed voltage fluctuations (see Ref. [157] for details). From their

noise-driven nonlocal spin valve measurements Wagner *et al.* deduce an effective spin-dependent Seebeck coefficient of 33 pV/K [157], which suggests that the electronic contribution to thermal spin injection in Fe/GaAs is negligibly small. Indeed, such a low value of S_{st} would require temperature differences of the order of several thousand Kelvin across the Fe/GaAs junction, in order to create a measurable thermal spin accumulation in the GaAs, which is clearly unfeasible in standard Joule heating experiments. It should be mentioned, however, that the noise-based experiments of Wagner *et al.* do not take an increased magnon or phonon temperature in the sample into account. Thus, they do not make any statement as to what extent magnon- or phonon-assisted tunneling might enhance the Seebeck spin tunneling coefficient. Nevertheless, the results of Wagner *et al.* clearly demonstrate that heating the electron system alone is not sufficient to generate a detectable thermal spin current in Fe/GaAs. Finally, note that Wagner *et al.* did not only carry out a noise-based investigation of thermal spin injection, but also attempted to directly observe thermal spin injection in Fe/GaAs by utilizing both Joule and laser heating approaches in conjunction with nonlocal detection. However, just like in the present work, it was not possible to unambiguously identify any significant thermal spin signals [158].

In summary, Seebeck spin tunneling through Fe/GaAs Schottky barriers was investigated by employing pMOKE detection at the cleaved edge and a Joule heating approach. Similar to the results presented by B. Endres [22] no significant thermal spin accumulation could be detected. At least one of the investigated samples meets all prerequisites for the successful generation of a thermal spin imbalance, namely a narrow tunnel barrier and a non-vanishing energy derivative of P_{Σ} at the Fermi edge. Nevertheless, the experiments suggest a small Seebeck spin tunneling coefficient S_{st} well below 10 µV/K, in accordance with the Seebeck spin tunneling theory [138] and the findings of Wagner *et al.* [157, 158]. In contrast, three-terminal Hanle experiments yield huge thermal spin signals in Si and Ge-based systems with oxide tunnel barriers, resulting in Seebeck spin tunneling coefficients, which are orders of magnitude larger than expected. This large discrepancy casts doubt on the proposed efficiency of thermal spin injection into semiconductors, especially as the real origin of the three-terminal Hanle signals is still subject of a controversial debate.

5. Summary and outlook

In this work electron spin injection from ferromagnetic Fe or (Ga,Mn)As contacts into GaAs-based heterostructure systems was investigated by employing scanning Kerr microscopy at the cleaved edge of the samples. This magneto-optical measurement technique provides a direct insight into the spatial distribution of the spin density in the semiconductor channel. Furthermore, the dynamical properties of the spin accumulation can be investigated by performing Hanle depolarization measurements.

In the first experiment electrical spin injection from Fe into an n-doped bulk GaAs channel was demonstrated. The results obtained from the magneto-optical measurements are consistent with earlier observations on spin injection into n-GaAs and are in particular in line with previously reported values for the spin diffusion length λ_s and the spin lifetime τ_s. The spatial distribution of the spin ensemble in the semiconductor channel revealed an exponential decay of the spin accumulation outside the contact region with a spin diffusion length of roughly 4 µm. The spin lifetime was determined to 9.5 ns. Moreover, the experiment suggested that spin diffusion and charge diffusion have comparable strengths, which confirms the widely used assumption $D_s = D_\mathrm{e}$ for electrical spin injection into a bulk semiconductor.

Subsequently, electrical spin injection into a high-mobility 2DEG confined at a GaAs/(Al,Ga)As interface was investigated. Performing optical measurements on such a system is a delicate subject, since illumination creates a parallel conduction path in the (Al,Ga)As underneath the 2DEG. However, magnetotransport measurements demonstrated that transport through the illuminated heterostructure is still dominated by the 2DEG due to its high electron mobility. Moreover, a possible spin polarization in the parasitic transport channel cannot contribute to the Kerr signal, since the optical setup is exclusively sensitive to the spin density in the GaAs. Linescan measurements of the spin accumulation at the cleaved edge of the sample resulted in spin decay lengths in a range from about 2 µm to 7 µm, which is consistent with the findings of all-electrical detection schemes. Both magneto-optical and nonlocal detection methods show a clear Hanle depolarization of the spin signal. Fitting the data with the standard drift-diffusion model of spin injection suggests averaged in-plane spin lifetimes of the order of one nanosecond. Since spin relaxation in two-dimensional systems is anisotropic,

the obtained spin lifetime corresponds to the geometric mean of the spin lifetimes along the two in-plane principal axes. Considering literature values for the spin relaxation times along these directions, the measured lifetimes of about 1 ns are fully consistent with what one would expect for a GaAs-based two-dimensional spin system. In addition, the measurements yielded spin diffusivites D_s, which are orders of magnitude smaller than the charge diffusivity D_e. This finding suggests that electron-electron interactions play an important role in the investigated 2DEG samples. Clearly a more thorough theoretical investigation of spin injection into and transport in 2DEG systems is required to explain the influence of electron-electron interactions on two-dimensional spin systems. Moreover, since the process of spin injection seems to be affected by ballistic tunneling, there is a need to extend the standard spin drift-diffusion model to the (quasi-)ballistic case.

Finally, it was investigated, whether a spin imbalance in n-GaAs can be created via thermal spin injection. So far, thermal spin currents have exclusively been detected by employing three-terminal Hanle experiments. As this technique is controversially discussed, a magneto-optical verification of thermal spin injection would be highly desirable. However, in the present experiments no clear signature of a thermally induced spin accumulation was found, although at least one of the used Fe/n-GaAs samples in principle fulfilled all requirements for the successful generation of a thermal spin current. The measurements suggest that the Seebeck spin tunneling coefficient S_st for Fe/GaAs is orders of magnitude smaller than the reported values for Si and Ge-based systems with oxide tunnel barriers. Recent results by Wagner *et al.* even suggest that in Fe/GaAs heterostructures the electronic contribution to thermal spin injection is completely negligible for experimentally accessible temperature gradients. Nevertheless, since the present experiments suffered from a shunting of the Joule heating current by the Schottky tunnel barrier and the approach of Wagner *et al.* did not take magnon or phonon-assisted tunneling into account, it might be worth to continue the search for thermal spin injection into n-GaAs. These future experiments should be designed in such a way that current shunting can be completely ruled out. One way to achieve this would be to insert a thin insulating layer between the Fe/n-GaAs tunnel barrier and the U-shaped heating contact above. For that purpose a thin film of Al_2O_3 could be used, as it has a quite large thermal conductivity for an insulator. Another way would be to employ laser heating of the ferromagnet as it was already done in previous experiments. However, considering the data situation available today it seems highly unlikely that thermal spin injection from Fe into n-doped bulk GaAs can develop to a serious alternative to conventional electrical spin injection.

For the development of semiconductor-based spintronic devices, such as the Datta-Das spin-FET [16], the realization of efficient electrical spin injection into a two-dimensional electron gas, as investigated in this work, is an important step. A

further step for future experiments now would be the integration of a gate electrode on top of the 2DEG channel, in order to induce Bychkov-Rashba spin precession and thus a signal modulation in a local measurement geometry. In order to achieve this, it is necessary to use materials with a larger spin-orbit coupling than GaAs. In 2009 Koo *et al.* already demonstrated a successful gate voltage controlled spin precession using a high-mobility InAs quantum well with strong intrinsic Bychkov-Rashba-type spin-orbit interaction [125]. However, in these experiments the spin signal was detected in a nonlocal geometry, whereas the spin-FET requires a local detection. Electrical spin injection into a 2DEG confined in an (In,Ga)As-QW has also been demonstrated in Regensburg [127]. Thus, in future the study of electrical spin injection into (In,Ga)As-based heterostructures with an integrated gate electrode should be intensified.

However, it should be mentioned that the cleaved edge detection technique is reaching its limits with (In,Ga)As-based heterostructures. In contrast to bulk GaAs samples or 2DEGs confined at a GaAs/(Al,Ga)As interface, the optical selection rules in a quantum well are expected to yield only weak Kerr rotation signals in edge-emission. Furthermore, the effective magnetic fields arising from Bychkov-Rashba spin-orbit interaction are oriented perpendicular to the direction of the 2DEG channel. Therefore, the measurement geometry of the optical setup prohibits a direct observation of a Bychkov-Rashba-precession of the spin signal, as the sensitive direction of the experiment is parallel to the precession axis of the spin accumulation. Thus, the last steps in the development of a working spin-FET will either have to be investigated with purely electrical means or with a revised magneto-optical detection approach.

Part II.

Anisotropic polar magneto-optic Kerr effect

6. The Fe/GaAs(001) heterostructure

This chapter gives a brief introduction into the crystallographic and magnetic properties of the Fe/GaAs(001) heterostructure. Furthermore, the spin-orbit coupling fields present at the Fe/GaAs interface will be addressed. Throughout the whole chapter special attention is paid to the symmetry of the system.

6.1. Crystal structure

The III-V semiconductor GaAs crystallizes in a zinc-blende structure, i.e. the atoms occupy a face-centered cubic (fcc) lattice with a diatomic basis. The basis contains one As and one Ga atom at the coordinates (0,0,0) and $(\frac{1}{4},\frac{1}{4},\frac{1}{4})$, respectively. This crystal structure has tetrahedral coordination; each atom can be thought to be located in the center of a regular tetrahedron with the four nearest neighbour atoms positioned at the vertex corners [26]. Fig. 6.1 illustrates the top view onto an idealized GaAs(001) surface[1]. Each atom is covalently bound to four atoms of the opposite type, two of them located in the underlying lattice plane and the other two in the overlying lattice plane.

The (001) surface of a GaAs crystal can be Ga- or As-terminated, depending on the atom type in the topmost lattice plane. Since the topmost atoms are lacking two neighbours, with which they could form a covalent bond, there are two unsatisfied bonds per surface atom protruding from the GaAs(001) surface plane. In the case of an As-terminated surface, these dangling bonds are exclusively oriented along the $[1\bar{1}0]$ crystallographic direction (see Fig. 6.1). On a Ga-terminated surface, on the other hand, the dangling bonds are oriented along the [110] direction. Thus, independent on the surface termination, the dangling bonds cause an intrinsic anisotropy at the surface with the $[1\bar{1}0]$ direction being

[1] Note that a GaAs(001) surface forms a plethora of different surface reconstructions, when it is exposed to vacuum or air. This happens in order to minimize the large electronic energy, which arises from the dangling bonds. However, the reconstruction vanishes during the Fe-growth, ideally ending up with the interface shown in Fig. 6.1. An excellent overview concerning this topic is given in Ref. [159].

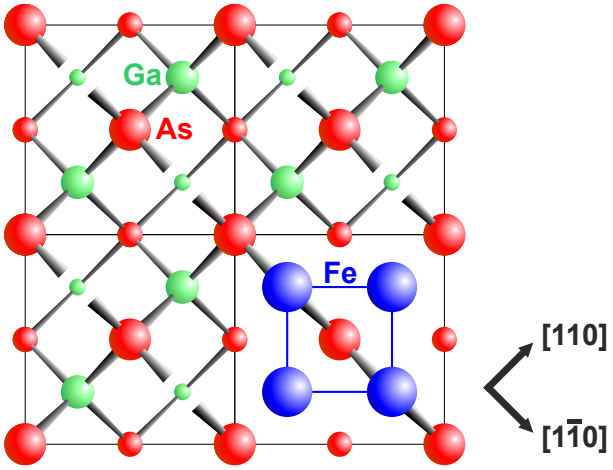

Figure 6.1.: Top view of the As-terminated, unreconstructed GaAs(001) surface. Atoms, which belong to lower atomic layers, are drawn smaller. The As atoms in the topmost layer form dangling bonds along the [1$\bar{1}$0] direction. The lower right part of the figure illustrates, how the first monolayer of Fe grows on the GaAs(001) surface (adapted from [160]).

not equivalent to the perpendicular [110] direction [160]. The resulting symmetry of the GaAs(001) surface can be described with the C_{2v} point group[2], i.e. the surface has a twofold rotation axis perpendicular to the surface and two vertical mirror planes (the (110) and the (1$\bar{1}$0) plane).

Fe has a body-centered cubic (bcc) crystal structure. Since the lattice constant of GaAs ($a_{\mathrm{GaAs}} = 5.653\,\text{Å}$) is roughly twice the lattice constant of Fe ($a_{\mathrm{Fe}} = 2.867\,\text{Å}$) it is possible to epitaxially grow Fe(001) onto GaAs(001). Due to the rather small lattice mismatch of 1.4% the Fe lattice adopts the lattice constant of the underlying GaAs crystal, which results in an almost strain-free, pseudomorphic growth [159]. In the first Fe monolayer every second atom is bound via the (formerly) dangling bonds to the GaAs (see Fig. 6.1 on the lower right). Hence, the GaAs(001) surface transmits its C_{2v} symmetry to the Fe/GaAs(001) interface [43].

6.2. Magnetic properties

Thin Fe films on GaAs(001) exhibit both a cubic magnetocrystalline anisotropy, originating from the bulk symmetry of the material, and a uniaxial magnetocrystalline anisotropy, which stems from the Fe/GaAs(001) interface. In general, the

[2] An introduction to the theory of point groups can be found in Ref. [161].

energy density arising from the in-plane magnetocrystalline anisotropy can be written as [107]:

$$\mathcal{E}(\phi_{\boldsymbol{M}}) = \frac{K_1}{4}\sin^2(2\phi_{\boldsymbol{M}}) + K_\mathrm{u}\cos^2(\phi_{\boldsymbol{M}}), \tag{6.1}$$

where $\phi_{\boldsymbol{M}}$ denotes the angle between the magnetization $\boldsymbol{M}$ and the $[1\bar{1}0]$ direction. The thickness dependent anisotropy constants K_1 and K_u describe the strengths of the fourfold and the twofold anisotropy, respectively. For sufficiently thick Fe films K_1 is found to be negative. This favors two equivalent magnetic easy axes along the in-plane [100] and [010] directions and reflects the magnetocrystalline anisotropy of bulk bcc-Fe.

The K_u-term arises from the reduced symmetry at the Fe/GaAs interface due to the directed orientation of the dangling bonds [162]. Independent of the termination of the GaAs(001) surface or the surface reconstruction prior to the Fe-growth one finds $K_\mathrm{u} > 0$, which favors one easy axis along [110] (see Ref. [163]). For ultrathin Fe films with a thickness of only a few monolayers the uniaxial anisotropy dominates over the fourfold one, leading to a magnetic easy axis along the crystallographic [110] direction [107, 163–168].

6.3. Interfacial spin-orbit coupling fields

An electron, which moves through the electric field of a crystal, experiences this electric field in its rest frame due to Lorentz transformation partly as a magnetic field. The interaction of the electron spin with this effective magnetic field and the associated spin splitting of otherwise degenerate electronic states is known as spin-orbit coupling (SOC). In general, spin-orbit coupling can be modeled with the Hamiltonian [43]

$$H_\mathrm{SOC} = \frac{\hbar}{4m_\mathrm{e}^2c^2}\left(\boldsymbol{\nabla}V \times \boldsymbol{p}\right)\cdot\hat{\boldsymbol{\sigma}}, \tag{6.2}$$

where V is the electrical potential and m_e and $\boldsymbol{p}$ are the electron mass and momentum, respectively. $\hat{\boldsymbol{\sigma}}$ is a vector whose components are the Pauli matrices. The term before the dot can be interpreted as an electron momentum dependent effective magnetic field, which couples to the electron spin. This field is known as spin-orbit (coupling) field (SOF) [43].

Spin-orbit coupling in solids arises from a break of the spatial inversion symmetry. In the Fe/GaAs(001) heterostructure this symmetry is broken due to two reasons. First of all, the Fe/GaAs interface introduces a structure inversion asymmetry. The electric field, which is present at the interface, causes a contribution to the SOC, which is known as Bychkov-Rashba term [80, 81]. Secondly, the GaAs

lacks due to its zinc-blende crystal structure a center of inversion. From this so-called bulk inversion asymmetry follows the Dresselhaus spin-orbit interaction term [73]. At the Fe/GaAs(001) interface both Bychkov-Rashba and Dresselhaus spin-orbit interaction create effective magnetic fields, which lie in the (001) plane. Rewriting Eq. 6.2 in the form $H_{\mathrm{SOC}} \propto \boldsymbol{w}(\boldsymbol{k}) \cdot \hat{\boldsymbol{\sigma}}$, the two types of spin-orbit fields read [43, 169]:

$$\boldsymbol{w}_{\mathrm{BR}}(\boldsymbol{k}) = \alpha \begin{pmatrix} -k_y \\ k_x \\ 0 \end{pmatrix} \qquad \text{and} \qquad \boldsymbol{w}_{\mathrm{D}}(\boldsymbol{k}) = \beta \begin{pmatrix} k_y \\ k_x \\ 0 \end{pmatrix}, \tag{6.3}$$

where α and β denote the Bychkov-Rashba and Dresselhaus spin-orbit parameters, respectively. For this representation of $\boldsymbol{w}_{\mathrm{BR}}(\boldsymbol{k})$ and $\boldsymbol{w}_{\mathrm{D}}(\boldsymbol{k})$ the coordinate system is chosen with $x \| [1\bar{1}0]$, $y \| [110]$ and $z \| [001]$. Fig. 6.2 illustrates the two types of spin-orbit fields in the (001) interface plane. Both the direction and the magnitude of the SOFs depend on the in-plane components $\boldsymbol{k}_{\|}$ of the electron wavevector $\boldsymbol{k}$.

Figure 6.3 illustrates on the left hand side the superposition $\boldsymbol{w}(\boldsymbol{k}) = \boldsymbol{w}_{\mathrm{BR}}(\boldsymbol{k}) + \boldsymbol{w}_{\mathrm{D}}(\boldsymbol{k})$ of Bychkov-Rashba and Dresselhaus spin-orbit fields for $|\alpha/\beta| = 2$. In contrast to the case, where only one kind of SOF is present, the superposition exhibits an anisotropy concerning its magnitude $|\boldsymbol{w}(\boldsymbol{k})|$; for example, electrons, which travel along $(\pm)[110]$, feel a larger SOF than electrons, which move along $(\pm)[1\bar{1}0]$. This anisotropy can be seen in more detail in Fig. 6.3 on the right hand side, where the magnitude

$$|\boldsymbol{w}(\boldsymbol{k})| = k_{\|} \sqrt{\alpha^2 + \beta^2 + 2\alpha\beta \cos(2\phi_{\boldsymbol{k}})} \tag{6.4}$$

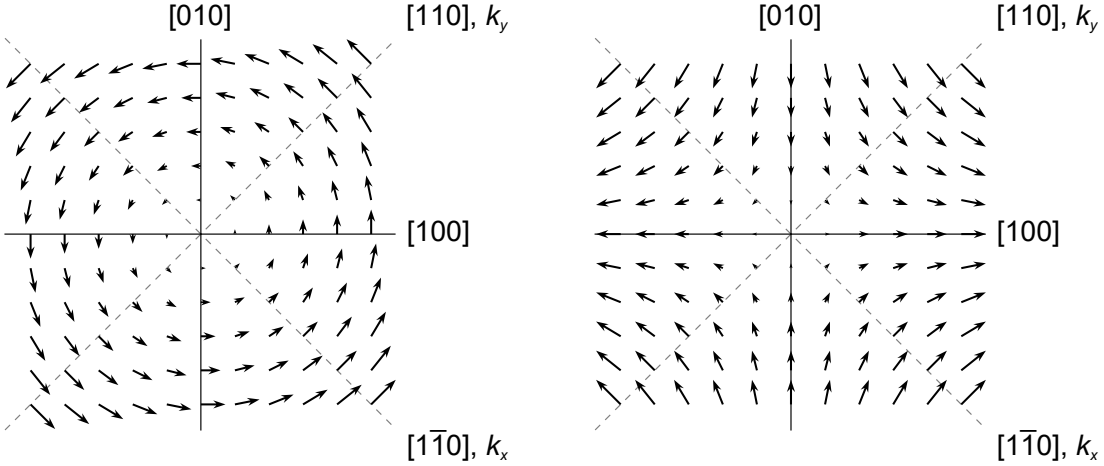

(a) Bychkov-Rashba-SOF (b) Dresselhaus-SOF

Figure 6.2.: Representation of the $\boldsymbol{k}_{\|}$-dependence of the Bychkov-Rashba spin-orbit field $\boldsymbol{w}_{\mathrm{BR}}(\boldsymbol{k})$ (a) and the Dresselhaus spin-orbit field $\boldsymbol{w}_{\mathrm{D}}(\boldsymbol{k})$ (b).

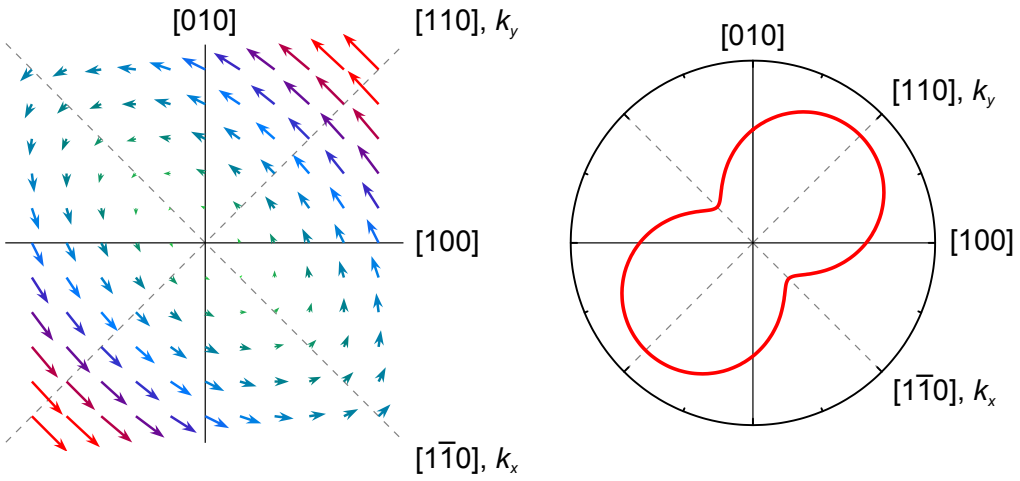

Figure 6.3.: Left: Interfacial spin-orbit fields in the presence of both Bychkov-Rashba and Dresselhaus SOC for $|\alpha/\beta| = 2$. The color of the arrows corresponds to their magnitude. Right: Magnitude $|\boldsymbol{w}(\boldsymbol{k})|$ of the SOFs for a fixed value of $k_{\parallel}$ as a function of the direction of $\boldsymbol{k}_{\parallel}$.

of the SOFs is plotted as a function of $\phi_{\boldsymbol{k}}$ for a fixed value of $k_{\parallel}$. The angle $\phi_{\boldsymbol{k}}$ denotes the direction of the electron $\boldsymbol{k}$-vector with respect to the $[1\bar{1}0]$ direction. All in all, the superposition of both Bychkov-Rashba and Dresselhaus SOFs reflects the symmetry of the Fe/GaAs(001) interface with $|\boldsymbol{w}(\boldsymbol{k})|$ exhibiting its $C_{2\mathrm{v}}$ symmetry.

7. Theory of AP-MOKE

This chapter is dedicated to the polar magneto-optic Kerr effect. It begins with a phenomenological description of the effect and explains the relevant microscopic mechanisms. Special emphasis is put on the important role played by the spin-orbit interaction, without which no Kerr effect would occur. Sec. 7.2 discusses then the anisotropic polar magneto-optic Kerr effect, which can be observed in thin layers of Fe/GaAs(001). First-principles calculations provide a first insight into the basic properties of this effect. Furthermore, a phenomenological model based on simple symmetry considerations is presented, which establishes the connection between the Kerr rotation anisotropy and the interference of interfacial Bychkov-Rashba and Dresselhaus spin-orbit coupling fields.

7.1. Polar magneto-optic Kerr effect

The magneto-optic Kerr effect (MOKE) describes the interaction of electromagnetic waves with a ferromagnetic material. In general, magneto-optic effects may affect the polarization and the intensity of light upon reflection from a ferromagnetic surface. The magneto-optic Kerr effect can be divided into several classes, depending on the orientation of the magnetization $\boldsymbol{M}$ with respect to the propagation direction of the light beam and the sample normal (cf. e.g. Refs. [170–172] for an overview). The present work deals mainly with the polar MOKE (P-MOKE), which is illustrated in Fig. 7.1 on the left hand side. Here, the sample is illuminated with linearly polarized light at (ideally) normal incidence, which makes the Kerr effect exclusively sensitive to the out-of-plane component of the magnetization $\boldsymbol{M}$. When the light is reflected from the surface, it becomes elliptically polarized and its polarization plane is rotated by the angle θ_{K}, the so-called Kerr rotation angle (see Fig. 7.1 on the right hand side). The Kerr ellipticity ε_{K}, which the light obtains, is defined by $\varepsilon_{\mathrm{K}} = \arctan(b/a)$, where a and b denote the lenghts of the semi-major and semi-minor axis of the polarization ellipse, respectively [170].

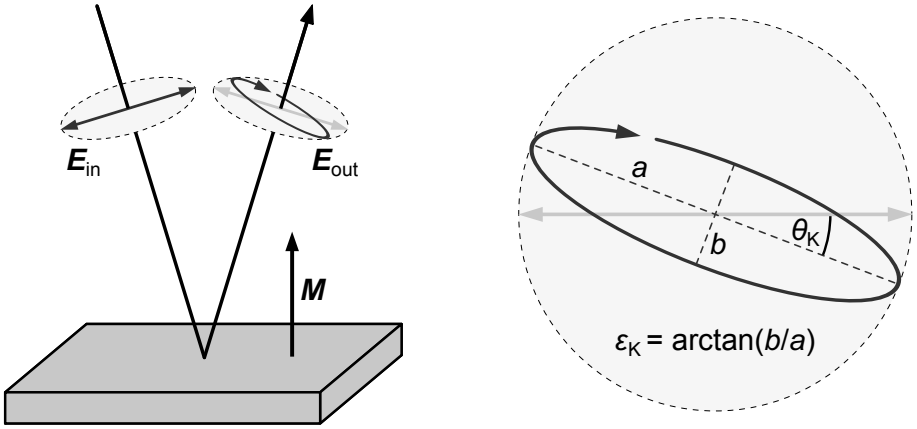

Figure 7.1.: Left: Working principle of the polar magneto-optic Kerr effect: Linearly polarized light is reflected from an out-of-plane magnetized sample. The reflected light is elliptically polarized. Note that the angle of incidence is drawn highly exaggerated; in the experiment it is typically of the order of 1°. Right: The Kerr effect is characterized by the Kerr rotation angle θ_K and the Kerr ellipticity ε_K. θ_K is the angle between the initial polarization direction of the light and the semi-major axis of the ellipse. The ellipticity of the light is defined by $\varepsilon_K = \arctan(b/a)$, where a and b are the lenghts of the semi-major and semi-minor axis, respectively.

7.1.1. Classical description

The origin of the P-MOKE can be understood from a simple classical picture [173], if one considers that linearly polarized light can be decomposed into left circularly polarized (lcp) and right circularly polarized (rcp) light of equal amplitudes. When circularly polarized light propagates through a medium, its electric field causes the electrons within to move on circular trajectories. lcp light forces the electrons into a left circular motion, whereas rcp light drives them onto right circular paths. In a nonmagnetic material the two light modes interact with the medium in an equivalent way. However, in a ferromagnet this symmetry is broken by the magnetization of the sample. The magnetization creates a Lorentz force, which deflects the electrons on their paths. For one rotation direction the Lorentz force points towards the center of the circular motion, whereas in the other case it will point away from it. Due to this asymmetry the electrons exhibit a different response to lcp and rcp light, which gives rise to different indices of refraction for the two circular light modes. This circular birefringence leads to a phase shift and a different absorption of the two circular modes, resulting in the Kerr rotation θ_K and the Kerr ellipticity ε_K, respectively [173].

As it is well known, the effects of charge carriers within a medium are taken into account by the electric displacement $\boldsymbol{D}$, which is connected with the electric field $\boldsymbol{E}$ via $\boldsymbol{D} = \epsilon \boldsymbol{E}$. The dielectric constant ϵ yields the response of a system on

an externally applied electric field $\boldsymbol{E}$. Thus, the optical properties of a medium, which are determined by the motion of its electrons, are fully included in the dielectric constant [173]. In general, ϵ is a second-rank tensor with complex elements. The exact shape of ϵ depends on the symmetry of the investigated system. Before examining the consequences of the $C_{2\mathrm{v}}$ symmetry of the Fe/GaAs interface on ϵ, it is instructive to discuss the case of higher symmetries. Consider a thin film sample in the xy-plane, which has at least a three-fold rotational in-plane symmetry. In the P-MOKE configuration with the magnetization $\boldsymbol{M}$ pointing along the z-direction the dielectric tensor is given by [170]:

$$\epsilon = \begin{pmatrix} \epsilon_{xx} & \epsilon_{xy} & 0 \\ -\epsilon_{xy} & \epsilon_{xx} & 0 \\ 0 & 0 & \epsilon_{zz} \end{pmatrix}. \tag{7.1}$$

This tensor has C_∞ symmetry in the xy-plane, i.e. it is invariant under any rotation about the z-axis [24,174]. Therefore, the optical properties of the system are isotropic as well. This means, in particular, that Kerr rotation θ_K and ellipticity ε_K in P-MOKE measurements do not depend on the polarization direction of the incident light beam with respect to the in-plane directions of the sample.

Kerr rotation θ_K and Kerr ellipticity ε_K are commonly combined to the complex Kerr angle Φ_K. The latter can be expressed in terms of the dielectric tensor as [24, 170]:

$$\Phi_\mathrm{K} = \theta_\mathrm{K} + \mathrm{i}\varepsilon_\mathrm{K} \approx \frac{-\epsilon_{xy}}{(1-\epsilon_{xx})\sqrt{\epsilon_{xx}}}. \tag{7.2}$$

Note that ϵ_{xy} obeys the Onsager relation $\epsilon_{xy}(-\boldsymbol{M}) = -\epsilon_{xy}(\boldsymbol{M})$, whereas ϵ_{xx} and ϵ_{zz} are even functions of $\boldsymbol{M}$ [172, 174]. This shows that the off-diagonal element ϵ_{xy} plays a decisive role for the magneto-optic Kerr effect, since it is only non-zero in the presence of a non-zero magnetization $\boldsymbol{M}$. Moreover, it is the off-diagonal element ϵ_{xy}, which mixes the E_x- and E_y-components of the electric field of the incident light and thus gives rise to the Kerr effect. Hence, the magneto-optical activity of the system is fully determined by ϵ_{xy}.

7.1.2. Quantum-mechanical description

The classical model of the Kerr effect, as described above, assumed that there is an effective magnetic field in the medium, which acts on the electrons in form of a Lorentz force, and thereby rotates the polarization plane of the incident light beam. So, in this simple model, the MOKE is created by the presence of this effective magnetic field only. However, for a quantum-mechanical explanation of magneto-optical effects this field alone is not sufficient. Indeed, also the quantum-mechanical approach considers a mean field; however, in this case it does not affect the motion of the electrons, which determines the optical properties of the

medium; instead it only aligns the spins of the electrons to create a ferromagnetic order. Hence, the mean field only determines the magnetic properties of the sample. The missing link between the magnetic and the optical properties of the solid is given by the spin-orbit interaction, which couples the spin of an electron to its orbital motion. Thus, for a correct, quantum-mechanical description of the Kerr effect both the mean field and the spin-orbit interaction have to be taken into account [175].

For the quantum-mechanical calculation one assumes that the interaction between the electrons of the solid and the electric field of the incident light beam can be treated as a small perturbation, which allows electronic transitions from occupied initial states $|i\rangle$ into unoccupied final states $|f\rangle$ by the absorption of photons from the optical radiation field. Time-dependent perturbation theory yields then an expression for the off-diagonal element $\epsilon_{xy} = \epsilon'_{xy} + \mathrm{i}\epsilon''_{xy}$ [176, 177]:

$$\epsilon'_{xy}(\omega) = \frac{-\pi^2 e^2}{\hbar\omega^2 m_\mathrm{e}^2 V} \sum_{i,f} f(E_i)\left[1 - f(E_f)\right] \Big[\left|\langle f|\, \pi_-\, |i\rangle\right|^2 - \left|\langle f|\, \pi_+\, |i\rangle\right|^2 \Big] \delta(\omega_{fi} - \omega),$$

$$\epsilon''_{xy}(\omega) = \frac{2\pi e^2}{\hbar\omega m_\mathrm{e}^2 V} \sum_{i,f} f(E_i)\left[1 - f(E_f)\right] \left[\frac{\left|\langle f|\, \pi_-\, |i\rangle\right|^2}{\omega_{fi}^2 - \omega^2} - \frac{\left|\langle f|\, \pi_+\, |i\rangle\right|^2}{\omega_{fi}^2 - \omega^2} \right]. \qquad (7.3)$$

Here, ω is the angular frequency of the light, $f(E)$ is the Fermi-Dirac distribution and $\hbar\omega_{fi} = E_f - E_i$ is the energy difference between the states $|f\rangle$ and $|i\rangle$. The terms $\left|\langle f|\, \pi_\pm\, |i\rangle\right|^2$ denote the transition probabilities from the initial state $|i\rangle$ into the final state $|f\rangle$ for absorption of lcp and rcp light, respectively. The equations above show that ϵ_{xy} is proportional to the difference of the absorption probabilities of lcp and rcp light [176, 177], i.e. a magneto-optical effect can only occur for a given frequency ω, if the two circular modes contribute differently to the electronic transitions.

The origin of such different absorption probabilities can be discussed with the aid of Fig. 7.2. Here, one considers the optical transitions from the doubly degenerate $d_{xz,yz}$-levels (quantum numbers $l = 2$, $m_l = \pm 1$) into the p_z-state ($l = 1$, $m_l = 0$) of a ferromagnetic system. Both exchange and spin-orbit interaction lift the degeneracy of the $d_{xz,yz}$-levels: the exchange interaction separates the majority and minority d-levels by the exchange energy ΔE_ex. Furthermore, the spin-orbit interaction splits the d-levels for both spin channels into a $d_{(x+\mathrm{i}y)z}$-state ($m_l = +1$) and a $d_{(x-\mathrm{i}y)z}$ state ($m_l = -1$), separated by the energy ΔE_so [177]. The optical transitions have to obey the dipole selection rules:

$$\Delta l = \pm 1, \qquad \Delta m_l = \pm 1, \qquad (7.4)$$

where $\Delta m_l = +1$ and $\Delta m_l = -1$ correspond to the absorption of lcp and rcp light, respectively. Fig. 7.2 illustrates on the left hand side the allowed optical transitions. Each transition can exclusively couple to one of the two circular

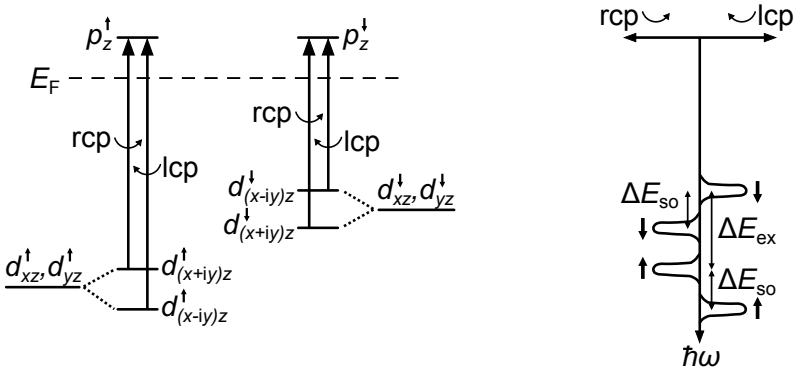

Figure 7.2.: Left: Simplified energy level diagram of a $3d$-ferromagnet. Vertical arrows illustrate the allowed optical transitions for right (rcp) and left circularly polarized (lcp) light (replotted from [177]). Right: Sketch of the corresponding absorption spectra (replotted from [177]).

modes, which results in different absorption spectra for lcp and rcp light (see Fig. 7.2 on the right hand side). These considerations explain the existence of the off-diagonal element ϵ_{xy} of the dielectric tensor and show that both exchange splitting ($\Delta E_{\mathrm{ex}} \neq 0$) and spin-orbit interaction ($\Delta E_{\mathrm{so}} \neq 0$) are essential to observe a magneto-optic Kerr effect [176, 177].

7.2. Anisotropic polar magneto-optic Kerr effect

The present work deals with Fe/GaAs(001) thin film samples, which exhibit a pronounced twofold anisotropy in the xy-plane. In this particular case the dielectric tensor adopts the form [23]:

$$\epsilon = \begin{pmatrix} \epsilon_{xx} & \epsilon_{xy} & 0 \\ -\epsilon_{xy} & \epsilon_{yy} & 0 \\ 0 & 0 & \epsilon_{zz} \end{pmatrix} = \begin{pmatrix} \epsilon_{xx} & \epsilon_{xy} & 0 \\ -\epsilon_{xy} & \epsilon_{xx} + \delta & 0 \\ 0 & 0 & \epsilon_{zz} \end{pmatrix}. \tag{7.5}$$

The intrinsic anisotropy in the xy-plane is expressed by a non-zero $\delta = \epsilon_{yy} - \epsilon_{xx}$, which reduces the C_∞ symmetry of the ϵ-tensor in Eq. 7.1 to a $C_{2\mathrm{v}}$ symmetry. Indeed, a rotation by an angle ϕ about the z-axis transforms the dielectric tensor as [23]:

$$\epsilon(\phi) = \begin{pmatrix} \epsilon_{xx} & \epsilon_{xy} & 0 \\ -\epsilon_{xy} & \epsilon_{xx} & 0 \\ 0 & 0 & \epsilon_{zz} \end{pmatrix} + \frac{\delta}{2} \begin{pmatrix} 1 - \cos(2\phi) & \sin(2\phi) & 0 \\ \sin(2\phi) & 1 + \cos(2\phi) & 0 \\ 0 & 0 & 0 \end{pmatrix}, \tag{7.6}$$

which demonstrates that the parameter δ is responsible for a twofold rotational symmetry of the dielectric tensor. For this reason the optical properties of

Fe/GaAs(001) are expected to reflect the C_{2v} symmetry of the interface, too. In particular, since spin-orbit coupling plays a crucial role for magneto-optic effects, the C_{2v} symmetry of the interfacial SOFs is expected to enter the dielectric tensor and should hence lead to an anisotropic polar magneto-optic Kerr effect (AP-MOKE). This means that the Kerr rotation angle θ_K and Kerr ellipticity ε_K in P-MOKE configuration depend on the angle between the linear polarization of the probing laser beam and the crystallographic axes of the sample, reflecting the twofold symmetry of the interface [23].

7.2.1. First-principles studies

Sebastian Putz from the group of Prof. Dr. J. Fabian investigated the optical properties of a 3 ML Fe/9 ML GaAs(001) heterostructure model system from first-principles by performing density functional theory (DFT) calculations (for details on the DFT calculations see Refs. [23, 24]). The calculations of the dielectric tensor ϵ demonstrate a significant crystallographic optical anisotropy δ, which has its origin in the interfacial SOFs [23]. This anisotropy directly implicates the existence of an anisotropic P-MOKE at the Fe/GaAs interface.

Figure 7.3 shows results from the ab-initio calculations of Putz *et al.* in the visible spectral range. It illustrates on the left hand side the wavelength dependence of the polar Kerr rotation angles for the incident laser beam being polarized along the $[1\bar{1}0]$ and [110] crystallographic directions, respectively. The calculations reveal a clear difference between both polarization directions with the magnitude of the Kerr rotation angle being slightly larger for the [110]-polarization throughout almost the whole visible spectrum [23]. This can be seen in more detail in Fig. 7.3

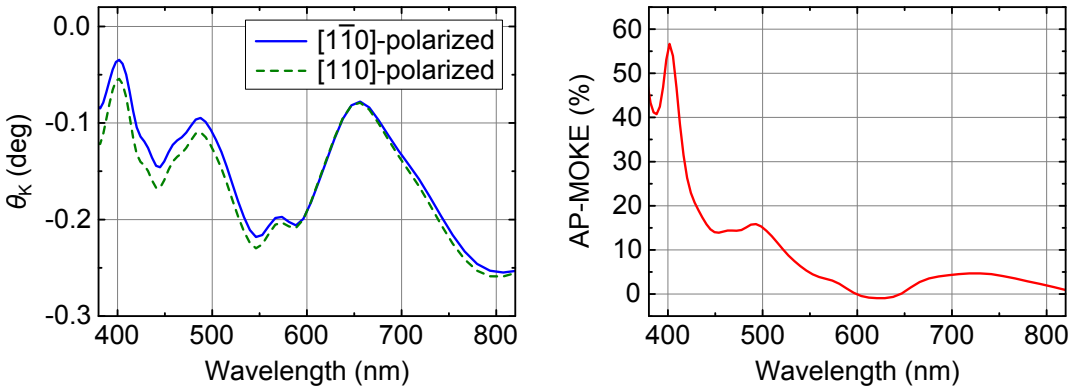

Figure 7.3.: Left: Calculated Kerr rotation angles for the incident laser beam being polarized along the $[1\bar{1}0]$ and [110] crystallographic directions, respectively, as a function of the wavelength (data taken from [23]). Right: Calculated wavelength dependence of AP-MOKE $= \theta_{K,[110]}/\theta_{K,[1\bar{1}0]} - 1$.

on the right hand side, where the quantity AP-MOKE $= \theta_{K,[110]}/\theta_{K,[1\bar{1}0]} - 1$ is plotted. The AP-MOKE exhibits a sharp maximum at a wavelength of 400 nm with an amplitude of more than 50% for the investigated ideal Fe/GaAs interface. The calculations suggest that the AP-MOKE should be easily detectable in the blue and green spectral range, whereas its contributions in the red wavelength range should be much weaker or even negligible.

Figure 7.4 illustrates DFT-calculations of the Kerr rotation angle as a function of the polarization direction of the incident laser beam for a wavelength of 405 nm. The calculation of θ_K clearly shows a dominating twofold symmetry, reflecting the C_{2v} symmetry of the SOC of the underlying Fe/GaAs(001) interface [23].

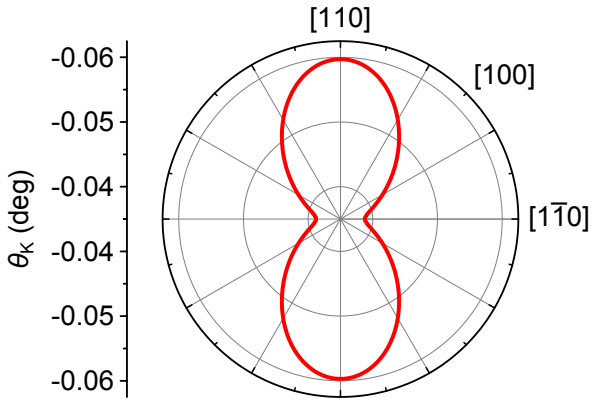

Figure 7.4: Ab-initio calculation of the polar Kerr rotation angle as a function of the linear polarization direction of the incident laser beam for a wavelength of 405 nm. The azimuth indicates the direction of linear polarization with respect to the crystallographic directions of the sample (data taken from [23]).

Note that the calculations assume a perfect, clean interface at $T = 0$ [178]. In contrast, the experiment is performed at room temperature and real samples will always contain structural imperfections. For that reason the experimentally determined values for the Kerr angle and the magnitude of the AP-MOKE will be smaller than predicted by DFT, as will be shown later. However, the numerical calculations can still be considered as a good, qualitative guideline.

7.2.2. Phenomenological model

The first-principles studies of Putz *et al.* have demonstrated that interfacial spin-orbit coupling fields are an essential prerequisite to observe an AP-MOKE [23]. With this knowledge, it is possible to develop a phenomenological model based on rather simple symmetry considerations, to explain the anisotropy of the P-MOKE. Similar models have already been used to describe the crystallographic anisotropy of the tunneling anisotropic magnetoresistance (TAMR) [43, 179, 180] and crystalline anisotropic magnetoresistance (CAMR) [169] on Fe/GaAs(001)-based heterostructures.

The phenomenological model for the present case has been developed by P. Högl from the group of Prof. Dr. J. Fabian [181]. The basic assumption of the model is

that the anisotropy of the Kerr rotation angle θ_K can be obtained by expanding it in powers of products of preferential directions of the system. Since the magnetization $\boldsymbol{M}$ has to be oriented into the out-of-plane direction for the P-MOKE experiments, there remain only two quantities, which define a preferential direction for a given electron wavevector $\boldsymbol{k}$, namely the spin-orbit coupling field

$$\boldsymbol{w}(\boldsymbol{k}) = \begin{pmatrix} (\beta-\alpha)k_y \\ (\beta+\alpha)k_x \\ 0 \end{pmatrix} \tag{7.7}$$

and the polarization direction $\boldsymbol{p}$ of the incident light beam

$$\boldsymbol{p} = \begin{pmatrix} \cos(\phi) \\ \sin(\phi) \\ 0 \end{pmatrix}, \tag{7.8}$$

where the azimuthal angle ϕ is measured with respect to the $[1\bar{1}0]$ axis. Therefore, the expansion of θ_K up to the second order can be written as

$$\begin{aligned}\theta_\mathrm{K}(\boldsymbol{k},\boldsymbol{p}) \approx\ & a_1^{(0)}(\boldsymbol{k}) + a_1^{(1)}(\boldsymbol{k})\left[\boldsymbol{p}\cdot\boldsymbol{w}(\boldsymbol{k})\right] + a_1^{(2)}(\boldsymbol{k})\left|\boldsymbol{w}(\boldsymbol{k})\right|^2 \\ & + a_2^{(2)}(\boldsymbol{k})\left[\boldsymbol{p}\cdot\boldsymbol{w}(\boldsymbol{k})\right]^2 .\end{aligned} \tag{7.9}$$

The expansion coefficients $a_i^{(j)}(\boldsymbol{k})$ are independent of $\boldsymbol{p}$ and $\boldsymbol{w}(\boldsymbol{k})$ and have the cubic symmetry of the underlying bulk materials. Substituting $\boldsymbol{p}$ and $\boldsymbol{w}(\boldsymbol{k})$ into this equation and averaging over all in-plane wavevectors $\boldsymbol{k}_\parallel$ (represented by $\langle\ldots\rangle$) finally yields[1]:

$$\begin{aligned}\theta_\mathrm{K}(\phi) &= \langle\theta_\mathrm{K}(\boldsymbol{k},\boldsymbol{p})\rangle = \\ &= A + \left(\alpha^2+\beta^2\right)\left(B+\frac{C}{2}\right) - C\alpha\beta\cos(2\phi)\end{aligned} \tag{7.10}$$

with the parameters

$$A = \left\langle a_1^{(0)}(\boldsymbol{k})\right\rangle, \tag{7.11}$$

$$B = \left\langle a_1^{(2)}(\boldsymbol{k})k_\parallel^2\right\rangle, \tag{7.12}$$

$$C = \left\langle a_2^{(2)}(\boldsymbol{k})k_\parallel^2\right\rangle. \tag{7.13}$$

The parameter A refers to the Kerr rotation angle in the absence of an interfacial contribution to the spin-orbit coupling, whereas B and C introduce interfacial SOF-mediated modifications to θ_K. In particular, the parameter C is responsible

[1] For the calculation it was made use of $\left\langle a_i^{(j)}(\boldsymbol{k})k_x\right\rangle = \left\langle a_i^{(j)}(\boldsymbol{k})k_y\right\rangle = \left\langle a_i^{(j)}(\boldsymbol{k})k_xk_y\right\rangle = 0$ and $\left\langle a_i^{(j)}(\boldsymbol{k})k_x^2\right\rangle = \left\langle a_i^{(j)}(\boldsymbol{k})k_y^2\right\rangle = \frac{1}{2}\left\langle a_i^{(j)}(\boldsymbol{k})k_\parallel^2\right\rangle$, which is true due to the fourfold symmetry of the $a_i^{(j)}(\boldsymbol{k})$.

for the twofold crystalline anisotropy of the Kerr rotation angle. Note that $\theta_{\mathrm{K}}(\phi)$ compares nicely to the general shape of the Kerr rotation angle anisotropy as obtained from the ab-initio calculations (see Fig. 7.4).

Using Eq. 7.10 one can finally derive an expression for the angular dependence of the AP-MOKE

$$\begin{aligned} \text{AP-MOKE}(\phi) &= \frac{\theta_{\mathrm{K}}(\phi)}{\theta_{\mathrm{K},[1\bar{1}0]}} - 1 \\ &\propto \alpha\beta\left[1 - \cos(2\phi)\right], \end{aligned} \tag{7.14}$$

which is the main result of the phenomenological model. The AP-MOKE is proportional to the product of the Bychkov-Rashba parameter α and the Dresselhaus parameter β. The interference of both types of spin-orbit fields is crucial to obtain the necessary symmetry of the SOFs and thus a $C_{2\mathrm{v}}$ symmetric Kerr rotation anisotropy.

7.2.3. Anisotropic reflectivity

The theoretical predictions of Ref. [23] suggest that not only the Kerr rotation angle θ_{K}, but also the reflectivity R of ultrathin Fe/GaAs(001) films should depend on the angle ϕ between the direction of linear polarization of the incident light and the crystallographic axes of the sample. The reflectivity of the sample is described by the complex reflectivity matrix ρ via [23]

$$\boldsymbol{E}_{\mathrm{r}} = \begin{pmatrix} \rho_{xx} & \rho_{xy} \\ -\rho_{xy} & \rho_{yy} \end{pmatrix} \cdot \boldsymbol{E}_0, \tag{7.15}$$

with $\boldsymbol{E}_0$ and $\boldsymbol{E}_{\mathrm{r}}$ being the polarization states of the incident and reflected light, respectively. Considering a linearly polarized incident laser beam of the form

$$\boldsymbol{E}_0 = E_0 \begin{pmatrix} \cos(\phi) \\ \sin(\phi) \end{pmatrix} \tag{7.16}$$

one finds for the reflected light intensity [181]

$$I(\phi) = I_0 \cdot \left[D + E\cos(2\phi) + F\sin(2\phi)\right] \tag{7.17}$$

with the coefficients

$$D = \tfrac{1}{2}\left(|\rho_{xx}|^2 + |\rho_{yy}|^2\right) + |\rho_{xy}|^2, \tag{7.18}$$

$$E = \tfrac{1}{2}\left(|\rho_{xx}|^2 - |\rho_{yy}|^2\right), \tag{7.19}$$

$$F = \mathrm{Re}\left[\left(\rho_{xx} - \rho_{yy}\right)\bar{\rho}_{xy}\right], \tag{7.20}$$

where an overbar indicates complex conjugation. Assuming real ρ_{ij} matrix elements, it can be shown that in the limit of a vanishing intrinsic anisotropy δ the ratio F/E is of the order of the Kerr rotation angle θ_{K} [181]. Therefore, it is justified to neglect the F coefficient in the analysis of the angular dependence of the reflectivity, as the Kerr rotation angle of ultrathin iron films typically is of the order of 10^{-3} or less, and the reflectivity of the sample can finally be written as

$$R(\phi) \approx D + E\cos(2\phi). \tag{7.21}$$

Thus, similar to the Kerr effect, also the reflectivity of ultrathin Fe/GaAs is expected to depend on the polarization direction of the incident light, again reflecting the $C_{2\mathrm{v}}$ symmetry of the interface.

8. Experimental results

In this chapter the experimental results will be discussed. It is shown that an AP-MOKE can indeed be observed in ultrathin Fe/GaAs(001) at room temperature. The Kerr rotation angle is found to be significantly larger with the laser being polarized along the [110] crystallographic axis, compared to a polarization in the $[1\bar{1}0]$ direction, altogether showing a uniaxial symmetry. The results presented in the following were published in Physical Review Letters **117**, 157202 (2016). Thus, parts of this section directly reproduce Ref. [181].

8.1. Samples

The Fe/GaAs(001) heterostructure system, which is investigated in this work, is sketched in Fig. 8.1 on the left hand side. All layers are grown by molecular beam epitaxy (MBE) on semi-insulating GaAs(001) substrates. The GaAs layers were prepared by Dr. D. Schuh from the group of Prof. Dr. D. Bougeard in a III-V semiconductor MBE system. Here a 100 nm thick buffer layer of undoped GaAs is grown to smoothen the underlying (001)-oriented GaAs substrate prior to the Fe growth. The GaAs is grown with an As-terminated surface, since this assures the formation of an abrupt Fe/GaAs interface (cf. e.g. Refs. [182–185]). Subsequently, the sample is transfered under ultra high vacuum conditions to a connected metal MBE chamber, where the final layers were grown by Dr. M. Kronseder from the group of Prof. Dr. C. H. Back. Fe films of various thicknesses are grown at room temperature. On a first wafer a steplike wedge with 4, 6 and 8 monolayers (ML) of Fe is grown; on a second wafer a 20 ML thick Fe film is deposited. Epitaxial growth and the thickness of the Fe layers are monitored in-situ by recording reflection high-energy electron diffraction (RHEED). Finally, to protect the Fe layers from oxidation they are capped in-situ with a 10 nm thick MgO layer and a 6 nm thick layer of Al_2O_3.

Proper epitaxial growth of the samples was checked via high resolution transmission electron microscopy (HR-TEM) measurements, which were carried out by F. Schwarzhuber from the group of Prof. Dr. J. Zweck. Fig. 8.1 on the right displays as an example a HR-TEM image of an 8 ML Fe/GaAs(001) sample. The image reaches atomic resolution and clearly demonstrates the high crystalline

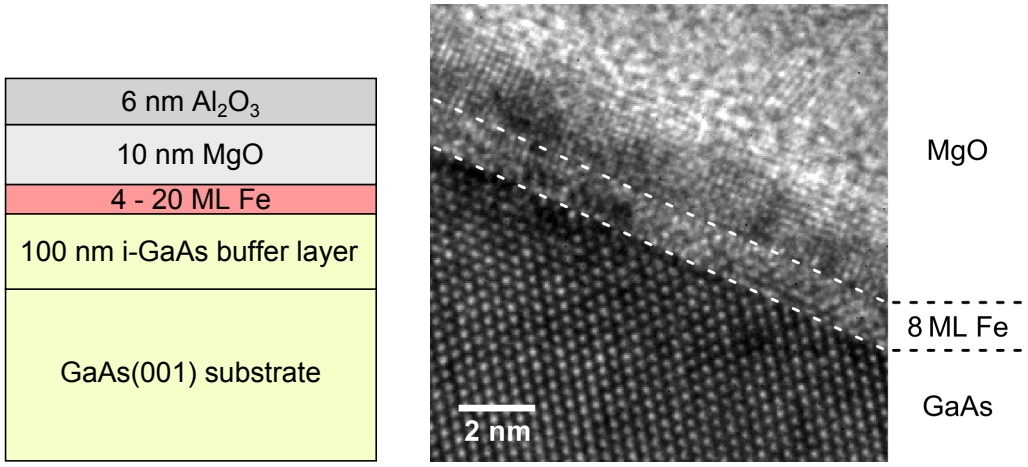

Figure 8.1.: Left: Layer stack of the investigated heterostructures. The Fe films have been grown with thicknesses of 4, 6, 8 and 20 monolayers. Right: HR-TEM image of an 8 ML Fe/GaAs(001) sample. The dashed white lines indicate the positions of the MgO/Fe and Fe/GaAs interfaces.

quality of the GaAs buffer layer. Moreover, an atomically sharp, abrupt interface between the GaAs and the Fe can be observed. The TEM measurements do not directly reveal an epitaxial growth of the Fe. However, since the MgO capping on top of the Fe again shows a crystalline order, it can be assumed that the epitaxial order extends from the GaAs through the Fe film into the MgO layer. The two dashed white lines in the figure indicate the expected thickness of the 8 ML Fe film (≈ 1.147 nm), proving that the Fe has indeed the desired thickness.

8.2. Magnetic characterizations

In order to characterize the magnetic properties of the Fe/GaAs layers, longitudinal MOKE and ferromagnetic resonance (FMR) measurements are performed on full film samples at room temperature. These techniques provide information about the in-plane magnetocrystalline anisotropy. Fig. 8.2 shows longitudinal MOKE loops for 4, 6, 8 and 20 monolayers of Fe/GaAs with the magnetic field applied along the $[1\bar{1}0]$, [100] and [110] crystallographic directions. In all samples one observes a strong uniaxial energy contribution with the easy axis along [110] and the hard axis along $[1\bar{1}0]$. The hard axis loops for the 4, 6 and 8 monolayers samples have more or less a linear shape in between the saturation fields, whereas the 20 ML Fe/GaAs sample has not. The non-linearity in the latter indicates the presence of a fourfold energy term in addition to the uniaxial one (cf. e.g. Refs. [107,163,186]), which will be confirmed below by FMR measurements. Fig. 8.3 shows on the left hand side the angular dependence of the remanent mag-

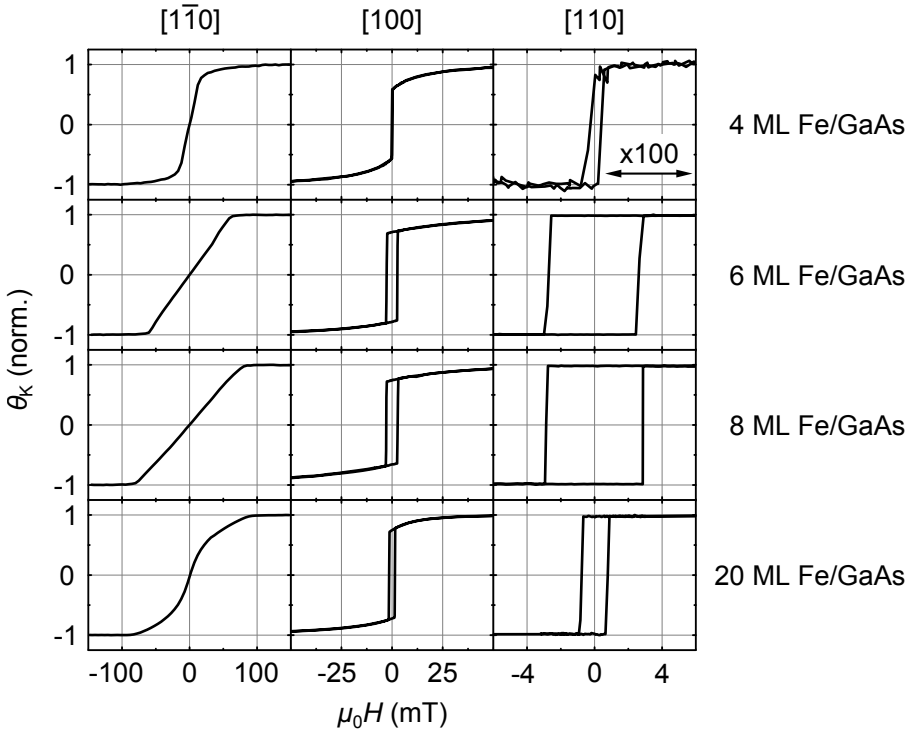

Figure 8.2.: Longitudinal MOKE loops measured on 4, 6, 8 and 20 monolayers of Fe/GaAs with the magnetic field applied along the [1$\bar{1}$0], [100] and [110] crystallographic directions. Note that the field axis of the 4 ML easy axis loop has been stretched by a factor 100.

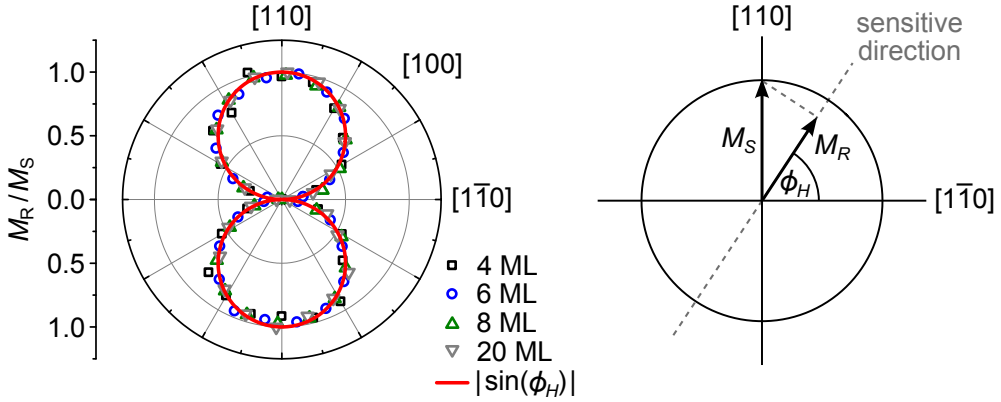

Figure 8.3.: Left: Angular dependence of the remanent magnetization M_R of 4, 6, 8 and 20 monolayers of Fe/GaAs. Right: In remanence the magnetization is aligned along [110] or [$\bar{1}\bar{1}$0] and M_R is given by $|\sin(\phi_{\boldsymbol{H}})|M_\mathrm{S}$.

netization M_R for all Fe layer thicknesses. The measurements reflect the twofold symmetry of the Fe/GaAs interface and are fully consistent with the theoretically expected behaviour of a uniaxial system (see Fig. 8.3 on the right hand side).

Figure 8.4 shows the angular dependence of the in-plane ferromagnetic resonance fields H_{FMR} for all four investigated Fe layer thicknesses determined at room temperature for a microwave frequency of 22 GHz. For all thicknesses the magnetocrystalline anisotropy energy is dominated by a uniaxial energy term, favoring an easy axis along [110]. However, with increasing Fe thickness the fourfold bulk energy contribution becomes more and more important. In particular, for the 20 ML sample maxima of H_{FMR} appear along the $\pm$[110] directions. The anisotropy constants K_1 and K_u (cf. Eq. 6.1) can be extracted from the FMR measurements by numerically fitting the data to the ferromagnetic resonance condition (cf. Ref. [187] for details). The obtained anisotropy constants are plotted in Fig. 8.5 together with some literature values for the Fe/GaAs(001) system. The measured values for K_1 agree nicely with the reported data. In particular, the expected sign reversal of K_1 at $d_{Fe} \approx 6$ ML [107] can be observed for the samples in this work. This sign reversal rotates the easy axes of the fourfold anisotropy for ultrathin films along the in-plane $\langle 110 \rangle$ directions, in contrast to thicker Fe films, where the fourfold easy axes are oriented along $\langle 100 \rangle$ [107]. For larger Fe film thicknesses the data scale linearly with $1/d_{Fe}$, which suggests the presence of an interfacial contribution, which decreases K_1 with respect to the bulk Fe value of $K_1 \approx -40\,\mathrm{kJ/m^3}$.

The uniaxial anisotropy constant K_u is of purely interfacial origin, which can be seen from the facts that $K_u \propto 1/d_{Fe}$ for $d_{Fe} \geq 10$ ML and that K_u vanishes for $1/d_{Fe} \to 0$. The accordance of the measured K_u data with the literature values is less well pronounced compared to the measurements of K_1. The obtained K_u values of the 4, 6 and 8 ML samples are significantly smaller than the reported data from R. Moosbühler [159] and M. Brockmann [188]; on the other hand, the data are in quite fair agreement with the measurements of M. Zölfl [189]. R. Moosbühler argued that the observed difference of the uniaxial anisotropy constants of Refs. [159, 188, 189] can be explained with a different pretreatment of the GaAs substrates prior to the Fe growth [159]. Moreover, for very thin Fe films the Curie temperature is significantly reduced with respect to the value of bulk Fe (cf. e.g. Refs. [190, 191]). Thus, the system is more susceptible to thermal excitations, which reduce the anisotropy. According to Ref. [159] K_u is fully developed only for Fe thicknesses above ≈ 10 ML. However, for all samples in this work the uniaxial anisotropy is much larger than the fourfold one, in accordance with the twofold symmetry of the Fe/GaAs(001) interface.

Altogether, the magnetic characterizations confirm that the samples have a high quality Fe/GaAs(001) interface, as the magnetic properties show the same C_{2v} symmetry as the interfacial spin-orbit fields do.

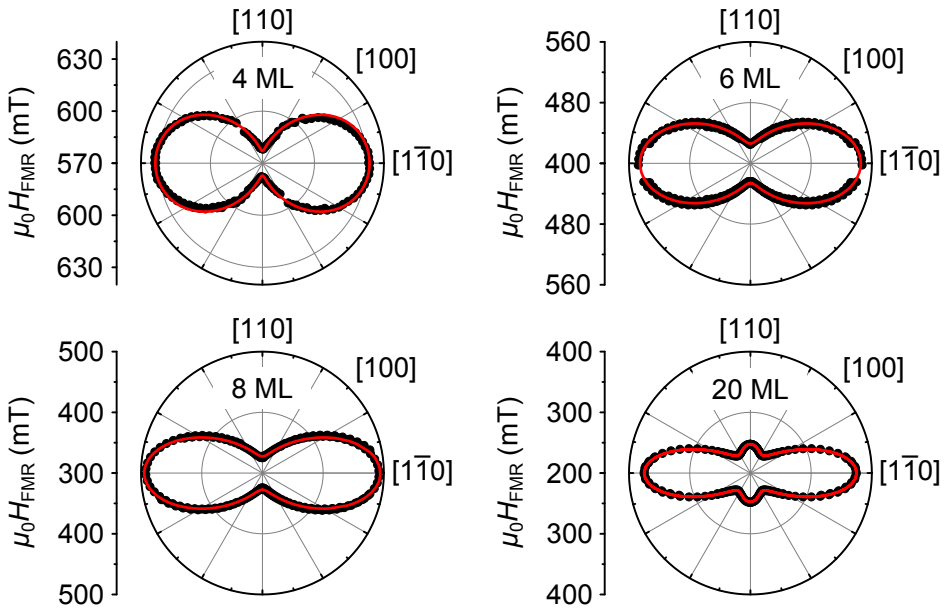

Figure 8.4.: In-plane angular dependence of the resonance field determined from FMR measurements at 22 GHz for 4, 6, 8 and 20 monolayers of Fe/GaAs. The magnetocrystalline anisotropy energy is dominated by a uniaxial energy term, favoring a magnetic easy axis along [110]. For 20 ML Fe the bulk cubic energy contribution becomes visible. The red lines are numerical fits.

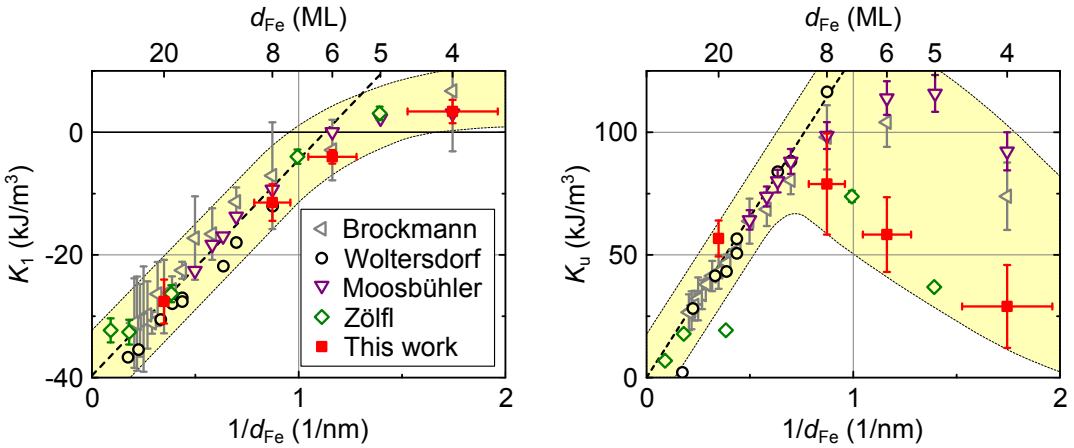

Figure 8.5.: Anisotropy constants K_1 (left) and K_u (right) as a function of the inverse iron layer thickness. The additional data points are taken from the PhD theses of M. Brockmann [188], G. Woltersdorf [187], R. Moosbühler [159] and M. Zölfl [189]. The black dashed line is a linear fit to the data points with $d_{Fe} \geq 10$ ML. The yellow area is a guide-to-the-eye to visualize the general trend of the data.

8.3. P-MOKE measurements

8.3.1. Setup

The polar magneto-optic Kerr effect measurements are carried out at room temperature using the setup shown in Fig. 8.6. A diode laser with a wavelength of 405 nm is used as light source. This wavelength is chosen according to the DFT-calculations of Ref. [23], as the theoretical considerations suggest a strong AP-MOKE for this particular photon energy (see also Fig. 7.3). The light is linearly polarized by polarizer P_1 and guided to the sample via the two mirrors M_1 and M_2. The sample is mounted on a special sample holder, which enables a rotation of the sample about its [001] crystallographic direction, which is parallel to the magnetic field and the direction of the incident laser beam. Therefore, it is possible to vary the angle between the in-plane crystallographic directions of the sample and the fixed linear polarization direction of the incident laser beam. Here, it is extremely important to ensure that the sample is properly mounted on the sample holder and that the laser hits the sample perfectly at normal incidence. Even a small misalignment between the sample normal, the rotation axis and the direction of the incident laser beam causes a deviation of the back reflected beam from the desired optical path by several degrees as soon as the sample is rotated. Such deviations can lead to spurious signal signatures in the angle dependent measurements and thus have to be avoided.

Due to P-MOKE the reflected light undergoes a change of its linear polarization to a rotated, elliptical polarization state, characterized by the Kerr rotation angle θ_K and Kerr ellipticity ε_K. Two different measurement schemes are used for the detection of the Kerr effect (see Fig. 8.6). The first one uses a Wollaston prism (WP) which splits the light into two orthogonally polarized beams whose intensities I_1 and I_2 are measured with a balanced photodiode detector. The detector transmits both the sum $\Sigma(\theta_K, \varepsilon_K) = I_1 + I_2$ and the difference signal $\Delta(\theta_K, \varepsilon_K) = I_1 - I_2$ of the two single photodiodes. A theoretical analysis of the system using Stokes vectors and Müller matrices shows that $\Sigma(\theta_K, \varepsilon_K) = I_0$ and $\Delta(\theta_K, \varepsilon_K) = I_0 \sin(2\theta_K)\cos(2\varepsilon_K)$, where I_0 is the light intensity right at the sample position (see appendix B for details). Hence, using small-angle approximation, one finds the following expression for the Kerr rotation angle:

$$\theta_K \approx \frac{\Delta(\theta_K, \varepsilon_K)}{2\Sigma(\theta_K, \varepsilon_K)}. \tag{8.1}$$

Therefore, the Wollaston-detector (WD) method yields absolute values for the Kerr rotation angle and separates any signal contributions originating from the Kerr ellipticity.

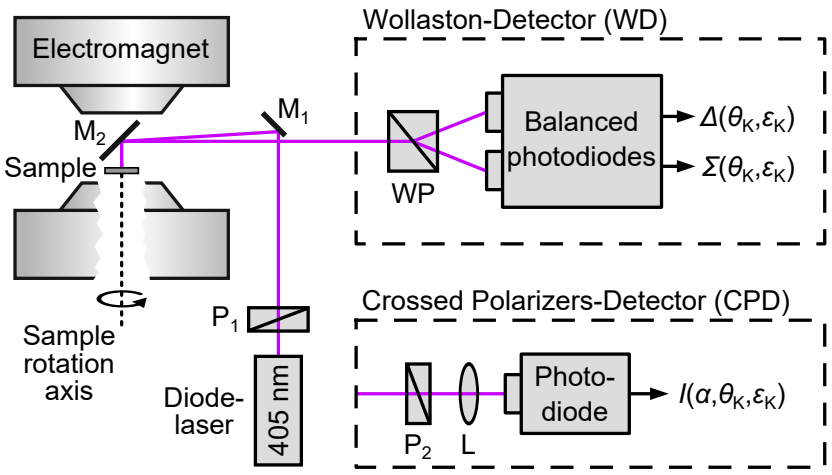

Figure 8.6.: Sketch of the polar MOKE setup. The sample is mounted on a rotatable sample holder within the field of an electromagnet. The Kerr signal of the sample can be measured via a Wollaston-detector (WD) unit or via a crossed polarizers-detector (CPD).

The second measurement method used in the experiment utilizes a crossed polarizers detection (CPD) scheme. Here, a second linear polarizer P_2 is used to probe the polarization state of the reflected, Kerr rotated light. The optical axis of P_2 deviates slightly from the perfectly crossed state. The transmitted light is focused with the aid of lens L onto a single photodiode, which detects the light intensity $I(\alpha, \theta_K, \varepsilon_K)$, where α is the angle of P_2 with respect to the perfectly crossed state. A theoretical analysis of the setup shows that I is given by (see appendix B)

$$I(\alpha, \theta_K, \varepsilon_K) = \frac{I_0}{2} \cdot \Big[1 - \cos\Big(2(\alpha - \theta_K)\Big) \cos(2\varepsilon_K)\Big]. \tag{8.2}$$

Hence, in contrast to the WD method, the CPD mixes the θ_K and ε_K signal contributions. However, it can be shown that the Kerr rotation angle is directly proportional to the intensity difference between positive and negative applied magnetic field, $\Delta I = |I(+\boldsymbol{H}) - I(-\boldsymbol{H})|$, resulting in

$$\theta_K \approx \frac{\Delta I}{2 I_0 \sin(2\alpha)}. \tag{8.3}$$

CPD does not allow to directly determine I_0 and the angle α is in general an ill-defined quantity. Thus, unlike WD, CPD gives only a relative measure for the Kerr rotation signal θ_K. However, the advantage of CPD compared to WD is its better signal-to-noise ratio due to its simpler optical and electrical layout.

8.3.2. Anisotropic reflectivity

Before discussing the results of the P-MOKE experiments, the expected anisotropy of the sample reflectivity (see Sec. 7.2.3) will be briefly addressed. Fig. 8.7 shows polarization angle dependent measurements of the reflectivity of a 4 ML Fe/GaAs sample, with the magnetization pointing along several crystallographic directions. For these measurements the laser light is guided under normal incidence onto the sample and the reflected light intensity is measured using a photodiode. To rotate the direction of linear polarization of the incident laser beam with respect to the crystallographic axes of the sample without changing the incident laser intensity the sample and the magnetic field are simultaneously rotated around the surface normal. Fig. 8.7(a) shows the measured reflectivities with the magnetization along the [110] direction normalized to the reflectivity for a linear polarization along the [110] direction. The reflectivity of the sample shows a clear twofold dependence on the polarization direction of the light with maxima (minima) along the $[1\bar{1}0]$ ($[110]$) direction. This symmetry again reflects the underlying C_{2v} symmetry of the Fe/GaAs interface. While a C_{2v} symmetry in the reflectivity is also expected when the magnetization points along the $[1\bar{1}0]$ or [001] directions, no significant anisotropy is observed in these cases, as shown in Figs. 8.7(b) and (c). Apparently the anisotropy is below the detection limit for these cases.

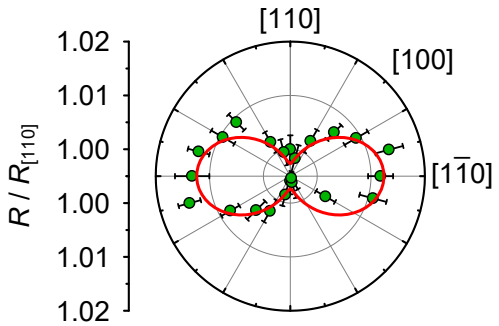

(a) $\boldsymbol{M} \,||\, [110]$

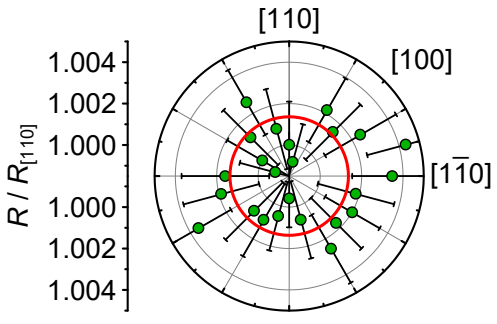

(b) $\boldsymbol{M} \,||\, [1\bar{1}0]$

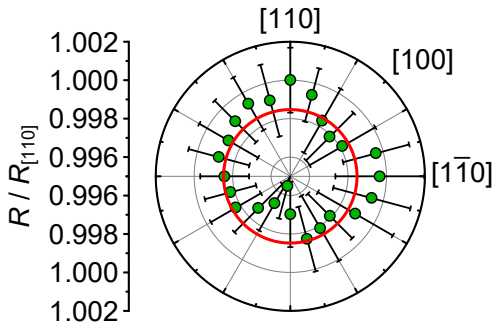

(c) $\boldsymbol{M} \,||\, [001]$

Figure 8.7.: Reflectivity of 4 ML Fe/GaAs for different polarization directions of the incident laser beam with $\boldsymbol{M}$ being saturated along the [110] (a), the $[1\bar{1}0]$ (b) and the [001] direction (c). The solid line in (a) is a fit using Eq. 7.21. Solid lines in (b) and (c) correspond to the average values of the data sets.

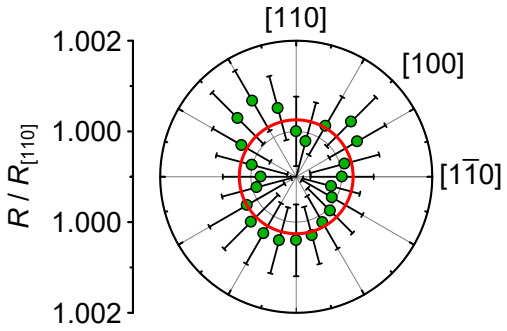

Figure 8.8: Reflectivity of 20 ML Fe/GaAs for different polarization directions of the incident laser beam with the magnetization being saturated along the [110] direction. The symbols are experimental data. The solid line is the average value of the data set.

Figure 8.8 illustrates a polarization angle dependent measurement of the reflectivity of a 20 ML Fe/GaAs sample with the magnetization along the [110] direction. For samples in this thickness range the reflectivity clearly shows an isotropic behaviour, which underlines the interfacial character of the observations.

As a final note, the consequences of a possible linear dichroism of the substrate on the AP-MOKE measurements will be addressed. Linear dichroism describes the dependence of the absorption coefficient of a sample on the direction of the linear polarization of the incident light beam. Since P-MOKE experiments rely on the measurement of reflected light intensities, a combination of the Kerr effect of a ferromagnetic film and a substrate with linear dichroism may give the impression that the Kerr angle depends on the polarization direction even if this is not the case. This effect is of particular importance for ultrathin film samples, since a few monolayers of a material are semi-transparent, i.e. the probing light beam can easily penetrate into the substrate. However, this effect is negligible for the present GaAs(001) substrate because GaAs crystallizes in a cubic lattice and therefore it is to first order optically isotropic [192]. Indeed, it has been shown that even cubic systems can exhibit a small intrinsic birefringence for short wavelengths [193]; however, the authors of Ref. [193] also show that there is no birefringence for light propagation along the [001] crystallographic direction, which corresponds to the situation in the present P-MOKE experiments. Hence, linear dichroism originating from the bulk GaAs substrate is not expected to affect the AP-MOKE experiments. Any anisotropic optical properties therefore have to stem from the Fe/GaAs interface. Moreover, since the polarization angle dependent reflectivity measurements presented above do not show any significant anisotropy for $\boldsymbol{M} \,||\, [001]$, linear dichroism can generally be excluded as a possible source for the C_{2v} symmetry in AP-MOKE, as discussed in the following section.

8.3.3. Anisotropic polar magneto-optic Kerr effect

The out-of-plane P-MOKE loops of the four investigated Fe/GaAs samples, measured with the Wollaston-detector, are displayed in Fig. 8.9. For the AP-MOKE

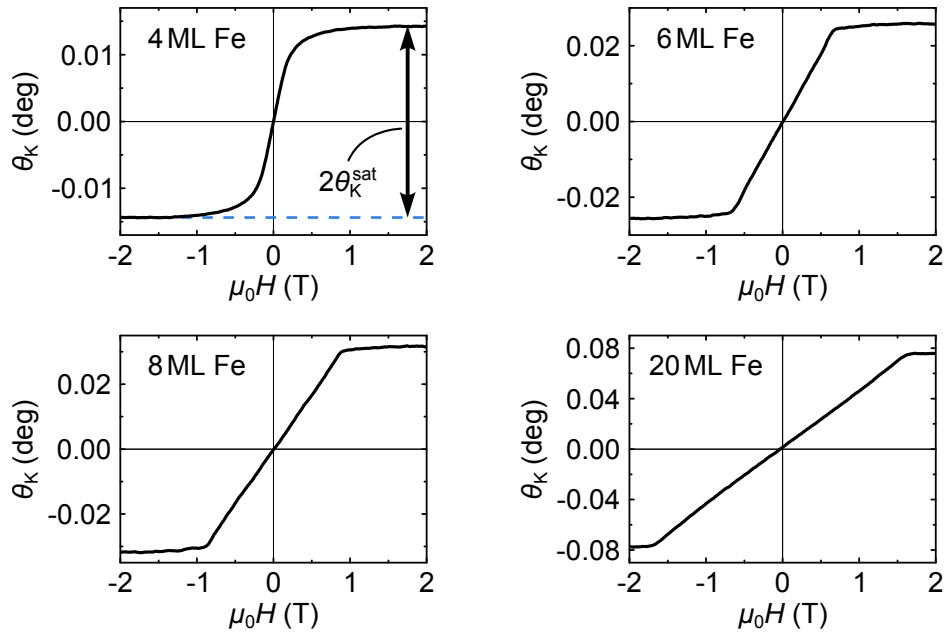

Figure 8.9.: P-MOKE loops of 4, 6, 8 and 20 monolayers of Fe/GaAs measured with the Wollaston-detector. The height of the loops in saturation, $2\theta_K^{sat}$, is used as a measure for the strength of the polar MOKE.

measurements the height of the magnetization loops in saturation, $2\theta_K^{sat}$, is used as a measure for the strength of the polar magneto-optic Kerr effect. In the 4 ML case, for instance, the sample exhibits a maximum Kerr rotation of $\theta_K^{sat} \approx 0.0145°$ in saturation. The Fe layer thickness dependence of θ_K^{sat} is illustrated in Fig. 8.10 on the left. As the penetration depth of the laser lies well above the thickness of the investigated Fe layers[1], the Kerr rotation shows a linear increase with film thickness.

The measurement procedure for the AP-MOKE experiments is as follows: first a fixed polarization direction with respect to the crystallographic directions of the sample is chosen. Then the sample is saturated alternating with positive and negative magnetic fields. For each saturated state the Kerr rotation is continuously measured for ~ 1 min. These measurements at alternating saturations are repeated several times to increase statistics and to check whether there is a significant drift with time. Finally, the difference of the detected Kerr rotations for positive and negative saturation fields is evaluated to extract a value for θ_K^{sat}. By using this fast magnetization reversal procedure one can avoid drift effects which might appear during the measurement of full magnetization loops. Finally, the sample is rotated to a new polarization direction and the measurement procedure is repeated for this new direction.

[1]The penetration depth into bulk Fe can be determined with the optical constants reported in Ref. [194]. For a wavelength of 405 nm the penetration depth is roughly 86 ML.

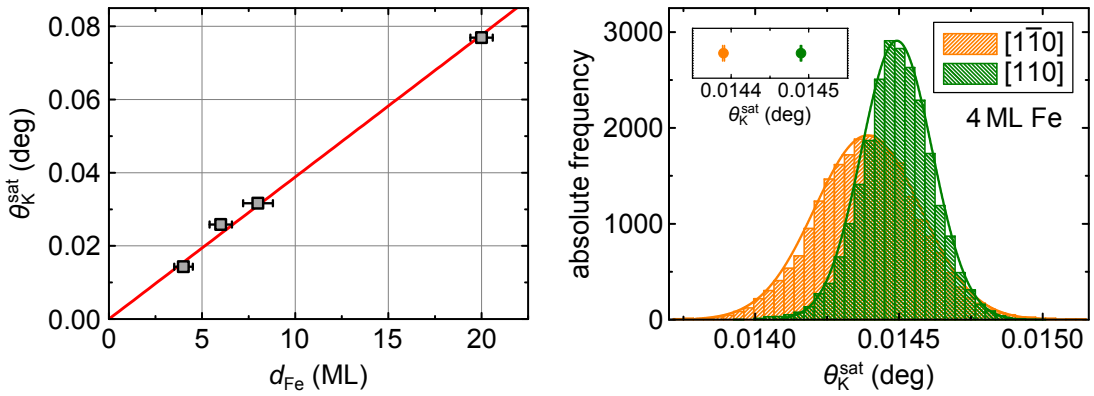

Figure 8.10.: Left: Kerr rotation angle θ_K^{sat} as a function of Fe layer thickness d_{Fe}. The solid line is a linear fit. Right: Histograms of the Kerr rotation angles θ_K^{sat} for the laser being polarized along the [110] and [1$\bar{1}$0] crystallographic directions for 4 ML Fe/GaAs. The inset shows the mean values for both polarization directions with the corresponding error bars.

Figure 8.10 displays on the right hand side histograms of repeated independent measurements of the absolute value of the Kerr rotation angles θ_K^{sat} on the 4 ML Fe/GaAs sample with the incident laser beam being polarized along the [110] and [1$\bar{1}$0] crystallographic directions, respectively, measured with Wollaston-detection. The statistical analysis reveals a clear difference between both polarization directions (see inset of Fig. 8.10 on the right) with the Kerr rotation angle θ_K^{sat} in [110] direction being $\approx 0.7\%$ larger than in the [1$\bar{1}$0] direction.

Figures 8.11(a)-(c) show the anisotropy of the Kerr rotation angle θ_K^{sat} for 4, 6 and 8 monolayers Fe/GaAs measured with the crossed polarizers-detector while rotating the sample about the direction of the incident laser beam and keeping both the incident light intensity I_0 and the tilt angle α of the analyzer P_2 fixed. The azimuthal angle ϕ in the plots indicates the direction of the linear polarization of the incident laser beam with respect to the crystallographic axes of the samples. The data are normalized to the value taken along the hard magnetic direction, [1$\bar{1}$0]. In all three cases the measurements reveal a clear twofold symmetry of the Kerr rotation angle with maxima (minima) along the [110] ([1$\bar{1}$0]) directions, the principal axes of the interfacial spin-orbit coupling fields. Note that the amplitude of the signal decreases with increasing Fe film thickness indicating its interfacial origin.

The experimentally measured twofold symmetry of the Kerr rotation angle suggests that the effect originates from the SOFs present at the Fe/GaAs interface. They exhibit the same twofold symmetry which stems from the combination of Dresselhaus and Bychkov-Rashba spin-orbit interaction arising from bulk inversion asymmetry of the GaAs and structure inversion asymmetry of the Fe/GaAs interface, respectively. Indeed, the data of Figs. 8.11(a)-(c) can be well fitted

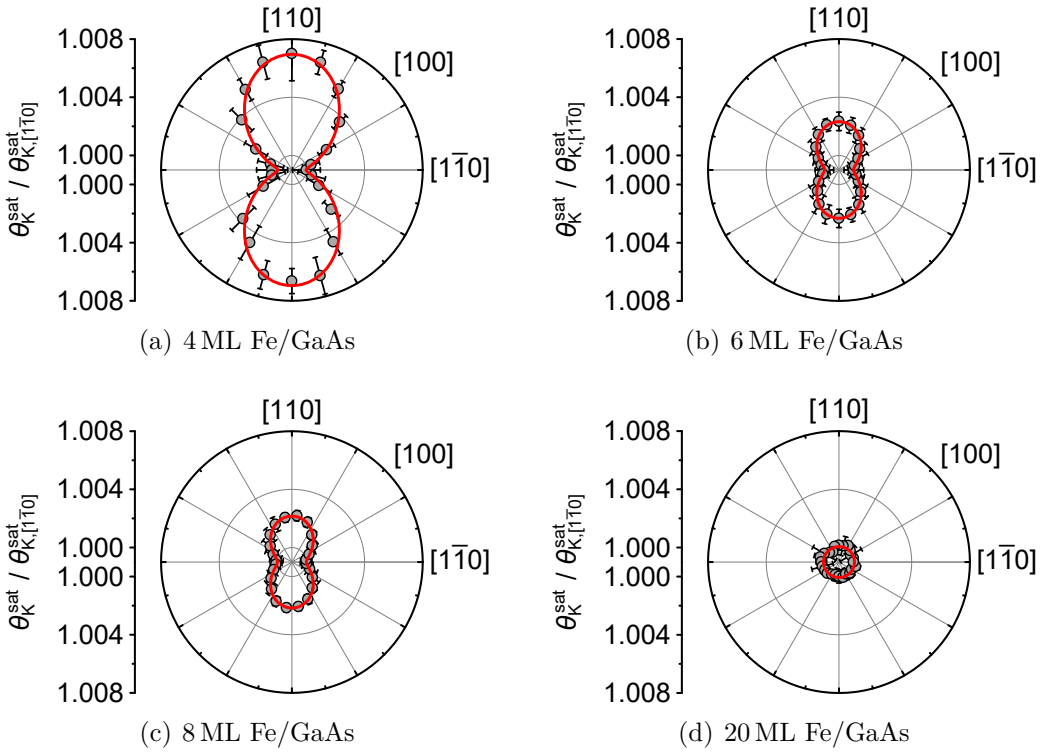

(a) 4 ML Fe/GaAs (b) 6 ML Fe/GaAs

(c) 8 ML Fe/GaAs (d) 20 ML Fe/GaAs

Figure 8.11.: Maximum Kerr rotation θ_K^{sat} normalized to the Kerr rotation along the [1$\bar{1}$0] direction for different polarization directions of the incident laser beam for 4, 6, 8 and 20 monolayers Fe/GaAs. The symbols are experimental data. In (a)-(c) the solid lines are fits using the phenomenological model, Eq. 7.14. The solid line in (d) represents the average value of the data points.

using the phenomenological model for the AP-MOKE (see Sec. 7.2.2).

To rule out any systematic errors from the setup as possible origin for the measured twofold symmetry, additionally polarization angle dependent measurements are performed on a single crystalline 20 ML thick Fe/GaAs sample and a polycrystalline 100 nm thick permalloy (Py) film grown onto oxidized GaAs. These measurements are carried out in an analogous way like the measurements of Figs. 8.11(a)-(c) and are shown in Figs. 8.11(d) and 8.12(a). In neither of these control experiments a clear twofold behaviour of θ_K^{sat} is observed. In the 20 ML Fe/GaAs sample the AP-MOKE is - due to its interface character - too weak to be detected and in Py it should be completely absent due to the polycrystallinity of the sample. Moreover, a vanishing Kerr rotation anisotropy is also found for symmetrically grown, single crystalline MgO/6 ML Fe/MgO and Au/6 ML Fe/Au samples (see Figs. 8.12(b) and (c)), both lacking interfacial C_{2v} symmetry of the SOC. This confirms that the interference of both Bychkov-Rashba and Dresselhaus SOC in the system is crucial to obtain an AP-MOKE because it ensures the necessary symmetry of the SOFs. In systems where at least one of

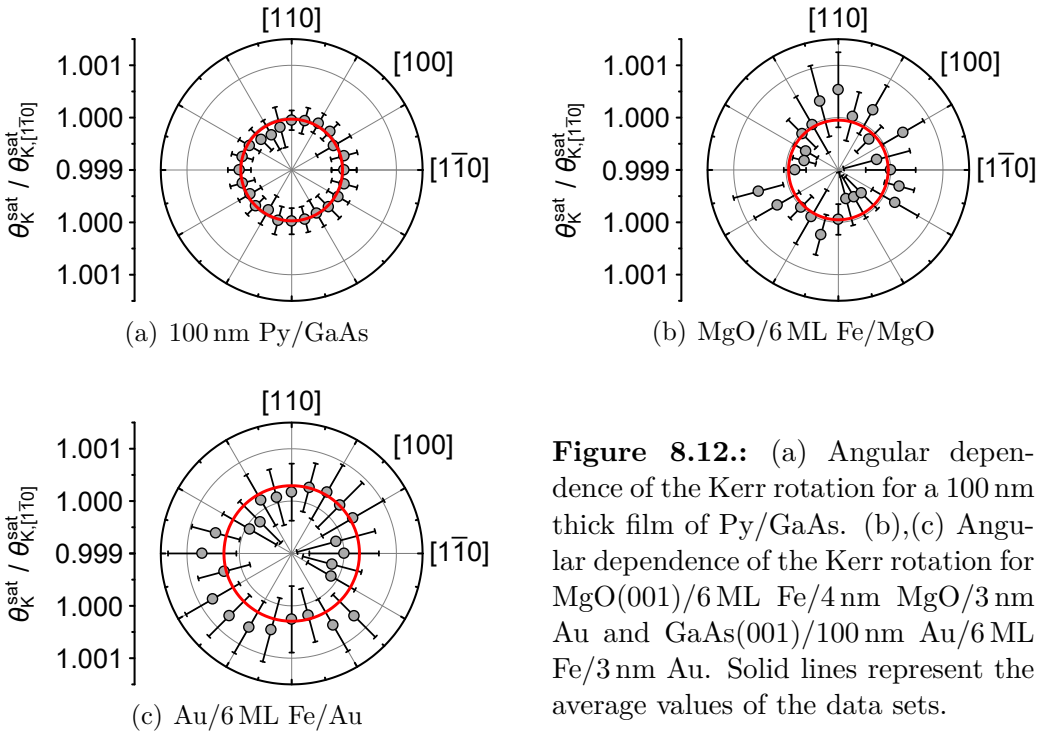

(a) 100 nm Py/GaAs

(b) MgO/6 ML Fe/MgO

(c) Au/6 ML Fe/Au

Figure 8.12.: (a) Angular dependence of the Kerr rotation for a 100 nm thick film of Py/GaAs. (b),(c) Angular dependence of the Kerr rotation for MgO(001)/6 ML Fe/4 nm MgO/3 nm Au and GaAs(001)/100 nm Au/6 ML Fe/3 nm Au. Solid lines represent the average values of the data sets.

the two spin-orbit fields is missing the AP-MOKE is zero. Therefore, the observations of Figs. 8.10 on the right hand side and 8.11(a)-(c) can be linked to the anisotropic polar magneto-optic Kerr effect originating from the interfacial SOC at the Fe/GaAs interface [23].

The observed anisotropy of the Kerr rotation angle for the ultrathin Fe layers compares nicely to ab-initio calculations based on a 3 ML Fe/9 ML GaAs(001) model system [23]. The theoretical considerations reveal a pronounced uniaxial behaviour of $\theta_{\mathrm{K}}^{\mathrm{sat}}$ with strong anisotropies in the ultra-violet and violet wavelength range. However, as the DFT calculations assume an ideal Fe/GaAs interface at $T = 0$, they suggest Kerr rotation anisotropies of the order of $\approx 50\%$ for a wavelength of 405 nm (see Sec. 7.2.1), in contrast to the actually measured anisotropies, which lie well below 1% at room temperature. Note that such large discrepancies between ab-initio theory and experiment are not unusual and have already been observed previously. In general, spin-orbit related effects become weaker with increasing temperature. For example, the TAMR ratio of Fe/GaAs/Au tunnel junctions, which was shown to be of the order of some tenths of a percent at 4.2 K [179, 195], linearly decreases with increasing temperature and even vanishes for certain bias conditions at room temperature [196]. Moreover, first-principles calculations suggest for Fe-based tunnel junctions a large TAMR of up to 35% [197, 198], which is two orders of magnitude larger than experimentally observed. So, just like in the case of TAMR, a combination of elevated temperatures and enhanced ab-initio values due to the assumption of

perfect interfaces can easily accumulate to the observed two orders of magnitude difference between experiment and theory.

Recently, lateral magnetotransport measurements on identically prepared, epitaxial 4, 6 and 8 monolayers thick Fe/GaAs(001) have revealed a robust magnetoresistance anisotropy depending on the direction of the current flow with respect to the crystallographic directions of the sample [169]. Just like in the present case of AP-MOKE these transport anisotropies have been explained by the presence of interfacial Bychkov-Rashba and Dresselhaus SOFs. However, note that the optical measurements include all optical transitions at a photon energy of 3 eV available in the Brillouin zone, whereas the lateral magnetotransport experiment of Ref. [169] only involves electrons right at the Fermi edge. The optical experiment averages over a wider spectral regime and therefore provides a complementary information.

Finally, the wavelength dependence of the AP-MOKE shall be briefly addressed. The first-principles studies of Putz *et al.* demonstrate a pronounced photon energy dependence of the AP-MOKE (see Ref. [23] and Sec. 7.2.1). A strong Kerr rotation anisotropy is expected at a wavelength of 405 nm; in contrast, for light in the red spectral range only a small AP-MOKE is predicted (see Fig. 7.3). The latter is experimentally verified by using a diode laser with a wavelength of 635 nm, where the theoretical considerations suggest a nearby zero crossing of the AP-MOKE. In contrast to the experiments described above, where a light source with 405 nm is used, the measurements with 635 nm do not show any robust signal contributions, which could unequivocally be linked to AP-MOKE (see Fig. 8.13). Therefore, the measurements at 405 nm and 635 nm are in qualitative agreement with the predictions of Putz *et al.* [23].

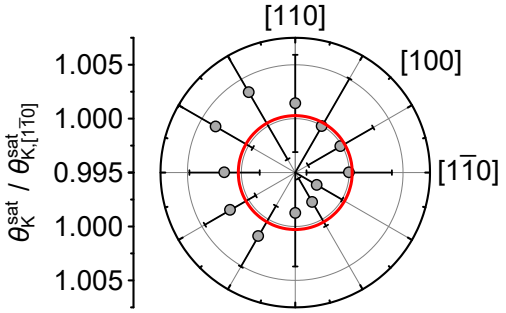

Figure 8.13: Kerr rotation angle for different polarization directions of the incident laser beam for a 4 ML Fe/GaAs sample measured at a laser wavelength of 635 nm. The solid line is the average of the data points.

9. Summary and outlook

The aim of this work was to investigate the optical properties of ultrathin layers of epitaxial Fe/GaAs(001) at room temperature. It was demonstrated that spin-orbit coupling at the Fe/GaAs(001) interface not only affects the transport properties of the heterostructure, as was shown before [169, 179], but also gives rise to magneto-optical anisotropies. A clear twofold symmetry of the Kerr rotation angle θ_{K} depending on the orientation of the linear polarization of the probing laser beam with respect to the crystallographic directions of the sample was detected in samples with 4, 6 and 8 monolayers thick Fe films. In all these samples the Kerr rotation is found to be larger with the incident laser beam being polarized along the [110] crystallographic direction, compared to a polarization along $[1\bar{1}0]$. This anisotropy vanishes in control measurements on thicker Fe films or samples without $C_{2\mathrm{v}}$ symmetry of the spin-orbit fields, demonstrating that the observed anisotropic polar magneto-optic Kerr effect stems from the spin-orbit interaction at the Fe/GaAs(001) interface, as has previously been predicted by first-principles calculations [23]. The twofold symmetry of the Kerr angle is fully reproduced by a phenomenological model based on the interference of interfacial Bychkov-Rashba and Dresselhaus spin-orbit coupling fields.

The AP-MOKE is found to be largest for the 4 ML Fe/GaAs sample with an anisotropy of roughly 0.7%. This value is two orders of magnitude smaller than theoretically expected, as the first-principles calculations of Putz *et al.* suggest for the used photon energy an anisotropy of more than 50%. This discrepancy can be explained by the fact that the experiment is carried out at room temperature, whereas the calculations assume a temperature of $T = 0$. In addition, the investigated samples contain structural imperfections, which are not included in the theoretical considerations.

All in all, the experiments have proven the existence of the theoretically expected Kerr rotation anisotropy in the Fe/GaAs(001) heterostructure system. However, the effect is rather small. Therefore, in future experiments it should be investigated to what extent the AP-MOKE can be enhanced by using optimized measurement parameters or a more suitable material system. For example, it should be possible to increase the Kerr rotation anisotropy by cooling the samples to low temperatures. Moreover, according to the density functional theory calculations of Putz *et al.* the wavelength of the probing laser beam is a crucial parameter

for the AP-MOKE. A huge anisotropy has been predicted for a photon energy of about 10 eV [23]. For that reason, the experiments should be repeated at a synchrotron, which allows to use light with photon energies well above the visible spectrum. In addition, the Fe could be grown on a zinc-blende semiconductor with larger spin-orbit coupling parameters than GaAs. Just recently, it has been demonstrated that the insertion of one monolayer of InAs between the GaAs buffer layer and the Fe enhances the amplitude of the AP-MOKE by a factor of three compared to the case of the here investigated Fe/GaAs(001) [199].

Another route for future experiments would be to combine the here presented magneto-optical characterization of interfacial spin-orbit fields with electrical detection techniques. It has been shown that the magnitude of the spin-orbit torques at the Fe/GaAs(001) interface can be quantified by employing the so-called spin-orbit ferromagnetic resonance (SO-FMR) technique [200]. This experiment makes use of a micro-fabricated Fe/GaAs(001) stripe. With the aid of a Kerr microscope it should be possible to perform both SO-FMR and AP-MOKE measurements on the same stripe. This allows a direct comparison of the two detection approaches, which is of particular interest, as the AP-MOKE measurement does not yield absolute values for the spin-orbit fields at the interface, whereas SO-FMR does. Another advantage of this approach is that the samples can be mounted in a cryostat, which allows for temperature dependent measurements. Most importantly, due to the used microscope objective a rocking of the back-reflected laser beam arising from the sample rotation is expected to have no significant influence on the detected signals. Thus, the experiment should be much easier to carry out compared to the approach used in this work, as a tedious sample mounting and aligning procedure is no longer necessary.

A. Spin dynamics with anisotropic spin relaxation

The dynamics of a spin $\boldsymbol{s}$, which is the total spin of an ensemble of electrons, in a magnetic field $\boldsymbol{B}$ (ignoring spin drift and diffusion) is given by the Bloch equation [43, 83]

$$\frac{\mathrm{d}\boldsymbol{s}}{\mathrm{d}t} = \boldsymbol{s} \times \boldsymbol{\omega_0} - \hat{\boldsymbol{\Gamma}}\boldsymbol{s}. \tag{A.1}$$

Here $\boldsymbol{\omega_0} = \frac{g\mu_\mathrm{B}}{\hbar}\boldsymbol{B}$ is the Larmor precession frequency and the tensor $\hat{\boldsymbol{\Gamma}}$ describes the anisotropic spin relaxation. By choosing the coordinate system along the principal axes of the tensor $\hat{\boldsymbol{\Gamma}}$ ($\hat{\boldsymbol{\Gamma}} = \mathrm{diag}(1/\tau_x, 1/\tau_y, 1/\tau_z)$) and taking $\boldsymbol{B}||z$-direction ($\boldsymbol{\omega_0} = (0, 0, \omega_0)$) this equation can be rewritten as a set of three coupled linear differential equations:

$$\frac{\mathrm{d}s_x}{\mathrm{d}t} - \omega_0 s_y + \frac{s_x}{\tau_x} = 0, \tag{A.2}$$

$$\frac{\mathrm{d}s_y}{\mathrm{d}t} + \omega_0 s_x + \frac{s_y}{\tau_y} = 0, \tag{A.3}$$

$$\frac{\mathrm{d}s_z}{\mathrm{d}t} + \frac{s_z}{\tau_z} = 0. \tag{A.4}$$

In the experiment the spin polarization is injected in the sample plane, perpendicular to the magnetic field, which forces the spins to precess. The corresponding initial condition for the differential equation problem is therefore given by

$$\boldsymbol{s}(0) = \begin{pmatrix} s_0 \cos(\phi) \\ s_0 \sin(\phi) \\ 0 \end{pmatrix}, \tag{A.5}$$

which represents an initial spin state with magnitude s_0 within the xy-plane, which is tilted by an angle ϕ with respect to the x-axis.

Since the z-component of $\boldsymbol{s}$ is decoupled from the other two components, one finds for the out-of-plane spin component the trivial solution $s_z(t) \equiv 0$. For the remaining two in-plane components one uses an ansatz of the form

$$s_x(t) = A_x \mathrm{e}^{-\lambda t}, \tag{A.6}$$

$$s_y(t) = A_y \mathrm{e}^{-\lambda t}, \tag{A.7}$$

and obtains the characteristic equation of the problem

$$\det \begin{pmatrix} \frac{1}{\tau_x} - \lambda & -\omega_0 \\ \omega_0 & \frac{1}{\tau_y} - \lambda \end{pmatrix} = 0. \tag{A.8}$$

By solving this determinant equation one finds the eigenvalues

$$\lambda_{1,2} = \frac{1}{\bar{\tau}} \pm \mathrm{i}\tilde{\omega} \tag{A.9}$$

with

$$\frac{1}{\bar{\tau}} = \frac{1}{2}\left(\frac{1}{\tau_x} + \frac{1}{\tau_y}\right) \qquad \text{and} \qquad \tilde{\omega} = \sqrt{\omega_0^2 - \frac{1}{4}\left(\frac{1}{\tau_x} - \frac{1}{\tau_y}\right)^2}. \tag{A.10}$$

Note that $\mathrm{Re}(\lambda_{1,2}) > 0$ for all ω_0. Thus, the boundary conditions $s_x(\infty) = s_y(\infty) = 0$, which describe a vanishing spin signal for large t, are always fulfilled. After solving a few last equations to satisfy the boundary conditions for $t = 0$ as well, one finally obtains for the time evolution of the in-plane spin components:

$$s_x(t) = s_0 \exp\left(-\frac{t}{\bar{\tau}}\right)\left\{\cos(\phi)\cos(\tilde{\omega}t) + \left[\omega_0 \sin(\phi) - \frac{1}{2}\left(\frac{1}{\tau_x} - \frac{1}{\tau_y}\right)\cos(\phi)\right]\frac{\sin(\tilde{\omega}t)}{\tilde{\omega}}\right\}, \tag{A.11}$$

$$s_y(t) = s_0 \exp\left(-\frac{t}{\bar{\tau}}\right)\left\{\sin(\phi)\cos(\tilde{\omega}t) - \left[\omega_0 \cos(\phi) - \frac{1}{2}\left(\frac{1}{\tau_x} - \frac{1}{\tau_y}\right)\sin(\phi)\right]\frac{\sin(\tilde{\omega}t)}{\tilde{\omega}}\right\}. \tag{A.12}$$

Thus, for small magnetic fields, the spins decay exponentially. For larger magnetic fields (when $\tilde{\omega}$ becomes real) the spins show a damped, precessional motion, with the decay time given by the harmonic mean $\bar{\tau}$ of the two in-plane spin lifetimes τ_x and τ_y.

Hanle lineshape with detection along $\boldsymbol{x}$

Using the solution for $\boldsymbol{s}(t)$ it is possible to determine the shape of the Hanle depolarization curves. The cleaved edge detection method is exclusively sensitive to the x-component of the spins. Therefore, the Hanle signal can be calculated by summing up the x-components of all spins, which have been injected into the system in the past, i.e. by integrating the spin signal $s_x(t)$ over all possible transit times from injection to detection:

$$s_x(\omega_0) = \int_0^\infty s_x(t)\mathrm{d}t = \\ = \frac{s_0\tau_x}{1 + (\omega_0\sqrt{\tau_x\tau_y})^2} \cdot \Big(\cos(\phi) + \omega_0\tau_y \sin(\phi)\Big). \tag{A.13}$$

The Hanle curve exhibits a Lorentzian lineshape, just like in the case of systems with isotropic spin relaxation. In the present case, however, the width of the depolarization curve is determined by the geometric mean $\sqrt{\tau_x \tau_y}$ of the spin lifetimes along the two in-plane principal axes.

Hanle lineshape with detection along injection direction
Another possibility to investigate the Hanle depolarization would be to consider only the spin component along the initial injection direction ϕ (which, however, is experimentally harder to achieve). In this case the Hanle lineshape is given by

$$\begin{aligned} s_\phi(\omega_0) &= \int_0^\infty s_\phi(t)\mathrm{d}t = \int_0^\infty \Big(s_x(t)\cos(\phi) + s_y(t)\sin(\phi)\Big)\mathrm{d}t = \\ &= \frac{s_0}{1+(\omega_0\sqrt{\tau_x\tau_y})^2} \cdot \Big(\tau_x \cos^2(\phi) + \tau_y \sin^2(\phi)\Big)\,. \end{aligned} \tag{A.14}$$

Again, the Hanle curve exhibits a Lorentzian lineshape and its width is determined by the geometric mean value $\sqrt{\tau_x \tau_y}$.

B. Theoretical analysis of the Kerr detection units

The light intensities, which reach the photodiodes of the Kerr detection units, are calculated by means of the Stokes vector and Müller matrix formalism (cf. e.g. Refs. [201, 202]). In general, elliptically polarized light can be described by a Stokes vector of the form

$$S = \begin{pmatrix} I_0 \\ I_0 \cos(2\varepsilon)\cos(2\gamma) \\ I_0 \cos(2\varepsilon)\sin(2\gamma) \\ I_0 \sin(2\varepsilon) \end{pmatrix}. \tag{B.1}$$

Here, I_0 is the intensity of the light, ε the ellipticity and γ the angle between the x-axis and the semi-major axis of the polarization ellipse (see Fig. B.1). In the experiment the laser light is linearly polarized by polarizer P_1, with the polarization axis being vertically oriented, before it hits the sample. Due to the polar magneto-optic Kerr effect the reflected light obtains a Kerr ellipticity ε_K and its polarization axis is rotated by the angle θ_K. Hence, the Stokes vector of the reflected light can be written as

$$S_{\mathrm{Kerr}} = I_0 \begin{pmatrix} 1 \\ \cos(2\varepsilon_K)\cos\left(2\cdot(90^\circ+\theta_K)\right) \\ \cos(2\varepsilon_K)\sin\left(2\cdot(90^\circ+\theta_K)\right) \\ \sin(2\varepsilon_K) \end{pmatrix} = I_0 \begin{pmatrix} 1 \\ -\cos(2\varepsilon_K)\cos(2\theta_K) \\ -\cos(2\varepsilon_K)\sin(2\theta_K) \\ \sin(2\varepsilon_K) \end{pmatrix}. \tag{B.2}$$

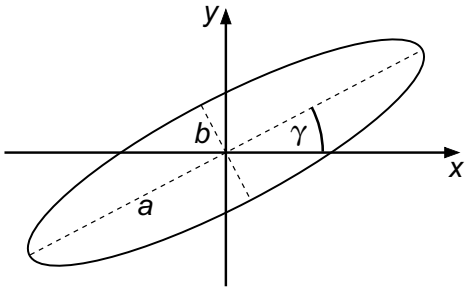

Figure B.1: Elliptically polarized light is fully described by the angle γ and the ellipticity ε. γ is the angle between the x-axis and the semi-major axis of the ellipse. The ellipticity of the light is defined by $\varepsilon = \arctan(b/a)$, where a and b are the lenghts of the semi-major and semi-minor axis, respectively.

Wollaston detector

In the Wollaston detector the reflected light is split by a Wollaston prism into two beams, which are perpendicularly polarized. The Wollaston prism behaves effectively like two linear polarizers with optical axes oriented along $\mp 45°$. The corresponding Müller matrices are

$$M_{\text{Wollaston 1,2}} = \frac{1}{2}\begin{pmatrix} 1 & 0 & \mp 1 & 0 \\ 0 & 0 & 0 & 0 \\ \mp 1 & 0 & 1 & 0 \\ 0 & 0 & 0 & 0 \end{pmatrix}. \tag{B.3}$$

Therefore, the Stokes vectors of the two split beams can be calculated to

$$S_{1,2} = M_{\text{Wollaston 1,2}} \cdot S_{\text{Kerr}} = \frac{I_0}{2}\begin{pmatrix} 1 \pm \sin(2\theta_{\text{K}})\cos(2\varepsilon_{\text{K}}) \\ 0 \\ \mp 1 - \sin(2\theta_{\text{K}})\cos(2\varepsilon_{\text{K}}) \\ 0 \end{pmatrix} \tag{B.4}$$

and their intensities, which are given by the first components of the Stokes vectors, are:

$$I_{1,2} = \frac{I_0}{2} \cdot \Big(1 \pm \sin(2\theta_{\text{K}})\cos(2\varepsilon_{\text{K}})\Big). \tag{B.5}$$

The difference and the sum signals then read:

$$\Delta(\theta_{\text{K}}, \varepsilon_{\text{K}}) = I_1 - I_2 = I_0 \sin(2\theta_{\text{K}})\cos(2\varepsilon_{\text{K}}), \tag{B.6}$$

$$\Sigma(\theta_{\text{K}}, \varepsilon_{\text{K}}) = I_1 + I_2 = I_0. \tag{B.7}$$

Small-angle approximation finally yields for the Kerr rotation angle:

$$\theta_{\text{K}} \approx \frac{\Delta(\theta_{\text{K}}, \varepsilon_{\text{K}})}{2\Sigma(\theta_{\text{K}}, \varepsilon_{\text{K}})}. \tag{B.8}$$

Crossed polarizers detector

The Müller matrix of analyzer P_2 can be written as

$$M_{\text{Analyzer}}(\alpha) = \frac{1}{2}\begin{pmatrix} 1 & \cos(2\alpha) & \sin(2\alpha) & 0 \\ \cos(2\alpha) & \cos^2(2\alpha) & \sin(2\alpha)\cos(2\alpha) & 0 \\ \sin(2\alpha) & \sin(2\alpha)\cos(2\alpha) & \sin^2(2\alpha) & 0 \\ 0 & 0 & 0 & 0 \end{pmatrix}, \tag{B.9}$$

where α is the angle between the x-axis and the polarization axis of P_2. Multiplication with S_{Kerr} yields the Stokes vector of the light, which reaches the

photodiode:

$$S_{\text{Photodiode}} = \frac{I_0}{2} \cdot \begin{pmatrix} 1 - \cos(2\alpha)\cos(2\theta_\text{K})\cos(2\varepsilon_\text{K}) - \sin(2\alpha)\sin(2\theta_\text{K})\cos(2\varepsilon_\text{K}) \\ \cos(2\alpha) - \cos^2(2\alpha)\cos(2\theta_\text{K})\cos(2\varepsilon_\text{K}) - \sin(2\alpha)\cos(2\alpha)\sin(2\theta_\text{K})\cos(2\varepsilon_\text{K}) \\ \sin(2\alpha) - \sin(2\alpha)\cos(2\alpha)\cos(2\theta_\text{K})\cos(2\varepsilon_\text{K}) - \sin^2(2\alpha)\sin(2\theta_\text{K})\cos(2\varepsilon_\text{K}) \\ 0 \end{pmatrix}. \tag{B.10}$$

The first component is the light intensity, which is detected by the photodiode:

$$\begin{aligned} I(\alpha, \theta_\text{K}, \varepsilon_\text{K}) &= \frac{I_0}{2} \cdot \Big[1 - \cos(2\alpha)\cos(2\theta_\text{K})\cos(2\varepsilon_\text{K}) - \sin(2\alpha)\sin(2\theta_\text{K})\cos(2\varepsilon_\text{K})\Big] = \\ &= \frac{I_0}{2} \cdot \Big[1 - \cos(2(\alpha - \theta_\text{K}))\cos(2\varepsilon_\text{K})\Big]. \end{aligned} \tag{B.11}$$

Taking the intensity difference between positive and negative applied magnetic field yields:

$$\begin{aligned} \Delta I &= \Big|I(+\boldsymbol{H}) - I(-\boldsymbol{H})\Big| = \Big|I(\alpha, \theta_\text{K}, \varepsilon_\text{K}) - I(\alpha, -\theta_\text{K}, -\varepsilon_\text{K})\Big| = \\ &= I_0 \sin(2\alpha)\sin(2\theta_\text{K})\cos(2\varepsilon_\text{K}) \approx 2I_0 \sin(2\alpha)\theta_\text{K}, \end{aligned} \tag{B.12}$$

where again small-angle approximation was used in the last step. This finally leads to the expression

$$\theta_\text{K} \approx \frac{\Delta I}{2I_0 \sin(2\alpha)} \tag{B.13}$$

for the Kerr rotation angle.

Bibliography

[1] J. Bardeen and W. H. Brattain. *The Transistor, A Semi-Conductor Triode.* Phys. Rev. **74**, 230 (1948).

[2] J. Bardeen and W. H. Brattain. *Physical Principles Involved in Transistor Action.* Phys. Rev. **75**, 1208 (1949).

[3] J. S. Kilby. *Invention of the Integrated Circuit.* IEEE Trans. Electron Dev. **23**, 648 (1976).

[4] G. E. Moore. *Cramming More Components onto Integrated Circuits.* Electronics **38**, 114 (1965).

[5] G. E. Moore. *Progress in Digital Integrated Electronics.* Tech. Dig. IEDM **21**, 11 (1975).

[6] S. E. Thompson and S. Parthasarathy. *Moore's law: the future of Si microelectronics.* Mater. Today **9**, 20 (2006).

[7] M. M. Waldrop. *The chips are down for Moore's law.* Nature **530**, 144 (2016).

[8] S. A. Wolf, D. D. Awschalom, R. A. Buhrman, J. M. Daughton, S. von Molnár, M. L. Roukes, A. Y. Chtchelkanova, and D. M. Treger. *Spintronics: A Spin-Based Electronics Vision for the Future.* Science **294**, 1488 (2001).

[9] M. Johnson and R. H. Silsbee. *Interfacial charge-spin coupling: Injection and detection of spin magnetization in metals.* Phys. Rev. Lett. **55**, 1790 (1985).

[10] M. N. Baibich, J. M. Broto, A. Fert, F. Nguyen Van Dau, F. Petroff, P. Etienne, G. Creuzet, A. Friederich, and J. Chazelas. *Giant Magnetoresistance of (001)Fe/(001)Cr Magnetic Superlattices.* Phys. Rev. Lett. **61**, 2472 (1988).

[11] G. Binasch, P. Grünberg, F. Saurenbach, and W. Zinn. *Enhanced magnetoresistance in layered magnetic structures with antiferromagnetic interlayer exchange.* Phys. Rev. B **39**, 4828 (1989).

[12] M. Jullière. *Tunneling between ferromagnetic films.* Phys. Lett. A **54**, 225 (1975).

[13] T. Miyazaki and N. Tezuka. *Giant magnetic tunneling effect in $Fe/Al_2O_3/Fe$ junction.* J. Magn. Magn. Mater. **139**, L231 (1995).

[14] D. D. Awschalom and M. E. Flatté. *Challenges for semiconductor spintronics.* Nature Phys. **3**, 153 (2007).

[15] International Roadmap Committee. *International Technology Roadmap for Semiconductors 2.0 - 2015 Edition.* Available online at: http://www.itrs2.net, 2015.

[16] S. Datta and B. Das. *Electronic analog of the electro-optic modulator.* Appl. Phys. Lett. **56**, 665 (1990).

[17] P. Kotissek, M. Bailleul, M. Sperl, A. Spitzer, D. Schuh, W. Wegscheider, C. H. Back, and G. Bayreuther. *Cross-sectional imaging of spin injection into a semiconductor.* Nature Phys. **3**, 872 (2007).

[18] P. Kotissek. *Remanente Spininjektion und zweidimensionale Spindichte-Verteilung in einem Halbleiter.* Universität Regensburg, PhD thesis, 2008.

[19] B. Endres, F. Hoffmann, C. Wolf, A. Einwanger, M. Utz, D. Schuh, G. Woltersdorf, M. Ciorga, D. Weiss, C. H. Back, and G. Bayreuther. *Bias dependence of spin injection into GaAs from Fe, FeCo, and (Ga,Mn)As contacts.* J. Appl. Phys. **109**, 07C505 (2011).

[20] B. Endres, M. Ciorga, R. Wagner, S. Ringer, M. Utz, D. Bougeard, D. Weiss, C. H. Back, and G. Bayreuther. *Nonuniform current and spin accumulation in a 1 μm thick n-GaAs channel.* Appl. Phys. Lett. **100**, 092405 (2012).

[21] B. Endres, M. Ciorga, M. Schmid, M. Utz, D. Bougeard, D. Weiss, G. Bayreuther, and C. H. Back. *Demonstration of the spin solar cell and spin photodiode effect.* Nat. Commun. **4**, 2068 (2013).

[22] B. Endres. *Spin injection into GaAs.* Universität Regensburg, PhD thesis, 2013.

[23] S. Putz, M. Gmitra, and J. Fabian. *Anisotropic optical properties of Fe/GaAs(001) nanolayers from first principles.* Phys. Rev. B **90**, 045315 (2014).

[24] S. Putz. *Optical properties of hydrogenated graphene and Fe/GaAs(001) from first principles.* Universität Regensburg, PhD thesis, 2014.

[25] I. Žutić, J. Fabian, and S. Das Sarma. *Spintronics: Fundamentals and applications.* Rev. Mod. Phys. **76**, 323 (2004).

[26] S. Hunklinger. *Festkörperphysik.* 2. Aufl. München: Oldenbourg Wissenschaftsverlag, 2009.

[27] S. Blügel, D. Bürgler, M. Morgenstern, C. M. Schneider, and R. Waser (Eds.). *Spintronics - From GMR to Quantum Information.* Forschungszentrum Jülich: Lecture Notes of the 40th Spring School, 2009.

[28] C. Bosio, J. L. Staehli, M. Guzzi, G. Burri, and R. A. Logan. *Direct-energy-gap dependence on Al concentration in $Al_xGa_{1-x}As$.* Phys. Rev. B **38**, 3263 (1988).

[29] D. J. Chadi and K. J. Chang. *Theory of the Atomic and Electronic Structure of DX Centers in GaAs and $Al_xGa_{1-x}As$ Alloys.* Phys. Rev. Lett. **61**, 873 (1988).

[30] D. J. Chadi and K. J. Chang. *Energetics of DX-center formation in GaAs and $Al_xGa_{1-x}As$ alloys.* Phys. Rev. B **39**, 10063 (1989).

[31] M. I. Nathan. *Persistent photoconductivity in AlGaAs/GaAs modulation doped layers and field effect transistors: A review.* Solid-State Electron. **29**, 167 (1986).

[32] P. M. Mooney. *Deep donor levels (DX centers) in III-V semiconductors.* J. Appl. Phys. **67**, R1 (1990).

[33] P. M. Mooney. *Donor-related levels in GaAs and $Al_xGa_{1-x}As$.* Semicond. Sci. Technol. **6**, B1 (1991).

[34] A. Kastalsky and J. C. M. Hwang. *Study of persistent photoconductivity effect in n-type selectively doped AlGaAs/GaAs heterojunction.* Solid State Commun. **51**, 317 (1984).

[35] M. J. Kane, N. Apsley, D. A. Anderson, L. L. Taylor, and T. Kerr. *Parallel conduction in $GaAs/Al_xGa_{1-x}As$ modulation doped heterojunctions.* J. Phys. C **18**, 5629 (1985).

[36] M. A. Reed, W. P. Kirk, and P. S. Kobiela. *Investigation of parallel conduction in $GaAs/Al_xGa_{1-x}As$ modulation-doped structures in the quantum limit.* IEEE J. Quant. Electron. **22**, 1753 (1986).

[37] A. Fert, J.-M. George, H. Jaffrès, and R. Mattana. *Semiconductors Between Spin-Polarized Sources and Drains.* IEEE Trans. Electron Dev. **54**, 921 (2007).

[38] C. Chappert, A. Fert, and F. Nguyen Van Dau. *The emergence of spin electronics in data storage.* Nat. Mater. **6**, 813 (2007).

[39] G. Schmidt, D. Ferrand, L. W. Molenkamp, A. T. Filip, and B. J. van Wees. *Fundamental obstacle for electrical spin injection from a ferromagnetic metal into a diffusive semiconductor.* Phys. Rev. B **62**, R4790 (2000).

[40] E. I. Rashba. *Theory of electrical spin injection: Tunnel contacts as a solution of the conductivity mismatch problem.* Phys. Rev. B **62**, R16267 (2000).

[41] A. Fert and H. Jaffrès. *Conditions for efficient spin injection from a ferromagnetic metal into a semiconductor.* Phys. Rev. B **64**, 184420 (2001).

[42] E. I. Rashba. *Diffusion theory of spin injection through resistive contacts.* Eur. Phys. J. B **29**, 513 (2002).

[43] J. Fabian, A. Matos-Abiague, C. Ertler, P. Stano, and I. Žutić. *Semiconductor Spintronics.* Acta Phys. Slov. **57**, 565 (2007).

[44] F. A. Padovani and R. Stratton. *Field and thermionic-field emission in Schottky barriers.* Solid-State Electron. **9**, 695 (1966).

[45] O. Wunnicke, P. Mavropoulos, R. Zeller, P. H. Dederichs, and D. Grundler. *Ballistic spin injection from Fe(001) into ZnSe and GaAs.* Phys. Rev. B **65**, 241306 (2002).

[46] O. Wunnicke, P. Mavropoulos, R. Zeller, and P. H. Dederichs. *Ballistic spin injection from Fe into ZnSe(001), (111), and (110), and into GaAs(001).* J. Phys.: Condens. Matter **16**, 4643 (2004).

[47] B. D. Schultz, N. Marom, D. Naveh, X. Lou, C. Adelmann, J. Strand, P. A. Crowell, L. Kronik, and C. J. Palmstrøm. *Spin injection across the Fe/GaAs interface: Role of interfacial ordering.* Phys. Rev. B **80**, 201309 (2009).

[48] A. T. Hanbicki, B. T. Jonker, G. Itskos, G. Kioseoglou, and A. Petrou. *Efficient electrical spin injection from a magnetic metal/tunnel barrier contact into a semiconductor.* Appl. Phys. Lett. **80**, 1240 (2002).

[49] A. T. Hanbicki, O. M. J. van 't Erve, R. Magno, G. Kioseoglou, C. H. Li, B. T. Jonker, G. Itskos, R. Mallory, M. Yasar, and A. Petrou. *Analysis of the transport process providing spin injection through an Fe/AlGaAs Schottky barrier.* Appl. Phys. Lett. **82**, 4092 (2003).

[50] C. Adelmann, X. Lou, J. Strand, C. J. Palmstrøm, and P. A. Crowell. *Spin injection and relaxation in ferromagnet-semiconductor heterostructures.* Phys. Rev. B **71**, 121301 (2005).

[51] O. M. J. van 't Erve, G. Kioseoglou, A. T. Hanbicki, C. H. Li, and B. T. Jonker. *Remanent electrical spin injection from Fe into AlGaAs/GaAs light emitting diodes.* Appl. Phys. Lett. **89**, 072505 (2006).

[52] T. H. Lee, H. C. Koo, K. H. Kim, H.-j. Kim, J. Chang, S.-H. Han, J. Hong, and S. H. Lim. *Temperature dependence of spin injection efficiency in an epitaxially grown Fe/GaAs hybrid structure.* J. Magn. Magn. Mater. **321**, 3795 (2009).

[53] G. Salis, A. Fuhrer, and S. F. Alvarado. *Signatures of dynamically polarized nuclear spins in all-electrical lateral spin transport devices.* Phys. Rev. B **80**, 115332 (2009).

[54] H. Ohno, A. Shen, F. Matsukura, A. Oiwa, A. Endo, S. Katsumoto, and Y. Iye. *(Ga,Mn)As: A new diluted magnetic semiconductor based on GaAs.* Appl. Phys. Lett. **69**, 363 (1996).

[55] H. Ohno. *Making Nonmagnetic Semiconductors Ferromagnetic.* Science **281**, 951 (1998).

[56] A. X. Gray, J. Minár, S. Ueda, P. R. Stone, Y. Yamashita, J. Fujii, J. Braun, L. Plucinski, C. M. Schneider, G. Panaccione, H. Ebert, O. D. Dubon, K. Kobayashi, and C. S. Fadley. *Bulk electronic structure of the dilute magnetic semiconductor $Ga_{1-x}Mn_xAs$ through hard X-ray angle-resolved photoemission.* Nat. Mater. **11**, 957 (2012).

[57] T. Dietl, H. Ohno, F. Matsukura, J. Cibert, and D. Ferrand. *Zener Model Description of Ferromagnetism in Zinc-Blende Magnetic Semiconductors.* Science **287**, 1019 (2000).

[58] K. Sato, L. Bergqvist, J. Kudrnovský, P. H. Dederichs, O. Eriksson, I. Turek, B. Sanyal, G. Bouzerar, H. Katayama-Yoshida, V. A. Dinh, T. Fukushima, H. Kizaki, and R. Zeller. *First-principles theory of dilute magnetic semiconductors.* Rev. Mod. Phys. **82**, 1633 (2010).

[59] L. Chen, S. Yan, P. F. Xu, J. Lu, W. Z. Wang, J. J. Deng, X. Qian, Y. Ji, and J. H. Zhao. *Low-temperature magnetotransport behaviors of heavily Mn-doped (Ga,Mn)As films with high ferromagnetic transition temperature.* Appl. Phys. Lett. **95**, 182505 (2009).

[60] L. Chen, X. Yang, F. Yang, J. Zhao, J. Misuraca, P. Xiong, and S. von Molnár. *Enhancing the Curie Temperature of Ferromagnetic Semiconductor (Ga,Mn)As to 200 K via Nanostructure Engineering.* Nano Lett. **11**, 2584 (2011).

[61] P. Němec, V. Novák, N. Tesařová, E. Rozkotová, H. Reichlová, D. Butkovičová, F. Trojánek, K. Olejník, P. Malý, R. P. Campion, B. L. Gallagher, J. Sinova, and T. Jungwirth. *The essential role of carefully optimized synthesis for elucidating intrinsic material properties of (Ga,Mn)As.* Nat. Commun. **4**, 1422 (2013).

[62] Y. Ohno, D. K. Young, B. Beschoten, F. Matsukura, H. Ohno, and D. D. Awschalom. *Electrical spin injection in a ferromagnetic semiconductor heterostructure.* Nature **402**, 790 (1999).

[63] M. Kohda, Y. Ohno, K. Takamura, F. Matsukura, and H. Ohno. *A Spin Esaki Diode.* Jpn. J. Appl. Phys. **40**, L1274 (2001).

[64] A. G. Chynoweth, W. L. Feldmann, and R. A. Logan. *Excess Tunnel Current in Silicon Esaki Junctions.* Phys. Rev. **121**, 684 (1961).

[65] J. Shiogai, M. Ciorga, M. Utz, D. Schuh, M. Kohda, D. Bougeard, T. Nojima, J. Nitta, and D. Weiss. *Giant enhancement of spin detection sensitivity in (Ga,Mn)As/GaAs Esaki diodes.* Phys. Rev. B **89**, 081307 (2014).

[66] P. Van Dorpe, Z. Liu, W. Van Roy, V. F. Motsnyi, M. Sawicki, G. Borghs, and J. De Boeck. *Very high spin polarization in GaAs by injection from a (Ga,Mn)As Zener diode.* Appl. Phys. Lett. **84**, 3495 (2004).

[67] P. Van Dorpe, W. Van Roy, J. De Boeck, G. Borghs, P. Sankowski, P. Kacman, J. A. Majewski, and T. Dietl. *Voltage-controlled spin injection in a (Ga,Mn)As/(Al,Ga)As Zener diode.* Phys. Rev. B **72**, 205322 (2005).

[68] M. Ciorga, A. Einwanger, U. Wurstbauer, D. Schuh, W. Wegscheider, and D. Weiss. *Electrical spin injection and detection in lateral all-semiconductor devices.* Phys. Rev. B **79**, 165321 (2009).

[69] M. Ciorga, M. Utz, D. Schuh, D. Bougeard, and D. Weiss. *Effect of contact geometry on spin-transport signals in nonlocal (Ga,Mn)As/GaAs devices.* Phys. Rev. B **88**, 155308 (2013).

[70] M. I. D'yakonov and V. I. Perel'. *Spin orientation of electrons associated with the interband absorption of light in semiconductors.* Sov. Phys. JETP **33**, 1053 (1971).

[71] M. I. D'yakonov and V. I. Perel'. *Spin relaxation of conduction electrons in noncentrosymmetric semiconductors.* Sov. Phys. Solid State **13**, 3023 (1972).

[72] M. I. D'yakonov and V. Y. Kachorovskii. *Spin relaxation of two-dimensional electrons in noncentrosymmetric semiconductors.* Sov. Phys. Semicond. **20**, 110 (1986).

[73] G. Dresselhaus. *Spin-Orbit Coupling Effects in Zinc Blende Structures.* Phys. Rev. **100**, 580 (1955).

[74] R. I. Dzhioev, K. V. Kavokin, V. L. Korenev, M. V. Lazarev, B. Y. Meltser, M. N. Stepanova, B. P. Zakharchenya, D. Gammon, and D. S. Katzer. *Low-temperature spin relaxation in n-type GaAs.* Phys. Rev. B **66**, 245204 (2002).

[75] M. M. Glazov and E. L. Ivchenko. *Precession Spin Relaxation Mechanism Caused by Frequent Electron-Electron Collisions.* JETP Lett. **75**, 403 (2002).

[76] M. M. Glazov. *Mechanism of the D'yakonov-Perel' Spin Relaxation in Frequent Electron-Electron Collisions in a Quantum Well with a Finite Width.* Phys. Solid State **45**, 1162 (2003).

[77] M. M. Glazov and E. L. Ivchenko. *Effect of Electron-Electron Interaction on Spin Relaxation of Charge Carriers in Semiconductors.* JETP **99**, 1279 (2004).

[78] W. J. H. Leyland, G. H. John, R. T. Harley, M. M. Glazov, E. L. Ivchenko, D. A. Ritchie, I. Farrer, A. J. Shields, and M. Henini. *Enhanced spin-relaxation time due to electron-electron scattering in semiconductor quantum wells.* Phys. Rev. B **75**, 165309 (2007).

[79] M. I. Dyakonov (Ed.). *Spin Physics in Semiconductors.* Berlin Heidelberg: Springer-Verlag, 2008.

[80] Y. A. Bychkov and E. I. Rashba. *Properties of a 2D electron gas with lifted spectral degeneracy.* JETP Lett. **39**, 78 (1984).

[81] Y. A. Bychkov and E. I. Rashba. *Oscillatory effects and the magnetic susceptibility of carriers in inversion layers.* J. Phys. C **17**, 6039 (1984).

[82] N. S. Averkiev, L. E. Golub, A. S. Gurevich, V. P. Evtikhiev, V. P. Kochereshko, A. V. Platonov, A. S. Shkolnik, and Y. P. Efimov. *Spin-relaxation anisotropy in asymmetrical (001) $Al_xGa_{1-x}As$ quantum wells from Hanle-effect measurements: Relative strengths of Rashba and Dresselhaus spin-orbit coupling.* Phys. Rev. B **74**, 033305 (2006).

[83] N. S. Averkiev and L. E. Golub. *Spin relaxation anisotropy: microscopic mechanisms for 2D systems.* Semicond. Sci. Technol. **23**, 114002 (2008).

[84] M. Griesbeck. *Spin dynamics in high-mobility two-dimensional electron systems embedded in GaAs/AlGaAs quantum wells.* Universität Regensburg, PhD thesis, 2012.

[85] N. S. Averkiev and L. E. Golub. *Giant spin relaxation anisotropy in zinc-blende heterostructures.* Phys. Rev. B **60**, 15582 (1999).

[86] N. S. Averkiev, L. E. Golub, and M. Willander. *Spin relaxation anisotropy in two-dimensional semiconductor systems.* J. Phys.: Condens. Matter **14**, R271 (2002).

[87] Y. Ohno, R. Terauchi, T. Adachi, F. Matsukura, and H. Ohno. *Spin Relaxation in GaAs(110) Quantum Wells.* Phys. Rev. Lett. **83**, 4196 (1999).

[88] D. Stich, J. Zhou, T. Korn, R. Schulz, D. Schuh, W. Wegscheider, M. W. Wu, and C. Schüller. *Effect of Initial Spin Polarization on Spin Dephasing and the Electron g Factor in a High-Mobility Two-Dimensional Electron System.* Phys. Rev. Lett. **98**, 176401 (2007).

[89] V. Lechner, L. E. Golub, F. Lomakina, V. V. Bel'kov, P. Olbrich, S. Stachel, I. Caspers, M. Griesbeck, M. Kugler, M. J. Hirmer, T. Korn, C. Schüller, D. Schuh, W. Wegscheider, and S. D. Ganichev. *Spin and orbital mechanisms of the magnetogyrotropic photogalvanic effects in GaAs/$Al_xGa_{1-x}As$ quantum well structures.* Phys. Rev. B **83**, 155313 (2011).

[90] D. Stich, J. H. Jiang, T. Korn, R. Schulz, D. Schuh, W. Wegscheider, M. W. Wu, and C. Schüller. *Detection of large magnetoanisotropy of electron spin dephasing in a high-mobility two-dimensional electron system in a [001] GaAs/$Al_xGa_{1-x}As$ quantum well.* Phys. Rev. B **76**, 073309 (2007).

[91] R. Völkl, M. Schwemmer, M. Griesbeck, S. A. Tarasenko, D. Schuh, W. Wegscheider, C. Schüller, and T. Korn. *Spin polarization, dephasing, and photoinduced spin diffusion in (110)-grown two-dimensional electron systems.* Phys. Rev. B **89**, 075424 (2014).

[92] S. Döhrmann, D. Hägele, J. Rudolph, M. Bichler, D. Schuh, and M. Oestreich. *Anomalous Spin Dephasing in (110) GaAs Quantum Wells: Anisotropy and Intersubband Effects.* Phys. Rev. Lett. **93**, 147405 (2004).

[93] J. M. Kikkawa and D. D. Awschalom. *Lateral drag of spin coherence in gallium arsenide.* Nature **397**, 139 (1999).

[94] M. E. Flatté and J. M. Byers. *Spin Diffusion in Semiconductors.* Phys. Rev. Lett. **84**, 4220 (2000).

[95] I. D'Amico and G. Vignale. *Theory of spin Coulomb drag in spin-polarized transport.* Phys. Rev. B **62**, 4853 (2000).

[96] I. D'Amico and G. Vignale. *Spin diffusion in doped semiconductors: The role of Coulomb interactions.* Europhys. Lett. **55**, 566 (2001).

[97] I. D'Amico and G. Vignale. *Coulomb interaction effects in spin-polarized transport.* Phys. Rev. B **65**, 085109 (2002).

[98] K. Flensberg, T. Stibius Jensen, and N. Asger Mortensen. *Diffusion equation and spin drag in spin-polarized transport.* Phys. Rev. B **64**, 245308 (2001).

[99] I. D'Amico and G. Vignale. *Spin Coulomb drag in the two-dimensional electron liquid.* Phys. Rev. B **68**, 045307 (2003).

[100] C. P. Weber, N. Gedik, J. E. Moore, J. Orenstein, J. Stephens, and D. D. Awschalom. *Observation of spin Coulomb drag in a two-dimensional electron gas.* Nature **437**, 1330 (2005).

[101] L. Yang, J. D. Koralek, J. Orenstein, D. R. Tibbetts, J. L. Reno, and M. P. Lilly. *Doppler velocimetry of spin propagation in a two-dimensional electron gas.* Nature Phys. **8**, 153 (2012).

[102] P. Altmann, M. Kohda, C. Reichl, W. Wegscheider, and G. Salis. *Transition of a two-dimensional spin mode to a helical state by lateral confinement.* Phys. Rev. B **92**, 235304 (2015).

[103] M. Beck. *Electron spin relaxation, transport and strain-induced precession in n-GaAs.* Friedrich-Alexander-Universität Erlangen-Nürnberg, PhD thesis, 2005.

[104] R. W. Martin, R. J. Nicholas, G. J. Rees, S. K. Haywood, N. J. Mason, and P. J. Walker. *Two-dimensional spin confinement in strained-layer quantum wells.* Phys. Rev. B **42**, 9237 (1990).

[105] S. A. Crooker, D. D. Awschalom, J. J. Baumberg, F. Flack, and N. Samarth. *Optical spin resonance and transverse spin relaxation in magnetic semiconductor quantum wells.* Phys. Rev. B **56**, 7574 (1997).

[106] R. Fiederling, P. Grabs, W. Ossau, G. Schmidt, and L. W. Molenkamp. *Detection of electrical spin injection by light-emitting diodes in top- and side-emission configurations.* Appl. Phys. Lett. **82**, 2160 (2003).

[107] G. Bayreuther, M. Dumm, B. Uhl, R. Meier, and W. Kipferl. *Magnetocrystalline volume and interface anisotropies in epitaxial films: Universal relation and Néel's model (invited).* J. Appl. Phys. **93**, 8230 (2003).

[108] U. Welp, V. K. Vlasko-Vlasov, X. Liu, J. K. Furdyna, and T. Wojtowicz. *Magnetic Domain Structure and Magnetic Anisotropy in $Ga_{1-x}Mn_xAs$.* Phys. Rev. Lett. **90**, 167206 (2003).

[109] G. P. Moore, J. Ferré, A. Mougin, M. Moreno, and L. Däweritz. *Magnetic anisotropy and switching process in diluted $Ga_{1-x}Mn_xAs$ magnetic semiconductor films.* J. Appl. Phys. **94**, 4530 (2003).

[110] J. Wenisch, C. Gould, L. Ebel, J. Storz, K. Pappert, M. J. Schmidt, C. Kumpf, G. Schmidt, K. Brunner, and L. W. Molenkamp. *Control of Magnetic Anisotropy in (Ga,Mn)As by Lithography-Induced Strain Relaxation.* Phys. Rev. Lett. **99**, 077201 (2007).

[111] F. Hoffmann, G. Woltersdorf, W. Wegscheider, A. Einwanger, D. Weiss, and C. H. Back. *Mapping the magnetic anisotropy in (Ga,Mn)As nanostructures.* Phys. Rev. B **80**, 054417 (2009).

[112] A. Einwanger. *Spin-Injection into GaAs using ferromagnetic (Ga,Mn)As contacts*. Universität Regensburg, PhD thesis, 2012.

[113] D. T. F. Marple. *Refractive Index of GaAs*. J. Appl. Phys. **35**, 1241 (1964).

[114] J. S. Blakemore. *Semiconducting and other major properties of gallium arsenide*. J. Appl. Phys. **53**, R123 (1982).

[115] M. D. Sturge. *Optical Absorption of Gallium Arsenide between 0.6 and 2.75 eV*. Phys. Rev. **127**, 768 (1962).

[116] P. D. Dapkus, N. Holonyak Jr., R. D. Burnham, D. L. Keune, J. W. Burd, K. L. Lawley, and R. E. Walline. *Spontaneous and Stimulated Carrier Lifetime (77 °K) in a High-Purity, Surface-Free GaAs Epitaxial Layer*. J. Appl. Phys. **41**, 4194 (1970).

[117] C. J. Hwang. *Doping Dependence of Hole Lifetime in n-Type GaAs*. J. Appl. Phys. **42**, 4408 (1971).

[118] F. K. Kneubühl and M. W. Sigrist. *Laser*. 7. Aufl. Wiesbaden: Vieweg+ Teubner-Verlag, 2008.

[119] M. Oestreich, S. Hallstein, A. P. Heberle, K. Eberl, E. Bauser, and W. W. Rühle. *Temperature and density dependence of the electron Landé g factor in semiconductors*. Phys. Rev. B **53**, 7911 (1996).

[120] M. J. Snelling, G. P. Flinn, A. S. Plaut, R. T. Harley, A. C. Tropper, R. Eccleston, and C. C. Phillips. *Magnetic g factor of electrons in $GaAs/Al_xGa_{1-x}As$ quantum wells*. Phys. Rev. B **44**, 11345 (1991).

[121] C. Awo-Affouda, O. M. J. van 't Erve, G. Kioseoglou, A. T. Hanbicki, M. Holub, C. H. Li, and B. T. Jonker. *Contributions to Hanle lineshapes in Fe/GaAs nonlocal spin valve transport*. Appl. Phys. Lett. **94**, 102511 (2009).

[122] J. Shiogai, M. Ciorga, M. Utz, D. Schuh, T. Arakawa, M. Kohda, K. Kobayashi, T. Ono, W. Wegscheider, D. Weiss, and J. Nitta. *Dynamic nuclear spin polarization in an all-semiconductor spin injection device with (Ga,Mn)As/n-GaAs spin Esaki diode*. Appl. Phys. Lett. **101**, 212402 (2012).

[123] A. Fuhrer, S. F. Alvarado, G. Salis, and R. Allenspach. *Fast electrical switching of spin injection in nonlocal spin transport devices*. Appl. Phys. Lett. **98**, 202104 (2011).

[124] P. R. Hammar and M. Johnson. *Detection of Spin-Polarized Electrons Injected into a Two-Dimensional Electron Gas*. Phys. Rev. Lett. **88**, 066806 (2002).

[125] H. C. Koo, J. H. Kwon, J. Eom, J. Chang, S. H. Han, and M. Johnson. *Control of Spin Precession in a Spin-Injected Field Effect Transistor.* Science **325**, 1515 (2009).

[126] R. Jansen, B.-C. Min, and S. P. Dash. *Oscillatory spin-polarized tunnelling from silicon quantum wells controlled by electric field.* Nat. Mater. **9**, 133 (2010).

[127] M. Oltscher, M. Ciorga, M. Utz, D. Schuh, D. Bougeard, and D. Weiss. *Electrical Spin Injection into High Mobility 2D Systems.* Phys. Rev. Lett. **113**, 236602 (2014).

[128] K. Chen and S. Zhang. *Enhancement of spin accumulation in ballistic transport regime.* Phys. Rev. B **92**, 214402 (2015).

[129] M. Buchner, T. Kuczmik, M. Oltscher, M. Ciorga, T. Korn, J. Loher, D. Schuh, C. Schüller, D. Bougeard, D. Weiss, and C. H. Back. *Optical investigation of electrical spin injection into an inverted two-dimensional electron gas structure.* Phys. Rev. B **95**, 035304 (2017).

[130] M. Oltscher. *Spininjektion in zweidimensionale Elektronengase.* Universität Regensburg, Diploma thesis, 2011.

[131] T. Kuczmik. *Spin injection into 2DEG: towards ballistic structures.* Universität Regensburg, Master's thesis, 2013.

[132] D. Popp. *Spininjektion in zweidimensionale Elektronensysteme.* Universität Regensburg, Master's thesis, 2016.

[133] G. B. Stringfellow, W. Koschel, F. Briones, J. Gladstone, and G. Patterson. *Photoluminescence of carbon implanted GaAs.* Appl. Phys. Lett. **39**, 581 (1981).

[134] L. Pavesi and M. Guzzi. *Photoluminescence of $Al_xGa_{1-x}As$ alloys.* J. Appl. Phys. **75**, 4779 (1994).

[135] T. Kuczmik, M. Oltscher, A. Bayer, D. Schuh, D. Bougeard, M. Ciorga, and D. Weiss. *Hanle spin precession in a two-dimensional electron system.* Phys. Rev. B **95**, 195315 (2017).

[136] M. Ciorga. Private communication, 2016.

[137] T. Kuczmik. Private communication, 2017.

[138] J.-C. Le Breton, S. Sharma, H. Saito, S. Yuasa, and R. Jansen. *Thermal spin current from a ferromagnet to silicon by Seebeck spin tunnelling.* Nature **475**, 82 (2011).

[139] G. E. W. Bauer, E. Saitoh, and B. J. van Wees. *Spin caloritronics.* Nat. Mater. **11**, 391 (2012).

[140] R. Jansen, A. M. Deac, H. Saito, and S. Yuasa. *Thermal spin current and magnetothermopower by Seebeck spin tunneling.* Phys. Rev. B **85**, 094401 (2012).

[141] A. Jain, C. Vergnaud, J. Peiro, J. C. Le Breton, E. Prestat, L. Louahadj, C. Portemont, C. Ducruet, V. Baltz, A. Marty, A. Barski, P. Bayle-Guillemaud, L. Vila, J.-P. Attané, E. Augendre, H. Jaffrès, J.-M. George, and M. Jamet. *Electrical and thermal spin accumulation in germanium.* Appl. Phys. Lett. **101**, 022402 (2012).

[142] K.-R. Jeon, B.-C. Min, S.-Y. Park, K.-D. Lee, H.-S. Song, Y.-H. Park, Y.-H. Jo, and S.-C. Shin. *Thermal spin injection and accumulation in CoFe/MgO/n-type Ge contacts.* Sci. Rep. **2**, 962 (2012).

[143] K.-R. Jeon, B.-C. Min, S.-Y. Park, K.-D. Lee, H.-S. Song, Y.-H. Park, and S.-C. Shin. *Thermal spin injection and accumulation in CoFe/MgO tunnel contacts to n-type Si through Seebeck spin tunneling.* Appl. Phys. Lett. **103**, 142401 (2013).

[144] A. Dankert and S. P. Dash. *Thermal creation of electron spin polarization in n-type silicon.* Appl. Phys. Lett. **103**, 242405 (2013).

[145] K.-R. Jeon, B.-C. Min, A. Spiesser, H. Saito, S.-C. Shin, S. Yuasa, and R. Jansen. *Voltage tuning of thermal spin current in ferromagnetic tunnel contacts to semiconductors.* Nat. Mater. **13**, 360 (2014).

[146] X. Lou, C. Adelmann, M. Furis, S. A. Crooker, C. J. Palmstrøm, and P. A. Crowell. *Electrical Detection of Spin Accumulation at a Ferromagnet-Semiconductor Interface.* Phys. Rev. Lett. **96**, 176603 (2006).

[147] S. P. Dash, S. Sharma, R. S. Patel, M. P. de Jong, and R. Jansen. *Electrical creation of spin polarization in silicon at room temperature.* Nature **462**, 491 (2009).

[148] E. McCann and V. I. Fal'ko. *A tunnel junction between a ferromagnet and a normal metal: magnon-assisted contribution to thermopower and conductance.* J. Magn. Magn. Mater. **268**, 123 (2004).

[149] R. Jansen. *Silicon spintronics.* Nat. Mater. **11**, 400 (2012).

[150] O. Txoperena and F. Casanova. *Spin injection and local magnetoresistance effects in three-terminal devices.* J. Phys. D: Appl. Phys. **49**, 133001 (2016).

[151] S. Sharma, A. Spiesser, S. P. Dash, S. Iba, S. Watanabe, B. J. van Wees, H. Saito, S. Yuasa, and R. Jansen. *Anomalous scaling of spin accumulation in ferromagnetic tunnel devices with silicon and germanium.* Phys. Rev. B **89**, 075301 (2014).

[152] M. Tran, H. Jaffrès, C. Deranlot, J.-M. George, A. Fert, A. Miard, and A. Lemaître. *Enhancement of the Spin Accumulation at the Interface between a Spin-Polarized Tunnel Junction and a Semiconductor.* Phys. Rev. Lett. **102**, 036601 (2009).

[153] R. Jansen, A. M. Deac, H. Saito, and S. Yuasa. *Injection and detection of spin in a semiconductor by tunneling via interface states.* Phys. Rev. B **85**, 134420 (2012).

[154] O. Txoperena, Y. Song, L. Qing, M. Gobbi, L. E. Hueso, H. Dery, and F. Casanova. *Impurity-Assisted Tunneling Magnetoresistance under a Weak Magnetic Field.* Phys. Rev. Lett. **113**, 146601 (2014).

[155] A. G. Swartz, S. Harashima, Y. Xie, D. Lu, B. Kim, C. Bell, Y. Hikita, and H. Y. Hwang. *Spin-dependent transport across $Co/LaAlO_3/SrTiO_3$ heterojunctions.* Appl. Phys. Lett. **105**, 032406 (2014).

[156] Y. Song and H. Dery. *Magnetic-Field-Modulated Resonant Tunneling in Ferromagnetic-Insulator-Nonmagnetic Junctions.* Phys. Rev. Lett. **113**, 047205 (2014).

[157] T. Wagner, J. A. Haigh, K. Olejník, A. C. Irvine, V. Novák, and J. Wunderlich. *Noise-based approximation to thermal spin-injection in Fe/GaAs*, to be published.

[158] T. Wagner. Private communication, 2017.

[159] R. Moosbühler. *GaAs(001)-Oberflächen-Rekonstruktionen und epitaktische Fe-Schichten auf GaAs(001): Wachstum und magnetische Anisotropie.* Universität Regensburg, PhD thesis, 2003.

[160] T. Hupfauer. *Transportanisotropien an Fe/GaAs-Grenzflächen.* Universität Regensburg, PhD thesis, 2015.

[161] H. Haken and H. C. Wolf. *Molekülphysik und Quantenchemie - Einführung in die experimentellen und theoretischen Grundlagen.* 5. Aufl. Berlin Heidelberg: Springer-Verlag, 2006.

[162] G. Bayreuther, J. Premper, M. Sperl, and D. Sander. *Uniaxial magnetic anisotropy in Fe/GaAs(001): Role of magnetoelastic interactions.* Phys. Rev. B **86**, 054418 (2012).

[163] R. Moosbühler, F. Bensch, M. Dumm, and G. Bayreuther. *Epitaxial Fe films on GaAs(001): Does the substrate surface reconstruction affect the uniaxial magnetic anisotropy?* J. Appl. Phys. **91**, 8757 (2002).

[164] M. Zölfl, M. Brockmann, M. Köhler, S. Kreuzer, T. Schweinböck, S. Miethaner, F. Bensch, and G. Bayreuther. *Magnetic films epitaxially grown on semiconductors.* J. Magn. Magn. Mater. **175**, 16 (1997).

[165] M. Brockmann, M. Zölfl, S. Miethaner, and G. Bayreuther. *In-plane volume and interface magnetic anisotropies in epitaxial Fe films on GaAs(0 0 1).* J. Magn. Magn. Mater. **198-199**, 384 (1999).

[166] F. Bensch, R. Moosbühler, and G. Bayreuther. *Onset of magnetic anisotropy in epitaxial Fe films on GaAs(001).* J. Appl. Phys. **91**, 8754 (2002).

[167] M. Košuth, V. Popescu, H. Ebert, and G. Bayreuther. *Magnetic anisotropy of thin Fe films on GaAs.* Europhys. Lett. **72**, 816 (2005).

[168] K. Zakeri, T. Kebe, J. Lindner, and M. Farle. *Magnetic anisotropy of Fe/GaAs(0 0 1) ultrathin films investigated by in situ ferromagnetic resonance.* J. Magn. Magn. Mater. **299**, L1 (2006).

[169] T. Hupfauer, A. Matos-Abiague, M. Gmitra, F. Schiller, J. Loher, D. Bougeard, C. H. Back, J. Fabian, and D. Weiss. *Emergence of spin-orbit fields in magnetotransport of quasi-two-dimensional iron on gallium arsenide.* Nat. Commun. **6**, 7374 (2015).

[170] P. M. Oppeneer. *Magneto-Optical Kerr Spectra* (in : *Handbook of Magnetic Materials, Volume 13,* edited by K. H. J. Buschow). Amsterdam: Elsevier, 2001.

[171] S. Blundell. *Magnetism in Condensed Matter.* Oxford: Oxford University Press, 2001.

[172] J. M. D. Coey. *Magnetism and Magnetic Materials.* Cambridge: Cambridge University Press, 2009.

[173] Z. Q. Qiu and S. D. Bader. *Surface magneto-optic Kerr effect.* Rev. Sci. Instrum. **71**, 1243 (2000).

[174] M. Nývlt. *Optical interactions in ultrathin magnetic film structures.* Charles University in Prague, PhD thesis, 1996.

[175] P. N. Argyres. *Theory of the Faraday and Kerr Effects in Ferromagnetics.* Phys. Rev. **97**, 334 (1955).

[176] H. S. Bennett and E. A. Stern. *Faraday Effect in Solids.* Phys. Rev. **137**, A448 (1965).

[177] P. Bruno, Y. Suzuki, and C. Chappert. *Magneto-optical Kerr effect in a paramagnetic overlayer on a ferromagnetic substrate: A spin-polarized quantum size effect.* Phys. Rev. B **53**, 9214 (1996).

[178] M. Gmitra, A. Matos-Abiague, C. Draxl, and J. Fabian. *Magnetic Control of Spin-Orbit Fields: A First-Principles Study of Fe/GaAs Junctions.* Phys. Rev. Lett. **111**, 036603 (2013).

[179] J. Moser, A. Matos-Abiague, D. Schuh, W. Wegscheider, J. Fabian, and D. Weiss. *Tunneling Anisotropic Magnetoresistance and Spin-Orbit Coupling in Fe/GaAs/Au Tunnel Junctions.* Phys. Rev. Lett. **99**, 056601 (2007).

[180] A. Matos-Abiague and J. Fabian. *Anisotropic tunneling magnetoresistance and tunneling anisotropic magnetoresistance: Spin-orbit coupling in magnetic tunnel junctions.* Phys. Rev. B **79**, 155303 (2009).

[181] M. Buchner, P. Högl, S. Putz, M. Gmitra, S. Günther, M. A. W. Schoen, M. Kronseder, D. Schuh, D. Bougeard, J. Fabian, and C. H. Back. *Anisotropic Polar Magneto-Optic Kerr Effect of Ultrathin Fe/GaAs(001) Layers due to Interfacial Spin-Orbit Interaction.* Phys. Rev. Lett. **117**, 157202 (2016).

[182] H.-P. Schönherr, R. Nötzel, W. Ma, and K. H. Ploog. *Evolution of the surface morphology of Fe grown on GaAs (100), (311)A, and (331)A substrates by molecular beam epitaxy.* J. Appl. Phys. **89**, 169 (2001).

[183] D. O. Demchenko and A. Y. Liu. *Influence of interface structure on electronic properties and Schottky barriers in Fe/GaAs magnetic junctions.* Phys. Rev. B **73**, 115332 (2006).

[184] T. Ashraf, C. Gusenbauer, J. Stangl, G. Hesser, M. Wegscheider, and R. Koch. *Stress and interdiffusion during molecular beam epitaxy of Fe on As-rich GaAs(001).* J. Phys.: Condens. Matter **23**, 042001 (2011).

[185] T. Ashraf, C. Gusenbauer, J. Stangl, G. Hesser, and R. Koch. *Growth, structure and morphology of epitaxial Fe(001) films on GaAs(001)c(4×4).* J. Phys.: Condens. Matter **27**, 036001 (2015).

[186] M. Dumm, M. Zölfl, R. Moosbühler, M. Brockmann, T. Schmidt, and G. Bayreuther. *Magnetism of ultrathin FeCo (001) films on GaAs(001).* J. Appl. Phys. **87**, 5457 (2000).

[187] G. Woltersdorf. *Spin-pumping and two-magnon scattering in magnetic multilayers.* Simon Fraser University, PhD thesis, 2004.

[188] M. Brockmann. *Epitaxie und magnetische in-plane-Anisotropie dünner Fe(001)-Schichten auf Au(001) und GaAs(001).* Universität Regensburg, PhD thesis, 2000.

[189] M. Zölfl. *Eisen auf Gallium-Arsenid: Epitaxie, Magnetismus und Transport.* Universität Regensburg, PhD thesis, 2001.

[190] F. Bensch. *Der magnetische Phasenübergang und das Einsetzen des Ferromagnetismus bei dünnen Eisenschichten auf Galliumarsenid.* Universität Regensburg, PhD thesis, 2001.

[191] T. Kebe. *SQUID-Magnetometry on Fe Monolayers on GaAs(001) in UHV*. Universität Duisburg-Essen, PhD thesis, 2006.

[192] A. Fiore, V. Berger, E. Rosencher, P. Bravetti, and J. Nagle. *Phase matching using an isotropic nonlinear optical material*. Nature **391**, 463 (1998).

[193] J. H. Burnett, Z. H. Levine, and E. L. Shirley. *Intrinsic birefringence in calcium fluoride and barium fluoride*. Phys. Rev. B **64**, 241102 (2001).

[194] P. B. Johnson and R. W. Christy. *Optical constants of transition metals: Ti, V, Cr, Mn, Fe, Co, Ni, and Pd*. Phys. Rev. B **9**, 5056 (1974).

[195] M. Wimmer, M. Lobenhofer, J. Moser, A. Matos-Abiague, D. Schuh, W. Wegscheider, J. Fabian, K. Richter, and D. Weiss. *Orbital effects on tunneling anisotropic magnetoresistance in Fe/GaAs/Au junctions*. Phys. Rev. B **80**, 121301 (2009).

[196] M. Lobenhofer. *TAMR-Effekt beim Tunneln durch einkristalline GaAs-Barrieren*. Universität Regensburg, PhD thesis, 2012.

[197] A. N. Chantis, K. D. Belashchenko, E. Y. Tsymbal, and M. van Schilfgaarde. *Tunneling Anisotropic Magnetoresistance Driven by Resonant Surface States: First-Principles Calculations on an Fe(001) Surface*. Phys. Rev. Lett. **98**, 046601 (2007).

[198] H. Ebert, D. Ködderitzsch, and J. Minár. *Calculating condensed matter properties using the KKR-Green's function method-recent developments and applications*. Rep. Prog. Phys. **74**, 096501 (2011).

[199] K. Wagner. *Anisotroper polarer magneto-optischer Kerreffekt an Fe/InAs/GaAs*. Universität Regensburg, Bachelor's thesis, 2017.

[200] L. Chen, M. Decker, M. Kronseder, R. Islinger, M. Gmitra, D. Schuh, D. Bougeard, J. Fabian, D. Weiss, and C. H. Back. *Robust spin-orbit torque and spin-galvanic effect at the Fe/GaAs (001) interface at room temperature*. Nat. Commun. **7**, 13802 (2016).

[201] W. Shurcliff. *Polarized Light - Production and Use*. Cambridge (Massachusetts): Harvard University Press, 1966.

[202] C. Bohren and D. Huffman. *Absorption and Scattering of Light by Small Particles*. Weinheim: Wiley-VCH-Verlag, 2004.

Danksagung

Zunächst möchte ich mich bei meinem Betreuer Prof. Dr. Christian H. Back dafür bedanken, dass er mir die Möglichkeit gegeben hat, die Promotion an seinem Lehrstuhl durchführen zu können. Er lenkte die Arbeit durch viele konstruktive Ideen immer in die richtige Richtung und trug durch zahlreiche Diskussionen zu einem tieferen Verständnis der Physik bei.

Prof. Dr. Dominique Bougeard danke ich für das große Interesse an meiner Arbeit, sowie die vielen hilfreichen Diskussionen während des Schreibens der Paper. Desweiteren wurden die untersuchten Halbleiterwafer bei ihm in der Gruppe hergestellt. In diesem Zusammenhang möchte ich auch Dr. Dieter Schuh, Josef Loher und Dr. Matthias Kronseder für das Wachstum der Heterostrukturen danken.

Prof. Dr. Jaroslav Fabian danke ich für viele hilfreiche Diskussionen zum Thema AP-MOKE. Außerdem wurden die theoretischen Grundlagen des AP-MOKE in seiner Arbeitsgruppe erarbeitet. Hierbei danke ich insbesondere Dr. Martin Gmitra und Sebastian Putz für das Durchführen der DFT-Rechnungen und Petra Högl für die Entwicklung des phänomenologischen Modells.

Bei Prof. Dr. Dieter Weiss möchte ich mich dafür bedanken, dass ich die Einrichtungen seines Lehrstuhls, insbesondere die CAIBE und den Alu-Bonder, nutzen durfte. Zum anderen danke ich ihm für die Möglichkeit, mit meinem optischen Setup einen Blick auf die 2DEG-Proben werfen zu können, die an seinem Lehrstuhl hergestellt wurden.

Ein ganz besonderes Dankeschön geht an Dr. Mariusz Ciorga, Thomas Kuczmik und Martin Oltscher dafür, dass sie mir die Möglichkeit gewährten, ihre Proben zu untersuchen. Thomas und Martin haben die Proben zum Teil extra für mich angefertigt und sie außerdem mittels Magnetotransportmessungen charakterisiert. Die unzähligen Diskussionen zum Thema Spininjektion ins 2DEG und die stets gute Zusammenarbeit haben ganz wesentlich zum Erfolg der zugehörigen Experimente beigetragen.

Prof. Dr. Christian Schüller danke ich dafür, dass ich die Mikrophotolumineszenz-Messungen in seiner Arbeitsgruppe durchführen konnte. Ein besonderer Dank richtet sich hierbei an Dr. Tobias Korn, der das Setup zu diesem Zweck für mich

umgebaut hat. Außerdem nahm er sich stets Zeit, um meine Fragen zum Thema Spininjektion und -relaxation im 2DEG zu beantworten.

Felix Schwarzhuber aus der Arbeitsgruppe von Prof. Dr. Josef Zweck danke ich für die TEM-Bilder meiner Proben.

Vielen Dank auch an Martin Schön und Markus Härtinger, welche so manche meiner Proben mittels FMR charakterisiert haben. Markus Härtinger gilt hierbei ein ganz besonderer Dank für die Bereitstellung seiner Fitroutinen.

Ebenso danke ich Helmut Körner für unzählige SQUID-Messungen, sowie deren Auswertung.

Ein besonderes Dankeschön geht an Stefan Günther. Sein Fachwissen im Bereich optische Experimente hat ganz wesentlich zum Erfolg der AP-MOKE Messungen beigetragen. Ein weiterer Dank geht außerdem an Maximilian Schmid, der stets hilfreiche Tipps in Sachen Messtechnik auf Lager hatte.

Martin Obstbaum, Martin Decker, Tobias Weindler und Helmut Körner danke ich für die stets gute Zusammenarbeit im Gelbraum und die großartige Unterstützung bei der Probenstrukturierung. Martin Decker gilt hierbei ein ganz besonderer Dank, da er mich auf die Möglichkeit hingewiesen hat, ein Doppellacksystem für die optische Lithographie einzusetzen, was die Lift-Off-Prozesse doch erheblich einfacher gestaltete.

Ein besonderer Dank geht an unsere Lehrstuhltechniker Markus Hollnberger und Dieter Schierl, die bei vielen kleineren und größeren technischen Problemen stets eine helfende Hand parat hatten. In diesem Zusammenhang danke ich auch den Mitarbeitern der Mechanik- und der Elektronikwerkstatt der Fakultät für die stets großartige Beratung und die Herstellung der benötigten wissenschaftlichen Ausrüstung. Christian Haimerl und Thomas Solleder danke ich zudem für die regelmäßige Versorgung mit flüssigem Helium.

Ein herzliches Dankeschön auch an unsere Sekretärinnen Magdalena Pfleger, Sylvia Hrdina, Claudia Zange und Doris Meier für die Erledigung sämtlicher anfallender bürokratischer Tätigkeiten.

Meinen Bürokollegen Johannes Stigloher, Robert Islinger und Martin Schön danke ich für die angenehme und lockere Atmosphäre und dem schnellen Aushelfen, wenn Origin oder Python mal wieder geklemmt hat.

Zuletzt möchte ich mich bei allen noch nicht genannten Kollegen am Lst. Back für die angenehme und hilfsbereite Arbeitsatmosphäre bedanken.

Vielen Dank!